# Unveiling the surface-interface properties of perovskite crystals and pivotal regulation strategies

Qin Li[1,§], Ziyu Wang[1,§], Junjie Ma[1] (✉), Mengqi Han[1], Peng Gao[1], Meng Cai[1], Yiqiang Zhang[1] (✉), Yanlin Song[1,2] (✉), and Shou Peng[3,4]

[1] *Henan Institute of Advanced Technology, College of Chemistry, Zhengzhou University, Zhengzhou 450001, China*
[2] *Key Laboratory of Green Printing, Institute of Chemistry, Chinese Academy of Sciences (ICCAS), Beijing 100190, China*
[3] *China National Building Material Group Co., Ltd., Beijing 100036, China*
[4] *State Key Laboratory of Advanced Technology for Float Glass, Beijing 100036, China*
[§] *Qin Li and Ziyu Wang contributed equally to this work.*

## ABSTRACT

Metal-halide perovskite solar cells have garnered significant research attention in the last decade due to their exceptional photovoltaic performance and potential for commercialization. Despite achieving remarkable power conversion efficiency of up to 26.1%, a substantial discrepancy persists when compared to the theoretical Shockley–Queisser (SQ) limit. One of the most serious challenges facing perovskite solar cells is the energy loss incurred during photovoltaic conversion, which affects the SQ limits and stability of the device. More significant than the energy loss occurring in the bulk phase of the perovskite is the energy loss occurring at the surface-interface. Here, we provide a systematic overview of the physical and chemical properties of the surface-interface. Firstly, we delve into the underlying mechanism causing the energy deficit and structural degradation at the surface-interface, aiming to enhance the understanding of carrier transport processes and structural chemical reactivity. Furthermore, we systematically summarized the primary modulating pathways, including surface reconstruction, dimensional construction, and electric-field regulation. Finally, we propose directions for future research to advance the efficiency of perovskite solar cells towards the radiative limit and their widespread commercial application.

## KEYWORDS

perovskite solar cells, surface-interface treatment, defect modification, dimensional design, energy regulation, heterojunction and homojunction

## 1 Introduction

Organic–inorganic perovskite solar cells (PSCs) stand out as one of the most promising photovoltaic technologies, distinguished by their extraordinary photoelectric properties, such as an adjustable band gap, rapid carrier migration rate, high absorption coefficient, and long carrier diffusion length [1–7]. The power conversion efficiency (PCE) of PSCs has soared to an impressive certified 26.1% in recent years, approaching the theoretical maximum efficiency (31%) of single-junction PSCs [8, 9]. Despite this rapid development, two challenges stemming from the perovskite surface-interface remain unresolved: maintaining long-term operational stability and minimizing energy loss during the carrier transport process [10, 11]. The fragile perovskite surface-interface is highly sensitive to water, oxygen, and light, the external water and oxygen can seriously harm the internal lattice of the perovskite through its primary point of entry at the surface-interface [12–15]. Additionally, lattice discontinuities significantly alter the distribution of periodic potential fields inside the crystal, resulting in unique physical and chemical properties of perovskite surfaces and interfaces. The surface-interface of the perovskite has a more significant impact on the perovskite film than the interior

due to lattice distortion, leading to several deleterious defects and structural disorders, thus causing energy loss during the photovoltaic conversion process of PSCs. Hence, an in-depth understanding of the surface-interface properties of the PSCs is highly desirable as a prerequisite for rational modulation strategies to reconstruct surface states.

The inferior surface-interface characteristics have drawn considerable attention from the perovskite community. Defects act as non-radiative carrier recombination centers, negatively affecting device performance with hysteresis and degradation issues [16, 17]. Various techniques, including surface passivation (SP) and recrystallization of surface growth, have been employed to prevent defect development. Advantages of two-dimensional (2D) perovskite over three-dimensional (3D) perovskite include higher formation energy and longer alkyl chain cations, preventing water molecules adsorption and improving moisture stability [18–21]. Researchers have integrated 2D and 3D perovskite through dimensional structure design, promoting joint improvement in PCE and stability of PSCs. The built-in electric field, affecting carrier transport and energy transfer, is significantly influenced by the surface condition as well [22, 23]. Thoughtful design of heterojunctions enables thorough alteration of carrier dynamics

within PSCs. Although the surface state and alignment of energy level between functional layers have been improved by constructing heterojunctions, significant research advances in carrier dynamics, lattice stability, and energy transfer have not been systematically reviewed. Therefore, it is crucially necessary to analyze the relevant theoretical mechanisms and develop regulation strategies to offer novel perspectives on improving the interfacial properties of perovskite.

Thus, this review outlines the relationship between surface-interface structure and associated physical and chemical properties concerning surface reconstruction, dimensional engineering, and energy regulation. Firstly, we provide a basic theoretical analysis of energy and stability. Then, we summarize modulation strategies for improving perovskite surfaces and interfaces, including suppressing perovskite surface and interface defects, optimizing thin film surfaces, enhancing the stability of perovskite through bonding between low-dimensional (LD) and 3D perovskite, and examining the effects of homogeneous and heterogeneous junctions on perovskite energy. Finally, we present a summary and outlook for exploring research trends and the most promising future paths for perovskite surface treatment. This review provides recommendations for preparing dense and defect-free perovskite films to facilitate the industrialization of PSCs.

# 2 Mechanism analysis of energy deficit and structural degradation

The existence of energy deficit ($E_{loss}$) and structural degradation pose challenges to the photovoltaic performance, limiting the practical application of PSCs close to the Shockley–Queisser (SQ) limit. Therefore, gaining an in-depth understanding of the underlying theoretical mechanism concerning carrier recombination pathways and crystal degradation processes is a prerequisite for guiding the design of modulation strategies. This section aims to outline the origin of electrical energy loss and explore dimensional modulation as a means to optimize surface-interface properties (Fig. 1) [17, 24–26].

## 2.1 Origin of electrical $E_{loss}$

In an ideal photoelectric conversion process within PSCs, incident photons are efficiently harvested and converted into photogenerated carriers, thereby generating electricity. However, such a complete process unavoidably incurs electrical $E_{loss}$ due to non-radiative recombination arising from surface defects, disordered crystal lattice, and energy band misalignment (Fig. 2(a)).

### 2.1.1 Generating principle of the $E_{loss}$

The open-circuit voltage ($V_{oc}$) in PSCs is primarily determined by the splitting of quasi-Fermi levels of electrons ($E_{Fn}$) and holes ($E_{Fp}$) under sunlight illumination. However, undesired carrier recombination loss reduces the splitting of quasi-Fermi levels, consequently decreasing the $V_{oc}$ [27, 28]. The overall $E_{loss}$ of PSCs can be further described by Eq. (1)

$$E_{loss} = qV_{loss} = E_g - qV_{oc} = \Delta E_1 + \Delta E_2 + \Delta E_3 \qquad (1)$$

which is divided into three detailed parameters. Among these parameters, $q$ is the elemental charge, $E_g$ is the bandgap, $V_{loss}$ is the open-circuit voltage deficit, $\Delta E_3$ is the nonradiative recombination loss, $\Delta E_1$ and $\Delta E_2$ represent radiation recombination losses originating from absorption above and below the band gap of the perovskite material, respectively. $\Delta E_1$ occurs due to a mismatch between the narrow solid-angle radiation received from the sun and the omnidirectional radiation recombination, while $\Delta E_2$ is caused by low charge transfer states in PSCs, which are unavoidable in all types of solar cells. The primary source of $V_{loss}$ is
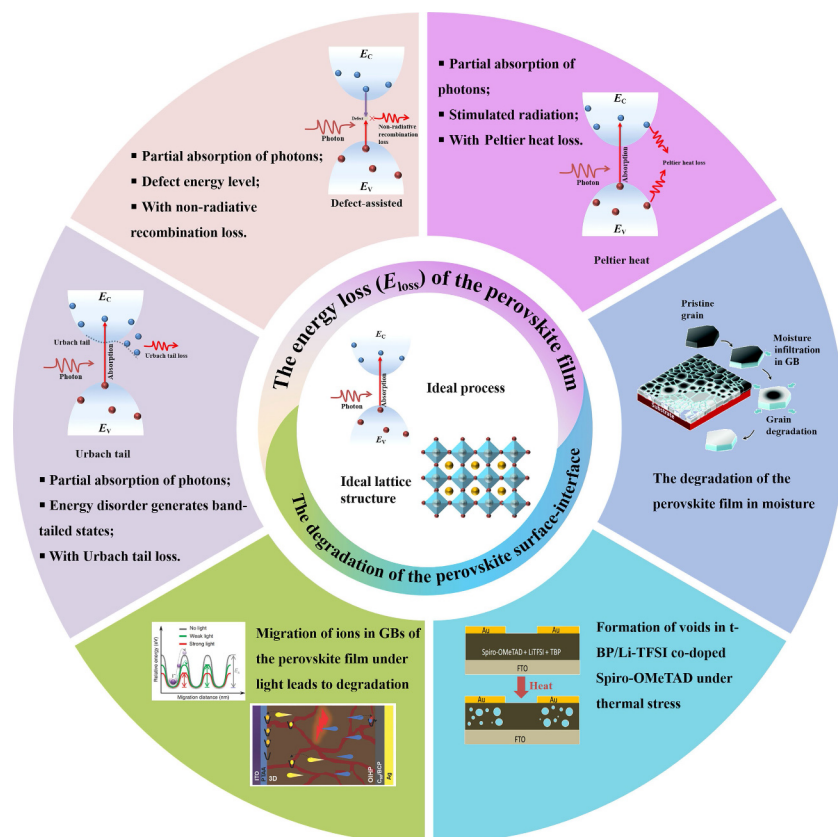


**Figure 1** The main structure framework of the mechanism analysis of energy deficit and structural degradation. Reproduced with permission from Ref. [17], © Rui, Y. C. et al. 2022. Reproduced with permission from Ref. [26], © The Royal Society of Chemistry 2016. Reproduced with permission from Ref. [24], © American Chemical Society 2017. Reproduced with permission from Ref. [25], © Zhao, Y. C. et al. 2016.
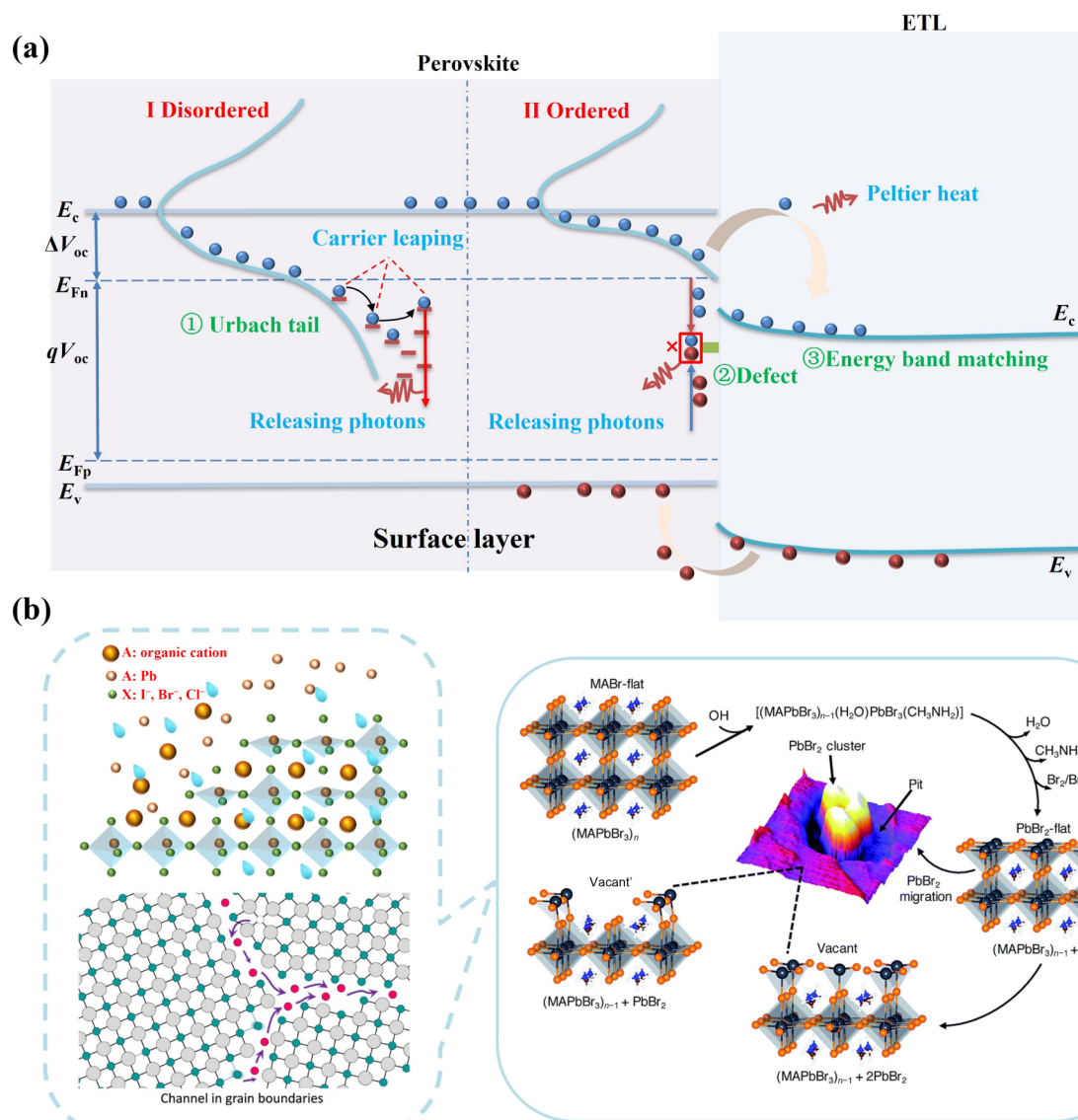
**Figure 2** (a) Main sources for energy loss in PSCs. Loss of band-tailed states in energy disorder, non-radiative recombination losses at defect energy levels during carrier migration, and Peltier heat loss in the transport of carriers between perovskite and other layers. (b) Proposed degradation pathway for the MAPbBr$_3$ single crystal in the UHV chamber in the presence of water vapor. The Vacant and Vacant' surfaces have similar morphologies with the difference of just one PbBr$_2$ molecule in the topmost atomic layer. Reproduced with permission from Ref. [55], © American Chemical Society 2016. Reproduced with permission from Ref. [56], © The Royal Society of Chemistry 2019.

$\Delta E_3$, arising from non-radiative recombination [29, 30]. The recombination process can be represented by the following Eq. (2)

$$\mathrm{d}n/\mathrm{d}t = -k_1 n - k_2 n^2 - k_3 n^3 \qquad (2)$$

where $n$ is the photogenerated carrier density, $t$ is the recombination time, and $k_1$, $k_2$, and $k_3$ are the rate constants associated with defect-assisted (single molecular charge), radiative (bimolecular charge), and Auger (Auger charge) recombination processes, respectively. Non-radiative recombination losses are dominated by defect-assisted and Auger recombination processes. Under low light intensity (carrier concentration of $10^{15}$ to $10^{16}$ cm$^{-3}$), the Auger recombination process is usually weaker compared with the other two recombination processes, as it occurs only at a carrier concentration above $10^{17}$ cm$^{-3}$. The values of $k_1$ and $k_2$, ranging from $10^{-7}$ to $10^{-5}$ cm$^3 \cdot$s$^{-1}$ and $10^{-11}$ to $10^{-10}$ cm$^3 \cdot$s$^{-1}$ respectively, can be determined using steady-state photoconductivity and Hall carrier density measurement [2, 31, 32]. At low excitation intensity, the carrier density remains low, and the carrier lifetime is limited by defect-assisted recombination. As the excitation intensity increases, the defect-assisted

recombination channels become saturated, leading to dominant radiative recombination. Non-radiative recombination occurring at the perovskite surface and interface is more severe than recombination within the bulk phase, primarily due to the following three reasons:

Firstly, defect-assisted recombination losses occur when carriers are trapped by defects during the transfer process. Secondly, the disordered nature of the crystal structure leads to the formation of band tail states near the band edges, providing an additional channel for energy loss. This creates new electronic states, inducing partial carrier hopping and leading to new band tail absorption or recombination. Finally, energy band differences between the perovskite and the transport layers facilitate carrier transport and extraction. However, when the energy band difference is too large, carriers produce Peltier heat during the leaping, leading to energy loss [33].

*2.1.2 Non-radiative recombination caused by crystal structure defects*

It is important to recognize that defects are commonly generated during the liquid−solid phase transition processes due to the low

defect formation energy, resulting in defect-induced recombination losses. In the case of the MAPbI$_3$ (MA = CH$_3$NH$_3^+$) perovskite crystal structure, it has been found that there can be 12 different types of inherent point defects [34–36]. These include atomic vacancies, such as MA (V$_{MA}$), Pb (V$_{Pb}$), and I (V$_I$) vacancies, interstitials like MA (MA$_i$), Pb (Pb$_i$), and I (I$_i$) interstitials, as well as anti-site substitutions, including MA$_{Pb}$, MA$_I$, Pb$_{MA}$, Pb$_I$, I$_{MA}$, and I$_{Pb}$. The produced defects can be further categorized into shallow-level traps and deep-level traps based on their energy level in the band gap [37–39]. Among these, deep-level traps produce more energy levels than shallow-level traps, exerting a stronger effect on carriers and are more likely to cause non-radiative recombination on the perovskite surface. According to calculations, the majority of point defects, creating shallow-level traps (MA$_i$, I$_i$, V$_{Pb}$, V$_{MA}$, V$_I$, MA$_{Pb}$, and MA$_I$) form close to the forbidden band due to their low formation energy, while deep-level traps, such as Pb$_{MA}$, Pb$_I$, and I$_{Pb}$, have higher formation energies [40]. However, under specific growth conditions, deep-level traps, such as Pb$_i$ and I$_{MA}$, can also have low formation energies, resulting in the development of non-radiative recombination centers at deep energy levels. The deep-level traps are considered the predominant non-radiative recombination centers that can trap electrons or holes, leading to a decrease in $V_{oc}$ and the overall device performance [41]. Shallow-level traps have a lesser impact on photovoltaic performance. Nevertheless, due to the flexible lattice structure of perovskite materials, even shallow-level traps with low formation energies can cause ions to accumulate at the film interface under light exposure, resulting in hysteresis and carrier bias [42, 43].

In addition to the intrinsic defects of perovskite, new defects are formed by ion migration under the influence of external environments such as light or heat [44]. The ion mobility ($\sigma_{ion}$) of the charged defects is related to the diffusion potential barrier ($\Delta E_b$) and the defect formation energy ($\Delta H$) by Eqs. (3) and (4)

$$\sigma_{ion} \sim [D] \exp\left(-\Delta E_b / KT\right) \sim \exp\left[-\left(\Delta H + \Delta E_b\right)/KT\right] = \exp\left(-\Delta E_a / KT\right) \tag{3}$$

$$\Delta E_a = \Delta E_b + \Delta H \tag{4}$$

where $[D]$ is the defect concentration, $K$ is the Boltzmann constant, $T$ is the temperature, and $\Delta E_a$ is the activation energy of the non-radiative recombination [45]. When the formation energy and diffusion potential fall simultaneously at a constant ambient temperature, more diffusion defects are produced and the ion mobility of charged defects gradually increases. Hence, by boosting the formation energy and diffusion potential of defects, the impact of defects on perovskite films can be reduced. Generally, the formation energy of most defects is an intrinsic characteristic, making the regulation of the potential of the defect diffusion a common strategy. For instance, adding a few interstitial atoms to the lattice can stabilize it and limit the migration rate of charged defects, preventing them from migrating from the source. In the following, in detail, we will cover strategies, including secondary growth by atmospheric treatment to create a more uniform film surface, secondary bonding of the additional molecules to the defects, and physical or chemical polishing.

### 2.1.3 Urbach energy

Urbach energy, indicating the width of the exponentially decaying of sub-bandgap absorption tail, is commonly used as an indicator of the electrical quality of absorption films in solar cells. Most semiconductors have an Urbach band tail below the forbidden band due to inherent static disorder in materials [46]. This causes carriers to jump between the electronic states in the Urbach tail,

resulting in photon energy being absorbed and released at the sub-bandgap [47–49]. Band-tail recombination occurs due to the band-tail states at the sub-bandgap of the perovskite materials, including band-tail losses and a new energy loss. Urbach energy ($E_U$) is calculated as follows [50]

$$E_U = \frac{E - E_g}{\ln\left(\dfrac{\alpha(E)}{\alpha_g}\right)} \tag{5}$$

where $\alpha(E)$ is the absorption coefficient spectrum and $\alpha_g$ is the value of $\alpha$ at the band gap energy ($E_g$). A higher $E_U$ value indicates increased band-tail absorption. As the Urbach tail descends, the quantity of emitted photons rises, leading to a reduction in the diffusion length of the carriers. It is reported that $V_{loss}$ improves as the $E_U$ decreases [51]. Typically, when the $E_U$ is less than 26.7 meV (at 300 K), there is very little reduction in $V_{loss}$.

However, the reduction in $V_{loss}$ increases rapidly when the $E_U$ exceeds 26.7 meV. When the Urbach energy is raised from 45 to 180 meV, the majority of the carriers recombine, shortening the carrier diffusion length and lowering the $V_{oc}$. Thus, the reduction of the band-tail recombination can increase the height difference between $E_{Fn}$ and $E_{Fp}$, resulting in a higher $V_{oc}$. Some studies have used spectroscopic ellipsometry (SE), unpolarized transmittance, and photothermal deflection spectroscopy (PDS) to derive the $\alpha$ spectra of narrow bandgap (FASnI$_3$)$_x$(MAPbI$_3$)$_{1-x}$ perovskite films, obtaining different values of $E_U$ by adjusting $x$ [52]. This indicates that varying the composition of the perovskite films has a moderating effect on energy loss. However, despite the lower $E_U$, the corresponding device efficiency is still poor. The primary reason is that composition adjustment can only partially reduce energy loss in the bulk phase. The energy disorder produced on the perovskite surface is more significant than that in the bulk phase because it is exposed to the environment and in touch with the transport layer.
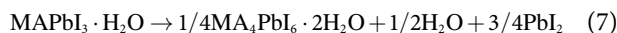
### 2.1.4 Energy-band alignment

In general, a perfect interface of perovskite/carrier transport layer (CTL) heterojunction must possess features that selectively extract majority carriers while blocking the minority carriers through a large Schottky barrier. The pushing force that separates the carriers at the interface is weakened by the misaligned energy-level alignment, which also leads to interface-induced recombination. The referred heterojunctions are mainly divided into three types: Straddling Gap (type I), Staggered Gap (type II), and Broken Gap (type III) [53]. In the type I band alignment, the conduction and valence bands ($E_c$ and $E_v$) of perovskite are sandwiched between the CTL. In this case, the energy band structure can be regarded as a potential well, where both the electrons and holes are confined to a lower energy level, resulting in electron accumulation and recombination at the interface. Type III represents the case of non-overlapping band alignment between the perovskite and carrier transport layer, where the $E_v$ of the perovskite is even higher than the $E_c$ of the CTL. Since the conduction band of perovskite is smaller than that of CTL, the carrier recombines with the $E_v$ of the perovskite during transport, preventing the formation of the typical carrier transport mechanism. Due to the difference in their energy bands, type II is utilized to make the majority of perovskite heterostructures, facilitating carrier transport [54]. However, an excessive energy band difference can result in additional Peltier heat during carrier transport, leading to $E_{loss}$. Moreover, defect levels may trap carriers during transport, causing non-radiative recombination. Therefore, proper energy level alignment is essential in order to reduce thermal losses and carrier recombination.

## 2.2 Degradation mechanisms of perovskite film

Extreme weather conditions, such as heavy rain, high temperatures, and strong ultraviolet (UV), are unavoidable during the practical operation of photovoltaic devices [24]. The instability of perovskite has emerged as the most critical issue hindering commercial applications. The surface and interface of the perovskite films are key factors affecting the stability of the final device. Due to the lattice discontinuities, uncoordinated atoms are typically exposed on the surface of perovskite films and are especially susceptible to oxygen and water intrusion, leading to unintended perovskite deterioration (Fig. 2(b)) [55, 56]. Additionally, when exposed to ambient conditions, fragile grain boundaries (GBs) create penetrating channels that accelerate the degrading process [26]. In the presence of high humidity, $MAPbI_3$ perovskite reacts with water to form the hydrated intermediate phase $MAPbI_3 \cdot H_2O$, which induces irreversible decomposition to form $PbI_2$, as shown in the following degradation process (Eqs. (6)–(8)) [57]

$$MAPbI_3 + H_2O \rightarrow MAPbI_3 \cdot H_2O \qquad (6)$$

$$MAPbI_3 \cdot H_2O \rightarrow 1/4MA_4PbI_6 \cdot 2H_2O + 1/2H_2O + 3/4PbI_2 \quad (7)$$

$$1/4MA_4PbI_6 \cdot 2H_2O \rightarrow MAI + 1/2H_2O + 1/4PbI_2 \qquad (8)$$

In addition, the film undergoes degradation under light, especially at the interface between $MAPbI_3$ and the transport layer [58]. Under light conditions, ion migration is significantly enhanced, leading to the creation of more defects and thus a decrease in cell efficiency [25]. When the light intensity increases, the diffusion potential barrier ($\Delta E_b$) decreases, leading to easier ion transport. Consequently, the stability of 3D perovskite remains one of the most critical challenges for commercialization.

In comparison to 3D perovskite, the LD perovskite exhibits a more stable structure due to better hydrophobicity and higher formation energy [59, 60]. The 2D perovskite can be obtained from 3D perovskite by slicing along (100) or (110) crystal planes. One-dimensional (1D) and zero-dimensional (0D) perovskite can be obtained by cutting 2D perovskite into metal halide lines and individual octahedra [61]. Here, let us briefly compare the performance of LD perovskite and 3D perovskite using examples of 2D and 3D perovskite. Due to the superior hydrophobicity of organic ligands and their orientational carrier transport behavior, the 2D perovskite exhibits remarkable optoelectronic characteristics and durability. The 2D perovskite has a naturally occurring quantum well structure, with organic spacers acting as formation barriers and the inorganic layers as wells [60, 62]. The majority of the components in 2D perovskite are made of hydrocarbon chains, which are then ordered or assembled to form hydrocarbon chain surfaces. These surfaces serve to separate the surrounding water from the perovskite material, significantly increasing hydrophobicity [20, 63]. The presence of hydrocarbon chains with nonpolar, lipophilic components improves the hydrophobicity of the 2D materials. Additionally, the fluorine atoms and amine molecules found in 2D perovskite are naturally hydrophobic. Therefore, the hydrophobicity of 3D perovskite can be effectively improved by the rational use of 2D perovskite, enhancing the stability of PSCs.

Furthermore, due to the quantum and dielectric confinement effects that affect the 2D perovskite, it becomes difficult to separate electron–hole pairs, making it challenging for electrons and holes to reach the appropriate transport layers. Despite affecting the cell efficiency of 2D perovskite devices to some extent, the notorious ion migration can be alleviated, thanks to the higher exciton

binding energy ($W_b$), resulting in a more stable crystal structure. The $W_b$ of 2D perovskite and 3D perovskite is expressed in Eq. (9) [60]

$$W_b^{2D} = 4\left(\frac{\varepsilon_\omega}{\varepsilon_b}\right)^2 W_b^{3D} \qquad (9)$$

where $\varepsilon_\omega$ is the dielectric constant of the well and $\varepsilon_b$ is the dielectric constant of the potential barrier. The $W_b^{2D}$ is the excitonic binding energy of the 2D perovskite and the $W_b^{3D}$ is the excitonic binding energy of the corresponding 3D perovskite. Since the dielectric constant of the organic spacer (barrier) is usually smaller than that of the inorganic layer (well), the exciton binding energy of 2D perovskite is higher than that of 3D perovskite. This is one of the reasons why 2D perovskite devices do not perform as well as their 3D counterparts. However, a higher exciton binding energy implies a higher ion activation energy ($W_a$). The $W_a$ and the $\sigma_{ion}$ are shown in Eq. (10) [64]

$$\sigma_{ion}(T) = \frac{\sigma_0}{T}\exp\left(-\frac{W_a}{K_g T}\right) \qquad (10)$$

where $K_g$ is the Boltzmann constant, $\sigma_0$ is a constant, and the $W_a$ can be derived from the slope of the $\ln(\sigma_{ion}T) - 1/kT$ relationship. The higher $W_a$ of 2D perovskite lowers the likelihood of carriers on the perovskite surface becoming activated, raising the potential barrier for carrier migration and preventing carrier migration on the surface of 3D perovskite. Therefore, by combining 2D and 3D perovskite, it is possible to address the problems of stability and ion migration of 3D perovskite, as well as the low efficiency of 2D perovskite due to quantum and dielectric confinement effects.

## 3 Modulation strategy of the perovskite surface-interface

Non-radiative recombination losses may be generated by imperfections on the surface of the perovskite film, which, in turn, affect the photovoltaic performance and operational stability. Therefore, we aim to elucidate predominant pathways for surface state reconstruction, dimensional engineering, and energy level alignment that contribute to achieving improved efficiency and highly stable perovskite solar cells. Additionally, we discuss the underlying mechanisms that drive the performance of the PSCs toward the theoretical limit.

### 3.1 Surface state reconstruction of perovskite

Due to the chemical softness of perovskite materials, defects on the surface and at the interface invariably result in either energy loss or undesirable lattice deterioration. Herein, we group the surface and interface defect modulation features into three types, including surface state reconstruction, gas-assisted surface secondary growth, and surface polishing treatment (Fig. 3(a)).

#### 3.1.1 Chemical coordination of surface defects

Uncoordinated defect sites on the perovskite film have been successfully passivated using organic chemical compounds with functional groups. Such adducts can be attached to the perovskite through covalent or ionic bonds and are rich in lone pairs of electrons. The bonding electrons can be shared between the chemical adducts and the defect sites, effectively passivating undercoordinated surface defects. In this section, we outline the surface state reconstruction strategies according to three defect types, including vacancy defects, interstitial defects, and antisite defects.

3.1.1.1  Passivation of vacancy defects

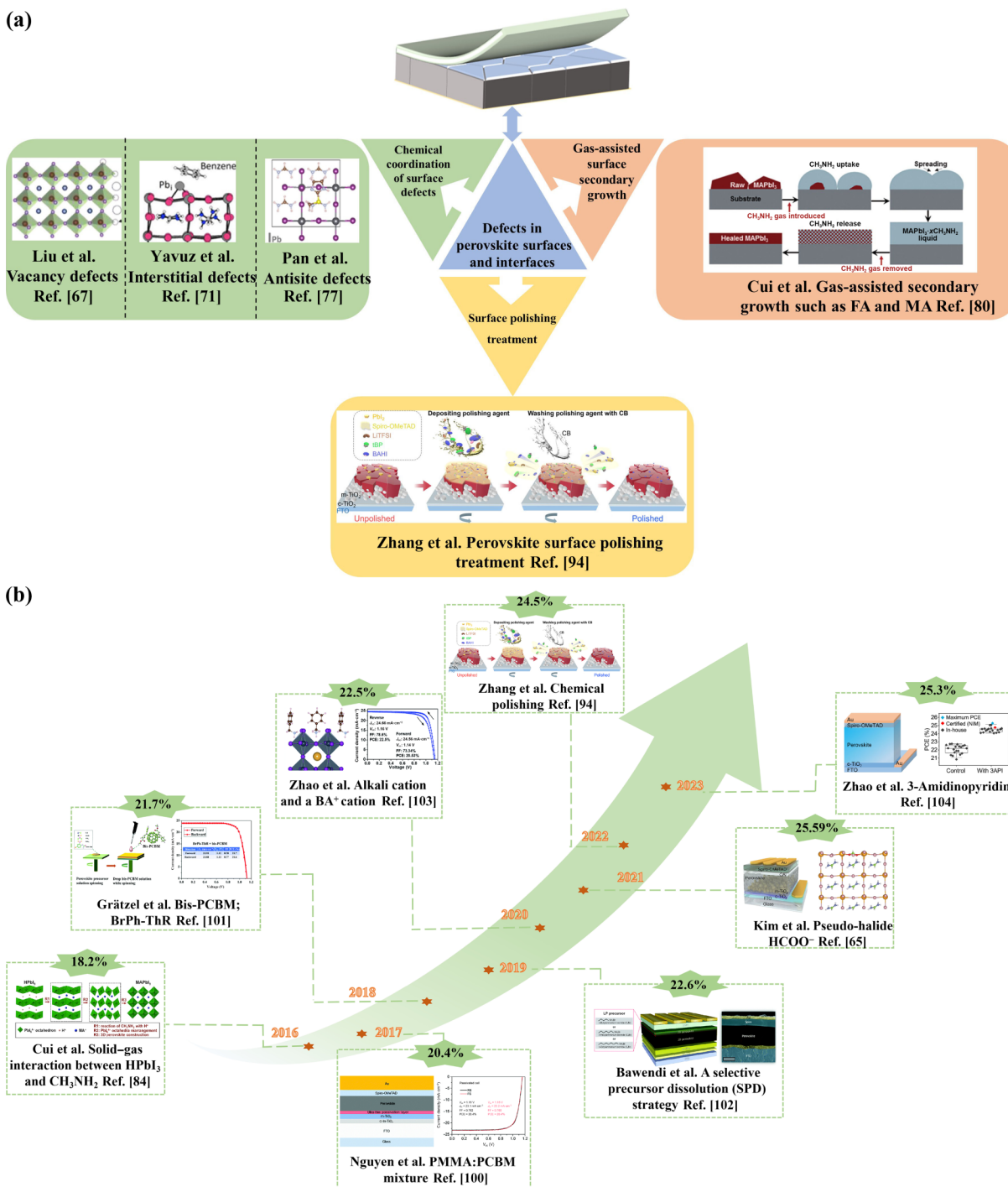Under the influence of the outside environment and post-

**(a)**



**(b)**



**Figure 3** (a) Summary of measures for passivation of defects at the perovskite surface and interface. Improvement of vacancy defects, interstitial defects, and antisite defects at the perovskite surfaces based on the chemical coordination of surface defects. Reproduced with permission from Ref. [67], © Wiley-VCH GmbH 2022. Reproduced with permission from Ref. [71], © American Chemical Society 2022. Reproduced with permission from Ref. [77], © American Chemical Society 2021. Reproduced with permission from Ref. [80], © Wiley-VCH Verlag GmbH & Co. KGaA, Weinheim 2015. Reproduced with permission from Ref. [94], © American Chemical Society 2022. Surface polishing treatments including mechanical and chemical polishing; gas assisted secondary growth and reconstruction of perovskite surfaces with atmospheres such as MA, FA, and ammonia. (b) The graphical abstract of related breakthrough works with reported maximum PCE for each year. Reproduced with permission from Ref. [65], © Jeong, J. et al. 2021. Reproduced with permission from Ref. [84], © American Chemical Society 2016. Reproduced with permission from Ref. [94], © American Chemical Society 2022. Reproduced with permission from Ref. [100], © The Royal Society of Chemistry 2017. Reproduced with permission from Ref. [101], © The Royal Society of Chemistry 2018. Reproduced with permission from Ref. [102], © The Royal Society of Chemistry 2019. Reproduced with permission from Ref. [103], © The Royal Society of Chemistry 2020. Reproduced with permission from Ref. [104], © Yang, T. H. et al. 2023.

annealing treatment, the periodic arrangement of atoms on the surface and interface of the perovskite produced by the solution method is easily disrupted, leading to vacancy defects such as $V_I$, $V_{Pb}$, etc. One of the main reasons for device instability is caused by vacancy defects, which act as electron traps to obstruct carrier transport and induce nonradiative recombination of charge carriers [65].

The superiority of $CsPbI_3$ perovskite is its unparalleled stability, whereas imperfect crystallization invariably results in unsatisfactory crystal quality and defects [66]. Donor defects of $V_I$ defect with lower formation energy are easier to form in $CsPbI_3$ perovskite compared with other defect types, which is detrimental to decreasing the Fermi level splitting and results in a lower $V_{oc}$. Du et al. developed a passivation strategy for managing $V_I$ defects

by introducing an $EMIMHSO_4$ ionic liquid into perovskite precursor [67]. They confirmed that $HSO_4^-$ plays the role of electron-acceptor and coordinates with the undercoordinated $Pb^{2+}$ to eliminate $V_I$ defects. Furthermore, they found that strong interaction between perovskite and the $EMIMHSO_4$ will probably slow the perovskite crystal growth and induce high-quality perovskite film. Jaeki et al. used the most common $HCOO^-$ to suppress $V_I$ defects at grain boundaries and surfaces of perovskite films (Fig. 4(b)) [65]. They indicated that the formate was small enough to accommodate $V_I$, thus eliminating a notorious $V_I$ defect in metal halide perovskite. The PCE of the resulting solar cell device was achieved at 25.6% due to the highest binding energy of $HCOO^-$ with $V_I$ compared to other ions. In tin-based perovskite, it is crucial to take into account not only the surface defects but also the negative effects of $Sn^{2+}$ oxidation. The device will become unstable and experience $V_{loss}$ due to surface Sn(II) oxidation and high-density Sn vacancies. Li et al. designed a 6-maleimidohexanehydrazide trifluoroacetate molecule to reconstruct the surface of $FASnI_3$ films (Fig. 4(a)) [68]. The oxidation process of $Sn^{2+}$ can be decreased by the $TFA^-$ ion reaction with $Sn^{2+}$. The $TFA^-$ ion successfully passivated the $V_I$ and $V_{Sn}$ during the action of the molecule, eliminating the electronic states brought on by $V_I$ and $V_{Sn}$ (Fig. 4(d)). Therefore, the ion coordination mechanism can be used to efficiently address the problems caused by the existence of vacancy defects. This technique, however, was not sufficient to entirely eliminate vacancy defects, particularly those seen in Sn-based perovskite or in all-inorganic perovskite, which lacked an ideal passivation mechanism. Thus, more comprehensive and effective methods are needed to address the performance degradation caused by vacancy defects.

### 3.1.1.2 Passivation of interstitial defects

The band gap of lead iodide perovskite is affected by interstitial defects rather than vacancy defects [69]. Interstitial defects are formed when impurities enter the lattice and create deep energy level traps away from the valence and conduction band edges. These defects are regarded as non-radiative combination centers that severely affect device performance [70]. Therefore, the interstitial defects need to be addressed to improve the final performance of the device. Electron-donating $FA_i$ and $Pb_i$ defects, which create deep-level traps, may limit optoelectronic performance. Oner et al. suppressed FA interstitial ($FA_i$) and Pb interstitial ($Pb_i$) defects by passivating perovskite surface defects with a benzene additive, which could provide electrons for surface defects through charge transport effects [71]. Due to its electrostatic interactions with $FA_i$ and $Pb_i$ as well as its own delocalized charge distribution capabilities, benzene can successfully eliminate deep energy level defects around $FA_i$ valance band maximum (VBM) and conduction band minimum (CBM) as well as near $Pb_i$ VBM (Figs. 4(c) and 4(e)). In addition to the passivation effect of the neutral passivator, the negatively charged ions can improve the $Pb_i$ defects with the nature of the electron donor. Kim et al. used the interaction between the negatively charged $Cl^-$ in GlyHCl and the positively charged $Pb_i$ and $Sn_i$ defects of the Sn-Pb mixed perovskite to improve the defective state [72]. It was evident that the optimized energy levels progressed toward greater binding energies, indicating that the defects had been passivated (Figs. 5(e) and 5(f)).

Recently, scientists have become enthusiastic about adding various metal ions to $CsPbI_2Br$ perovskite, which are abundant at the grain boundaries and contribute to local defect passivation, thereby enhancing the stability of the device. However, there is some controversy surrounding the doping of metal ions, and it has been argued that replacing perovskite B-site atoms with metal ions can improve device performance. Besides, it is believed that these metal ions have the potential to insert into the interstitials at the perovskite surface and interface, thereby passivating the interstitial defects of the surface. Zhang et al. incorporated Sm atoms into $CsPbI_2Br$ perovskite [73]. $Sm^{2+}$, which had a smaller atomic radius than that of $Cs^+$ and $Pb^{2+}$, thus extended the lattice rather than displacing $Cs^+$ and $Pb^{2+}$ (Fig. 4(f)). Since the substitution effects had been ruled out, the reduced angular shift was caused by the introduction of doped Sm ions into the perovskite interstitial sites. It was proved that the surface of a $CsPbI_2Br$ perovskite film doped with 0.5% Sm had greater phase stability in ambient air than that of the surface film of a pristine perovskite film, resulting in a PCE of 15.1%. Liu et al. added 3-sulfopropyl methacrylate potassium salt (SPM) additive to the perovskite precursor solution, in which the potassium ion served to fill the interstitial defects [74]. As a result, the formation of iodine-Frankl defects at the surface and GBs was prevented, and smooth, pinhole-free perovskite films were obtained.

The diffusion of charged ions is the main cause of vacancy and interstitial defects. However, ionic coordination methods alone can only partially solve these defects. Therefore, preventing the migration of charged ions before defects emerge may be one of the key tactics to improve PSCs performance.

### 3.1.1.3 Passivation of antisite defects

Antisite defects near the perovskite surface and interface are also a common deep energy level trap with high binding energy, contributing to non-radiative recombination at these regions. Vacancy and interstitial defects commonly arise readily at the perovskite surface and interface, leading to ion migration and promoting the formation of antisite defects. Using the $FAPbI_3$ surface as an example, Yang et al. observed that free FA cations exited vacant $V_{FA}^-$, and moved freely at the surface and interface. These cations primarily filled vacant $V_I^+$ sites or replaced the $I^-$ in the $PbI_x$ octahedron, resulting in FA anti-substitution (FA-I). Similarly, I anions from $V_I^+$ generated I anti-substitution (I-FA) as deep energy level traps (Fig. 5(a)) [75]. They proposed that reducing the generation of organic vacancies ($V_{FA}^-$ or $V_{MA}^-$) and inhibiting the ion migration of $FA^+$ or $MA^+$ could suppress the generation of antisite defects. To achieve this, they passivated surface defects using the additive poly-4-vinylpyridine (P4VP), which stabilizes the ammonium cation in $FA^+$ through ligand bonding and hydrogen bonding, thus eliminating antisite defects arising from vacancies such as $V_I$ and $V_{FA}$. Additionally, B-site ions and X-site ions both produce Pb-I and I-Pb at the surface and interface of Pb-rich perovskite, which results in irreversible deterioration and photoaging tendency [76]. Liu et al. addressed surface defects by introducing 2-(methylthio)-2-imidazoline cation (MT-Im) (Fig. 5(d)) [77]. They demonstrated a significant increase in the production energy of Pb-I antisite defects on the surface of perovskite films enhanced with MT-Im, indicating that MT-Im significantly affected the passivation of Pb-based defects on the perovskite film surface. In addition, MT-Im hindered the migration of $Pb^{2-}$ and mitigated the production of Pb-I antisite defects by forming $PbI_3^-$ and $NH^{2+}$. Utilizing ionic liquids to passivate perovskite surface defects has also shown promising results [7]. Liu et al. used the ionic liquid 1,3-dimethyl-3-imidazolium hexafluorophosphate ($DMIMPF_6$) to study the effect on the surface defects of $Cs_{0.08}FA_{0.92}PbI_3$ perovskite [78]. They discovered that $DMIMPF_6$ treatment passivated local edge states brought on by antisite defects, resulting in a high PCE of 23.25% for the treated perovskite devices (Fig. 5(c)). Moreover, antisite defects in the Pb-rich perovskite could be passivated through self-regulation. Liu et al. proposed that under Pb-rich conditions, interstitial Pb and vacant I form the antisite defect (Pb-I), which then self-regulates with the existing I-Pb to form a perfect crystal
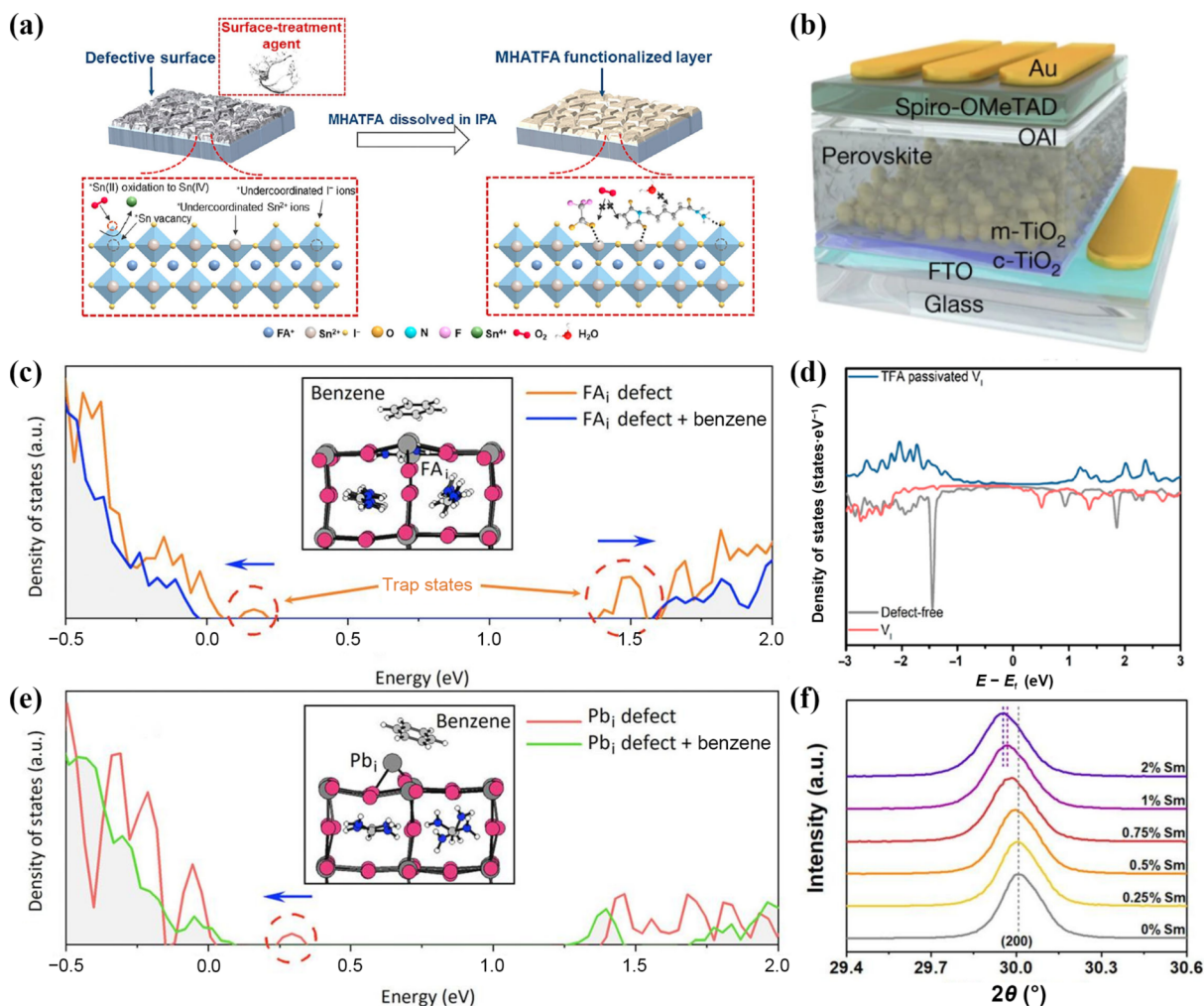
**Figure 4** (a) Schematic diagram of surface reconstruction strategy and the MHATFA passivation and protection mechanism. Reproduced with permission from Ref. [68], © American Chemical Society 2022. (b) The configuration of a typical FAPbI$_3$ PSCs device. Spiro-OMeTAD, 2,2′,7,7′-tetrakis(N,N-di-p-methoxyphenylamine)9,9′-spirobifluorene. Reproduced with permission from Ref. [65], © Jeong, J. et al. 2021. (c) Density of states (DOS) of FA$_i$ defect with and without the benzene additive. Reproduced with permission from Ref. [71], © American Chemical Society 2022. (d) DOS of defect-free, V$_I$ defected, and passivated surface. Reproduced with permission from Ref. [68], © American Chemical Society 2022. (e) Density of states of Pb$_i$ defect with and without the benzene additive. Reproduced with permission from Ref. [71], © American Chemical Society 2022. (f) Fine patterns of the peak of the (200) lattice plane. Reproduced with permission from Ref. [73], © American Chemical Society 2022.

structure without lattice expansion or contraction (Fig. 5(b)) [79]. This self-regulation process eliminates antisite defects on the perovskite surface, leading to improve the PSCs performance. However, the presence of vacancy and interstitial defects may repeatedly produce antisite defects with varying densities under different external environmental changes, making it challenging to maintain consistent defects on the perovskite surface.

Perovskite defect passivation is mainly achieved through van der Waals interaction forces between the additive and the perovskite precursor. Although this is an efficient way to deal with defects in perovskite films, the quasi-random distribution of ionic ligands on the perovskite surface due to the additive's weak van der Waals interactions limits the overall improvement of device performance. Therefore, alternative ways to regulate the perovskite surface-interface need to be explored.

### 3.1.2 Gas-assisted surface secondary growth and restructuring

In contrast to traditional chemical coordination approaches, the secondary growth method of perovskite films through dissolution and recrystallization proves to be a more efficient and precise way to eliminate surface defects. Utilizing different gases to assist the perovskite surface in undergoing secondary growth can effectively eliminate surface defects that cannot be addressed by ordinary passivation methods. Atmospheric post-treatment of perovskite

films for morphological reconstruction is an attractive approach for producing high-quality and large-scale perovskite films. Zhou et al. first proposed using methylamine (MA) gas as a post-treatment to optimize the surface of MAPbI$_3$ perovskite films, leading to defect repair on the surface [80]. This technique restored the damaged MAPbI$_3$ perovskite film to an almost perfect morphology (Fig. 6(a)). The addition of MA gas molecules led to reversible reactions with MAPbI$_3$, resulting in the formation of a liquid MAPbI$_{3-x}$CH$_3$NH$_2$ intermediate phase before rapidly forming a smooth and pinhole-free MAPbI$_3$ perovskite film surface as the MA gas molecules escaped. This method was fast and simple, successfully healing defects on the surface and interface of the perovskite film, and thus increasing the PCE of PSCs from 5.7% to 15.1%. However, this method often resulted in small grains due to the rapid nucleation rate caused by the spontaneous volatilization of MA gas molecules in liquid intermediates [81]. To address this issue, Zhang et al. heated the films based on a methylamine atmosphere treatment, which caused MAPbI$_3$ to recrystallize at high temperatures, resulting in larger and more uniform grain sizes [82]. This thermally induced recrystallization technique in the presence of an MA atmosphere resolved the growth process issue and reduced defects at the grain boundaries [83]. In addition to the post-atmospheric treatment of the perovskite film surface, MA gas molecules can interact with
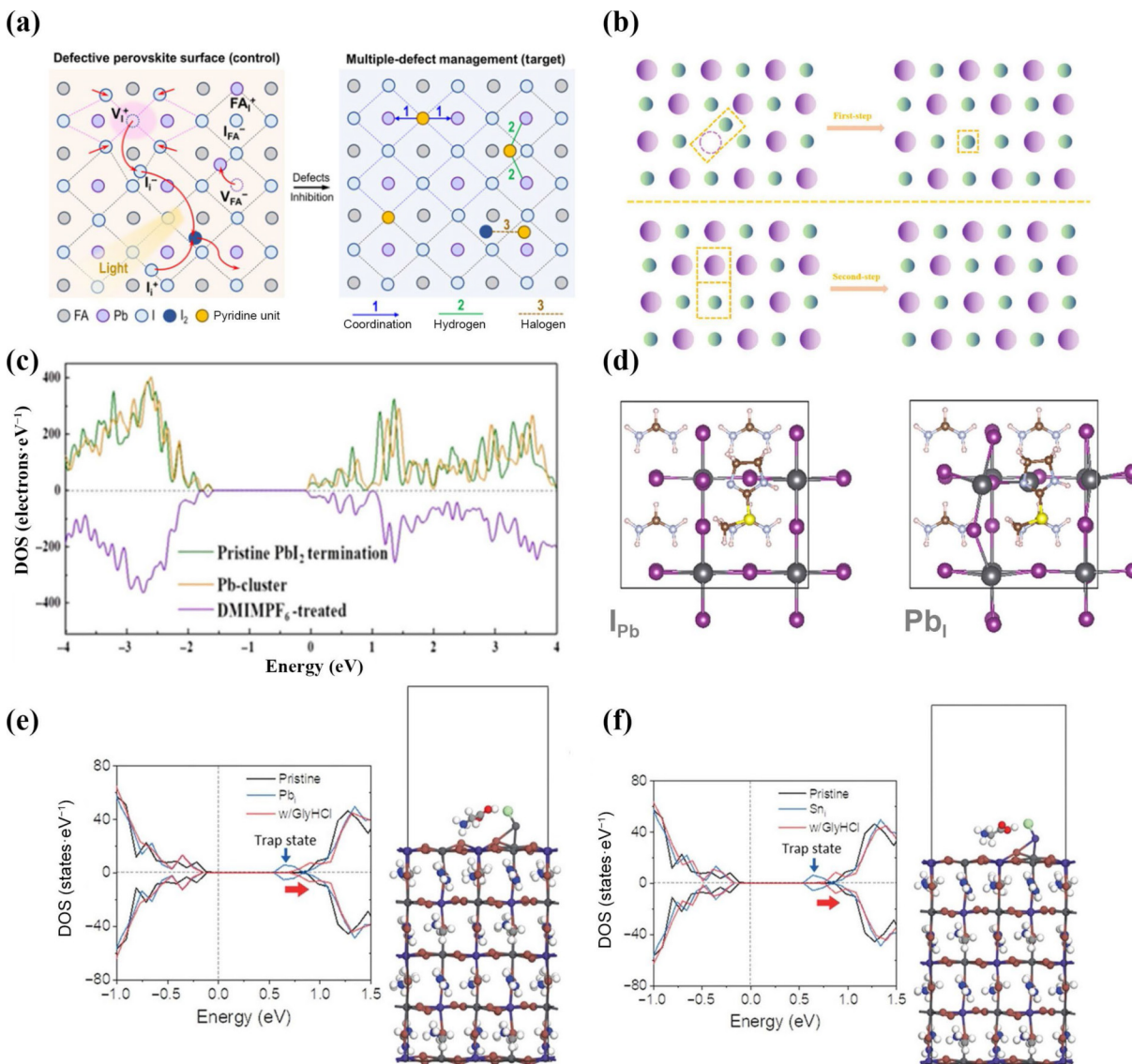
**Figure 5** (a) Planform showing multiple-defect management for the prototypical defective FAPbI$_3$ surface. Reproduced with permission from Ref. [75], © American Chemical Society 2021. (b) The proposed schematic diagram of defect-regulation processes. (the green and purple balls present Pb atoms I atoms, respectively). Reproduced with permission from Ref. [79], © Wiley-VCH GmbH 2021. (c) DOS of the pristine PbI$_2$ surface and Pb-I antisite surface with and without DMIMPF$_6$ treatment. Reproduced with permission from Ref. [78], © Wiley-VCH GmbH 2020. (d) Theoretical models of perovskite with molecular surface passivation of I$_{Pb}$ and Pb$_I$ antisite defects with MT-Im. Reproduced with permission from Ref. [77], © American Chemical Society 2021. DOS of (e) Pb$_i$ and (f) Sn$_i$ before and after GlyHCl introduction, and the optimized structure after the incorporation of GlyHCl. Note that DOS were aligned with the deep lying state of the pristine system. Pb, Sn, I, C, N, and H are indicated in dark gray, purple, brown, gray, blue, and white, respectively. Reproduced with permission from Ref. [72], © Wiley-VCH GmbH 2021.

the HPbI$_3$ precursor layer to create high-quality HPbI$_3$ crystals. Cui et al. used an antisolvent crystallization technique based on stoichiometric PbI$_2$/HI precursors to form HPbI$_3$ crystals [84]. When they exposed HPbI$_3$ to an MA atmosphere and then removed the MA gas, they observed that HPbI$_3$ transitioned from a pale yellow phase to a black phase (Fig. 6(d)). This process facilitated the formation of HPbI$_3$ through a strong acid-promoted pathway, as opposed to the conventional MAPbI$_3$ creation, where the MA gas had the largest surface area in contact with HPbI$_3$ without thermal induction. Meanwhile, the Pb-I structure in the HPbI$_3$ was preserved below the MA atmosphere, reducing iodine vacancies and enhancing the film quality. Thus, the production of MAPbI$_3$ perovskite films using this method had the potential to yield larger grains and limit the buildup of defects at the grain borders. Interestingly, Qi et al. prepared pinhole-free, low surface roughness and fully covered chloride-containing perovskite films through the synergistic effect of MA gas and partial substitution of iodide ions by chloride ions (Fig. 6(b)) [85]. The resulting PSCs achieved a PCE of 19.1% ± 0.4% with excellent reproducibility.

The slow breakdown of the MAPbI$_3$ layer and the accompanying very viscous liquid phase of the MA-perovskite cause slow diffusion near the surface, where recrystallization has already begun even though the perovskite surface is not yet completely covered. Huang et al. achieved complete reconstruction and repair of the perovskite films under combined treatment with methylamine gas and hot solvent vapor [82]. Using two different atmospheric treatments, they considered whether to turn the sample over for subsequent processing after atmospheric treatment and annealing. Comparing the films created using the two techniques revealed that the second approach produced a nearly flawless perovskite film surface (Fig. 6(c)). By flipping the film for the subsequent annealing stage, the MA could thoroughly react with the MAPbI$_3$ film, rapidly covering the surface of the perovskite film aided by gravity and recrystallizing from the margins as the MA departs, resulting in a perfect perovskite film state. Manipulating the nucleation and growth state of MAPbI$_3$ perovskite in the liquid state also allowed the achievement of perfect perovskite surfaces. Yuan et al. introduced self-generated
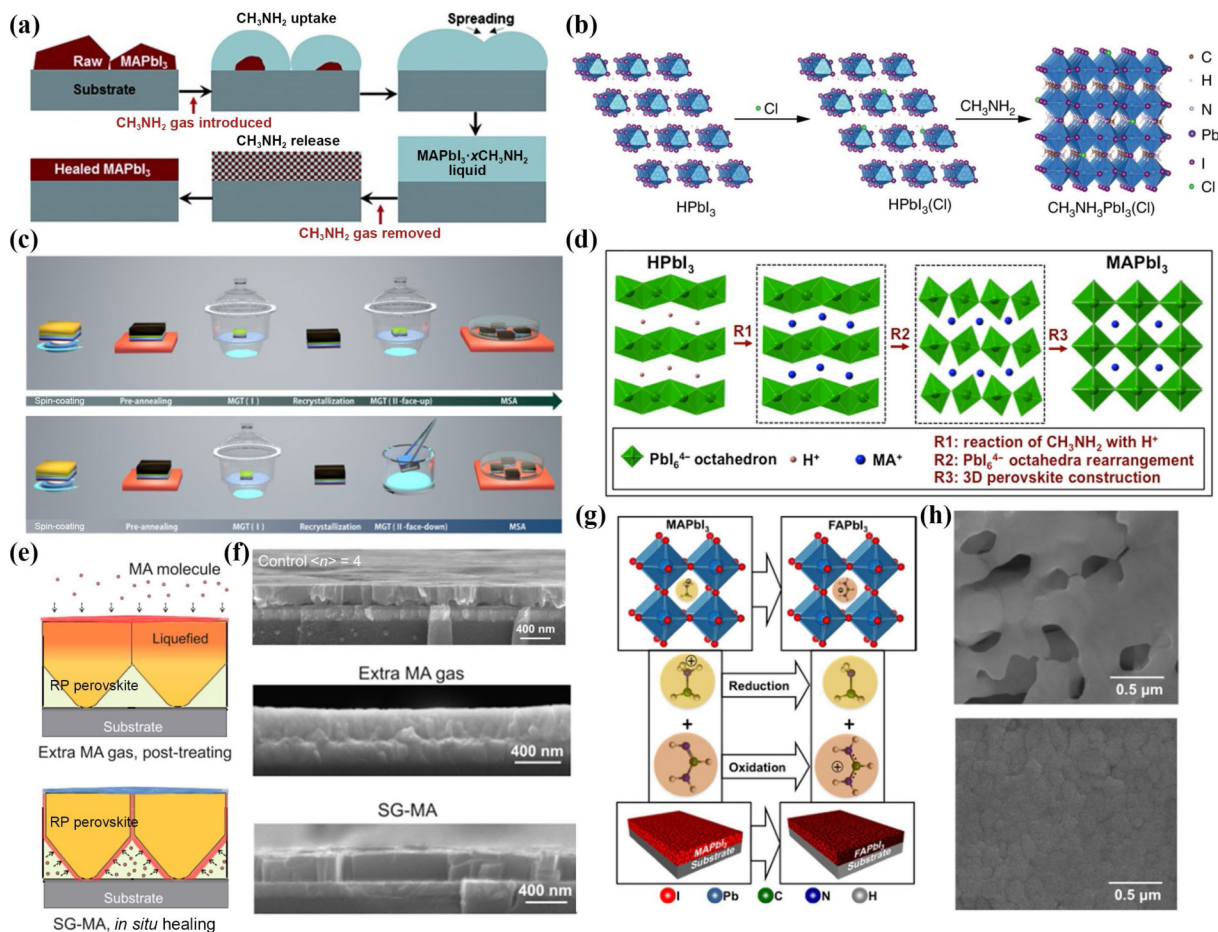
**Figure 6** (a) Schematic illustration of the mechanisms involved in the MIDH of MAPbI$_3$ perovskite films. Reproduced with permission from Ref. [80], © Wiley-VCH Verlag GmbH & Co. KGaA, Weinheim 2015. (b) Schematic drawing showing the reaction process of partial substitution of iodine ions by chorine ions to form chlorine-incorporated perovskite MAPbI$_3$(Cl) films. Reproduced with permission from Ref. [85], © Liu, Z. H. et al. 2018. (c) Schematic diagram of the two gas therapy modalities. Reproduced with permission from Ref. [82], © American Chemical Society 2020. (d) Schematic illustration of crystallographic conversion from HPbI$_3$ to MAPbI$_3$ upon reaction with CH$_3$NH$_2$. Reproduced with permission from Ref. [84], © American Chemical Society 2016. (e) Schematic illustration of the RP perovskite with extra MA gas post-treatment and SG-MA *in situ* healing. Reproduced with permission from Ref. [86], © American Chemical Society 2021. (f) Cross-sectional scanning electron microscope (SEM) images of the control and BA$_2$MA$_3$Pb$_4$I$_{13}$ RP perovskite films prepared by additional MA gas post-treatment and SG-MA methods, respectively. Reproduced with permission from Ref. [86], © American Chemical Society 2021. (g) Cation displacement reaction between MAPbI$_3$ perovskite and HC(=NH)NH$_2$ (formamidine or FA) gas at 150 °C resulting in FAPbI$_3$ perovskite and CH$_3$NH$_2$ (methylamine or MA) gas, and schematic illustration depicting morphology-preserving MAPbI$_3$ → FAPbI$_3$ perovskite thin-film conversion. Reproduced with permission from Ref. [87], © American Chemical Society 2016. (h) SEM images of raw FACsPbI$_3$ and NH$_3$-FACsPbI$_3$ perovskite films. Reproduced with permission from Ref. [89], © Li, Z. P. et al. 2022.

MA gas to avoid nucleation in the liquid phase state by controlling the amount of MA gas generated [86]. They demonstrated that potential vacancy defects in BA and PEA-based RP perovskite films, which resulted in decreased trap density and higher interfacial adhesion, might be successfully repaired *in situ* using self-generated MA gas (Figs. 6(e) and 6(f)). In recent years, other gas molecules have also been studied. Padture et al. placed MAPbI$_3$ perovskite films in a confined space containing FA gas, resulting in the rapid replacement of MA$^+$ cations by FA$^+$ cations in the perovskite structure (Fig. 6(g)) [87]. The microstructural morphology of the original MAPbI$_3$ films could be preserved in the resultant FAPbI$_3$ perovskite films. Theoretically, α-FAPbI$_3$ is more efficient and thermally stable than MAPbI$_3$. As a result, FA-based perovskite can be treated using a gas-assisted approach, which improves device performance. However, the degradation of the perovskite layer occurred as a result of post-treatment healing of FA-based perovskite films using MA gas [88]. Peng et al. selected ammonia as the post-treatment gas for highly homogeneous and dense FA-based perovskite films [89]. The findings demonstrated that FA-based perovskite materials might be produced at low temperatures that successfully encouraged the absorption of sufficient ammonia molecules and the production of a liquid intermediate state, which could efficiently remove defects

like voids on the surface of perovskite films (Fig. 6(h)). Ultimately, the resulting perovskite solar cells with ammonia-assisted post-treatment achieved a PCE of 23.21% with excellent reproducibility. Additionally, the method was also used to prepare large-area cells with an effective area of 14 cm$^2$ and realize a PCE of more than 20%. Therefore, gas-assisted secondary growth on the surface of perovskite films produced a dense and pinhole-free perovskite film with significantly lower defect density, featuring uniform large-area perovskite film fabrication. It paves the way for straightforward and quick fabrication of effective and reliable perovskite devices.

### 3.1.3 Surface polishing treatment

Perovskite films prepared by the solution method often exhibited a disordered grain boundary structure with numerous defects, caused by nanocrystals generated on surfaces and amorphous phases at grain boundaries. These defects lead to poor surface quality and reduced film hardness. To address this, surface polishing techniques have been explored to remove non-homogeneous phase components and improve carrier transport capabilities. Huang et al. utilized mechanical (physical) polishing techniques to remove defective layers of the surface of perovskite films [90]. This resulted in a tougher surface with significantly

reduced defects and increased roughness, promoting better contact between the perovskite layer and the transport layer. However, mechanical polishing methods are expensive and challenging to control, risking damage to the internal perovskite structure. Hence, alternative polishing methods more suitable for general applications need to be explored.

Chemical polishing techniques are superior to molecular passivation and mechanical polishing methods in terms of eliminating non-chemical composition and surface defects and facilitating electron–hole extraction between the perovskite and transport layers. Surface defects on $CsPbI_3$ perovskite films can cause severe non-radiative recombination and give rise to a p-type characteristic on the $CsPbI_3$ surface, which affects electron extraction and hole blocking when in contact with electron transport layer (ETL) PCBM. To address this issue, Fang et al. developed a technique using 1,4-butanediamine polishing treatment to eliminate the Pb-poor surface of $CsPbI_3$ perovskite films [91]. The Pb-poor surface had three common defects, $I_{Pb}$ and $V_{Pb}$ being deep energy level traps (Fig. 7(a)) [41]. The polishing treatment significantly improved the surface state (Fig. 7(b)) and energy level alignment, resulting in a noticeable increase in the efficiency of $CsPbI_3$ PCSs from 12.64% to 19.84% (Fig. 7(d)). The presence of $PbI_2$ on the surface of perovskite films is beneficial for grain enlargement, reducing halide vacancies and passivating defects on grain boundaries [92]. Additionally, a moderate amount of $PbI_2$ can inhibit the formation of δ-phase perovskite, thereby promoting the growth of more orientated α-phase perovskite crystals [93]. However, poorly regulated $PbI_2$ can induce considerable $Pb_i$ and severe non-radiative combinations on the perovskite surface. To end this, Zhu et al. used an extra layer produced by the *in situ* interaction between $PbI_2$ and the ammonium salt of the chemical polishing agent to optimize the effect of $PbI_2$. They then removed the excess $PbI_2$ from the perovskite surface through chemical polishing techniques (Fig. 7(c)) [94]. This chemical polishing not only passivated surface defects but also effectively regulated the energy level alignment of the perovskite/transport layer without introducing other impurities, leading to high device efficiencies of 24.5% (Fig. 7(e)).

However, additional indispensable chemical solvents in chemical polishing may affect the properties of perovskite films and complicate the preparation process. Therefore, considering the detrimental effect of solvents on perovskite, the researchers have explored a non-contact polishing method known as laser polishing. The utilization of short-wavelength laser irradiation with appropriate parameters not only avoids the decomposition of the perovskite but also ameliorates the quality of perovskite films [95, 96]. Fang et al. first proposed a new excimer laser surface modification (ELSM) method to reduce the surface defects of the perovskite films by laser irradiation [97]. This simple and effective method enables polishing of the perovskite surface within a few seconds, inhibiting the charge recombination at the interface of the perovskite and charge-transport layer, thus improving the performance of the PSCs. Thereafter, Guo et al. polished the perovskite surface with a high-intensity femtosecond (fs) laser to
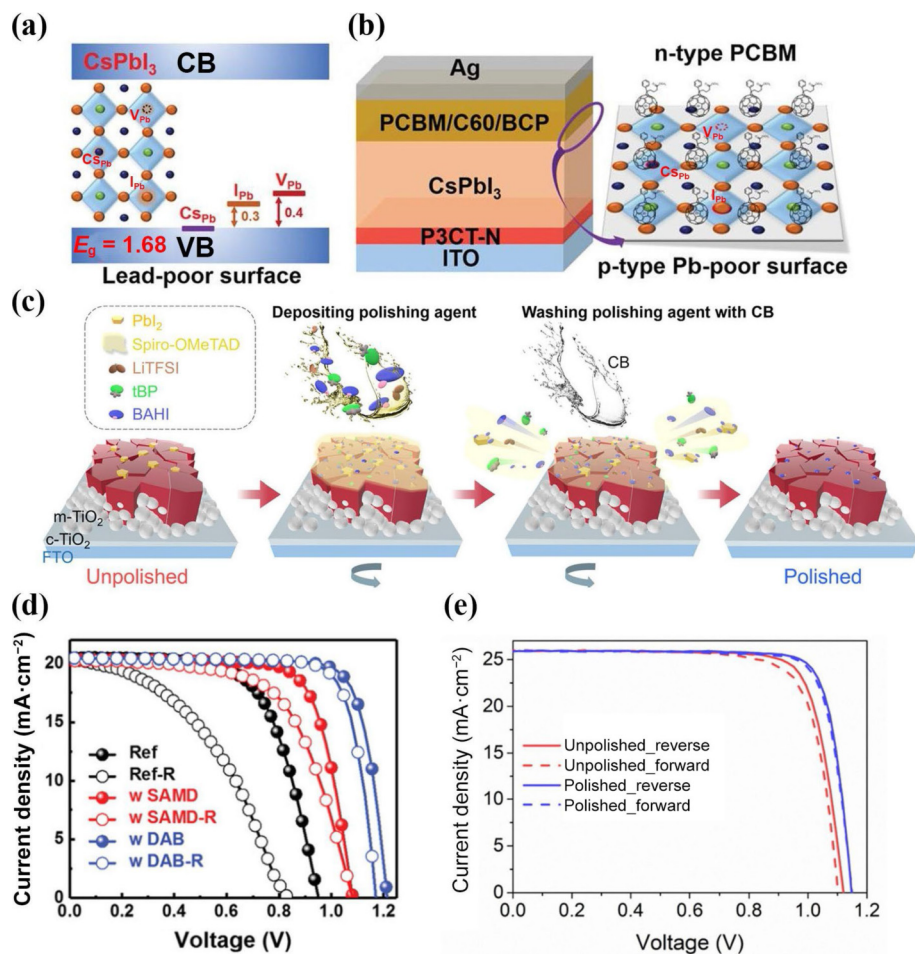


**Figure 7** (a) Theoretically simulated electronic states of lead-poor relevant traps in $CsPbI_3$ band energy levels. (b) Schematic diagram of the hindered electronic transport at cathode interface for the lead-poor surface. Reproduced with permission from Ref. [91], © Wiley-VCH GmbH 2022. (c) *J–V* curves of the champion device of each condition and the R and F symbols represent the reverse and forward scanning directions. Reproduced with permission from Ref. [94], © American Chemical Society 2022. (d) *J–V* curves in reverse and forward scanning directions of the champion PSCs based on unpolished and polished perovskite films. Reproduced with permission from Ref. [91], © Wiley-VCH GmbH 2022. (e) Schematic illustration of the chemical polishing process. Reproduced with permission from Ref. [94], © American Chemical Society 2022.

minimize the defect density on the perovskite surface [98]. The fs polishing technique removed approximately 20 nm from the top layer of perovskite, through an ultrafast ionization process, leading to the reduction of the grain boundary density and the increase of the grain size. The fs laser has the potential to damage the lattice structure of the perovskite by polishing it, and using a lower power laser may reduce the disruption to the perovskite. Therefore, Saliba et al. introduced a nanosecond (ns) pulsed UV laser to focus the laser on the top surface of the perovskite for raster scanning [99]. By controlling the laser energy and scanning speed, the photophysical properties of the surface could be improved without compromising the thickness of the film. This approach resulted in a $V_{oc}$ reaching 1.21 V by reducing surface recombination losses with an optimized perovskite/transport interface. These laser polishing methods compared to the prevalent chemical passivation layers can provide new perspectives for efficient, stable, and scalable fabrication of large-area or flexible PSCs. The main innovative advances in defect moderation on the perovskite surface and interface are summarized in Table 1 and the graphical summary of PCE breakthroughs over the years is presented in Fig. 3(b) [65, 84, 94, 100–104].

### 3.2 Dimensional engineering and structural stability

Despite the rapid progress in achieving high PCE performance, long-term stability issues arise due to unintentional phase structure degradation and inhomogeneous spatial distribution of components induced by ion motion from the surface. To address these challenges and pave the way for practical applications, low-dimensional perovskite structures have shown promise. These structures possess remarkable hydrophobic properties and effectively suppress ion migration from large organic cations. In this section, we present our approach to modulating the surface and grain boundaries of 3D perovskite by incorporating low-dimensional perovskite, offering a new direction for the development of highly stable PSCs (Fig. 8(a)) [61, 105–110].

*3.2.1   2D/3D hybrid dimensional structure*

2D perovskite demonstrates excellent stability with good hydrophobicity and high ion diffusion barriers [111]. To achieve both high efficiency and stability in PSCs, it is essential to combine 2D perovskite with 3D perovskite while delicately balancing their structures. This combination can be achieved through methods such as bulk doping and surface treatment to modify the grain boundaries and surfaces of 3D perovskite. In 2D/3D perovskite structures, the 2D phase is preferentially located at the grain boundaries of 3D perovskite [112], and an interfacial layer of 2D perovskite is formed on the 3D perovskite surface during the nucleation and growth [113]. Cao et al. applied β-guanidinylpropionic acid (β-GUA) molecules as additives in MA-free perovskite solutions to promote the formation of 2D/3D perovskite [114]. The grain boundaries of 3D perovskite allowed most of the 2D phases to be embedded, distributed over half of the thickness of the 3D perovskite film (Fig. 9(a)). The coupling of 2D and 3D perovskite resulted in superior water intrusion inhibition (Fig. 9(f)). In addition to the direct addition of 2D perovskite solution, the formation of 2D perovskite by reaction with $PbI_2$ between the 3D perovskite grain boundaries is essential to improve the PCE of PSCs. Liu et al. developed a simple approach using an ultra-thin 2D perovskite to terminate $CsPbI_3$ grain boundaries without damaging the original 3D perovskite [115]. They first deposited a $CsPbI_3$ layer containing excess $PbI_2$ and formed a template of $PbI_2$ at the grain boundaries, and then treated with a PEAI/isopropyl alcohol (IPA) solution, which induced the reaction of the PEAI solution with $PbI_2$ at the grain boundaries to form a 2D phase. The moisture stability of the 2D

terminated $CsPbI_3$ films was significantly improved due to the ability of the 2D perovskite to prevent the penetration of moisture and oxygen into the GBs while inhibiting ionic migration. As a result, the initial PCE of the unencapsulated device could be maintained at ≈ 81% after 84 h of storage at 40% ± 5% relative humidity (Fig. 9(g)). Other researchers have also improved device performance by gradually substituting components in the original 3D perovskite with new molecules, resulting in 2D perovskite encircling the original 3D grains to form a tighter encapsulation film [116, 117]. However, irregular crystal orientation and insulating properties of the 2D perovskite layers can reduce the efficiency of charge transfer between adjacent layers [118]. To address this, Li et al. demonstrated a localized 2D-3D mixed perovskite, in which the 2D perovskite was formed on the localized surface of 3D perovskite without fully covering it (Fig. 9(b)) [119]. This configuration was more conducive to hole transfer than the horizontal one due to the insulating organic spacer cations and random orientation of 3D perovskite. For incomplete coverage of the underlying 3D film, holes could be removed to the hole transport layer (HTL) even if the 2D perovskite layer was horizontally located on the 3D film surface. However, an undesirable quasi-2D phase that negatively affects the PCE and stability of the PSCs is inevitably created by the formation of 2D/3D layers in these methods [120]. For this purpose, Noh et al. developed a new method using a solvent-free solid-phase in-plane growth (SIG) approach to create 2D/3D layers [121]. A solid 2D film was placed on top of a 3D perovskite layer so that their surfaces were contacted. Next, pressure and heat were applied downward from above, which caused the 2D perovskite of the solid 2D perovskite film to transfer to the 3D perovskite layer (Fig. 9(e)). This approach avoided the generation of quasi-2D perovskite with large band gaps, resulting in 2D/3D perovskite devices with a $V_{oc}$ of 1.185 V and a PCE of 24.35%. The encapsulated devices maintained 94% of their initial efficiency after 1056 h in a damp heat test (85 °C/85% relative humidity).

In general, 2D perovskite can serve as both an additive and a surface post-treatment additive, effectively enhancing the stability of the perovskite films. Gharibzadeh et al. developed a strategy for double passivation of grain boundaries and surfaces using phenethylammonium chloride (PEACl) to treat grain boundaries and perovskite/$C_{60}$ interfaces (Fig. 9(c)) [122]. Through thermal conductivity spectroscopy (TAS), they demonstrated a significant increase in the activation energy for ion migration after double treatment, leading to enhanced device stability under maximum power point (MPP) tracking and 1000 h heat treatment (Fig. 9(h)). Furthermore, Gao et al. designed a strategy by introducing the 2-(2-pyridyl)ethylamine (2-PyEA) molecule into the perovskite (Fig. 9(d)) [123]. As an additive and post-treatment solvent, 2-PyEA promoted 2D@3D perovskite and 3D/2D perovskite generation, respectively, resulting in a 2D@3D/2D perovskite structure. This significantly increased the contact angle of 3D perovskite films from 53.5° to 72.9° and greatly improved the hydrophobicity of the perovskite films. Therefore, incorporating 2D perovskite into 3D perovskite structure is an effective approach to enhance the stability and efficiency of PSCs. This method not only passivates surface and interfacial defects but also functions as a hydrophobic and insulating layer, preventing the infiltration of water and oxygen.

*3.2.2   1D/3D hybrid dimensional structure*

As aforementioned, the 2D perovskite is effective in improving the stability of 3D perovskite. However, the large interlayer distance of 2D perovskite with long-chain organic cations may hinder charge extraction from 3D perovskite to neighboring CTL, thus reducing the PCE. In addition, the 2D structures formed on the 3D surfaces

**Table 1** Summary of innovative development of the passivation of surface defects in PSCs

| | Year | Device structure | Materials | Type of defect | Strategic and approach | Results | References |
|---|---|---|---|---|---|---|---|
| Chemical coordination of surface defects | 2021 | FTO/c-TiO$_2$/m-TiO$_2$/ Rb$_{0.05}$Cs$_{0.05}$MA$_{0.15}$FA$_{0.75}$ Pb$_{1.05}$(I$_{0.95}$Br$_{0.05}$)$_3$/Spiro-OMeTAD/Au | 3-Phosphonopropionic acid (H3pp) organic molecule | Shallow point defect | The strong interaction between the perovskite and the H3pp molecule through two types of hydrogen bonds (H···I and O···H) | PCE = 21% | [38] |
| | 2021 | ITO/PEN/HfO$_x$/ Rb$_{0.05}$Cs$_{0.05}$(FA$_{0.83}$ MA$_{0.17}$)$_{0.9}$Pb(I$_{0.95}$Br$_{0.05}$)$_3$/ Spiro-OMeTAD/Au | Artemisinin | Uncoordinated Pb ions | Passivate the perovskite grains via the interaction between the carbonyl groups of artemisinin and uncoordinated Pb ions | PCE = 21.10% | [39] |
| | 2022 | ITO/SnO$_2$ + Gd/perovskite/Spiro-OMeTAD/Au | Rare earth element Gd | Oxygen vacancy defects of the SnO$_2$ | Doping with Gd ions to passivate oxygen vacancy defects at the SnO$_2$ interface | PCE = 22.40% | [201] |
| | 2021 | FTO/c-TiO$_2$/m-TiO$_2$/ FAPbI$_3$/OAI/ Spiro-OMeTAD/Au | Pseudo-halide anion formate (HCOO$^-$) | Anion-vacancy defects | Introducing 2% formamidine formate (FAHCOO) into the precursor solution | PCE = 25.6% | [65] |
| | 2022 | FTO/TiO$_2$/CsPbI$_3$/Spiro-OMeTAD/Au | 1-Ethyl-3-methyl-imidazolium hydrogen sulfate (EMIMHSO$_4$) | Undercoordinated Pb$^{2+}$; iodine vacancy defects | A low concentration of ionic liquid, EMIMHSO$_4$, was introduced into perovskite film | PCE = 20.01% | [67] |
| | 2022 | ITO/PEDOT:PSS/ FASnI$_3$/C$_{60}$/BCP/Ag | 6-Maleimidohexanehydrazide trifluoroacetate | Undercoordinated Sn$^{2+}$; Sn interstitials; Sn-I antisites | Surface reconstruction strategy with 6-maleimidohexanehydrazide trifluoroacetate | PCE = 13.64% | [68] |
| | 2022 | — | Benzene additive with delocalized electron | Electron-donating FA-interstitial and Pb-interstitial defects | Investigated intrinsic point defect formations in FAPbI$_3$ surface with four types of terminations, PbI$_2$, FA$_I$, and Pb$_I$ | Benzene additive with delocalized electron distribution can effectively passivate the deep FA-interstitial and Pb-interstitial defects | [71] |
| | 2022 | ITO/Cs$_{0.05}$MA$_{0.45}$FA$_{0.5}$ Pb$_{0.5}$Sn$_{0.5}$I$_3$/PCBM/ C$_{60}$/BCP/Ag | Copper thiocyanate (CuSCN) and glycine hydrochloride (GlyHCl) | Sn-interstitial and Pb-interstitial defects | A binary additive system composed of CuSCN and GlyHCl | PCE = 18.6% | [72] |
| | 2022 | FTO/SnO$_2$/FAPbI$_3$/ Spiro-OMeTAD/Au | 3-Sulfopropyl methacrylate potassium salt additive | Undercoordinated Pb$^{2+}$; point defects and Pb clusters | Employed 3-sulfopropyl methacrylate potassium salt as a multifunctional additive to assist grain growth | PCE = 22%; EQE$_{EL}$ = 12.2% | [74] |
| | 2022 | ITO/SnO$_2$/FAPbI$_3$/ Spiro-OMeTAD/Au | Pyridine-containing polymeric agent | V$_{FA}^-$, V$_{MA}^-$, V$_I^+$, FA$_I^+$, I$_{FA}^-$, I$_i^+$ | Three kinds of chemical bonding enabled by polymeric P4VP atop the defective surface of perovskite polycrystalline films | PCE = 22.02%, planar devices | [75] |
| | | FTO/c-TiO$_2$/ FAPbI$_3$/Spiro-OMeTAD/Au | | | | PCE = 23.14%, mesoporous devices | |
| | 2021 | ITO/SnO$_2$/ (Cs$_{0.03}$FA$_{0.97}$PbI$_3$)$_{0.95}$ (MAPbBr$_3$)$_{0.05}$/MT-Im/Spiro-OMeTAD/Au | 2-Methylthio-2-imidazoline (MT-Im) | Pb-I antisite defexts; uncoordinated Pb$_0$ defects | A LDP by an amphoteric heterocyclic cation, increase the defect formation energies and inhibit the generation of Pb-I antisite defects. | PCE = 24.07% | [77] |
| | 2021 | FTO/NiO/Cs$_{0.08}$FA$_{0.92}$Pb I$_3$/DMIMPF$_6$/Spiro-OMeTAD/Au | 1,3-Dimethyl-3-imidazoliumhexafluor ophosphate (DMIMPF$_6$) ionic liquid | Pb-cluster and Pb-I antisite defects | [DMIM]$^+$ bonding with the Pb$^{2+}$ ion on the perovskite surface, leading to significantly suppressed nonradiative recombination | PCE = 23.25% | [78] |
| Gas-assisted surface secondary growth | 2015 | FTO/c-TiO$_2$/ MAPbI$_3$/HTM/Ag | Methylamine gas | Voids and pinholes | Secondary growth of MAPbI$_3$ perovskite crystal surface by introduction of MA gas | PCE = 15.1% | [80] |
| | 2018 | FTO/c-TiO$_2$/m-TiO$_2$/ MAPbI$_3$(Cl)/Spiro-OMeTAD/Au | Methylamine gas | Voids and pinholes | Fast gas–solid reaction of chlorine-incorporated hydrogen lead triiodide (HPbI$_3$(Cl)) and CH$_3$NH$_2$ gas | PCE = 19.1% ± 0.4% | [85] |

(Continued)

| | Year | Device structure | Materials | Type of defect | Strategic and approach | Results | References |
|---|---|---|---|---|---|---|---|
| Gas-assisted surface secondary growth | 2020 | ITO/SnO$_2$/MAPbI$_3$/ Spiro-OMeTAD/Ag | Methylamine gas and hot solvent vapors | Voids and pinholes | A joint treatment of methylamine gas and hot solvent vapors | PCE = 19.2% | [82] |
| | 2021 | ITO/PEDOT:PSS/ BA$_2$MA$_{n-1}$Pb$_n$I$_{3n+1}$/ PCBM/BCP/Cu | Methylamine gas | Irregular nanocavities | Self-generated methylamine gas, by a replacement reaction in solution, is introduced to *in situ* heal these irregular nanocavities | PCE = 13.1% | [86] |
| | 2016 | FTO/c-TiO$_2$/ m-TiO$_2$/MAPbI$_3$/ Spiro-OMeTAD/Ag | Formamidine gas | Voids and pinholes | Exposure MAPbI$_3$ thin films to FA gas at 150 °C, displacement of the MA$^+$ cations by FA$^+$ cations | PCE = 18% | [87] |
| | 2018 | FTO/c-TiO$_2$/m-TiO$_2$/ gMA$_{0.8}$FA$_{0.2}$PbI$_3$/ Spiro-OMeTAD/Au | Methylamine gas | Vacancy defects; voids | Exposed the MA$_x$FA$_{1-x}$PbI$_3$ perovskite films to the MA vapor to heal the film defects | PCE = 21% | [88] |
| | 2022 | FTO/TiO$_2$-SnO$_2$/NH$_3$-FACsPbI$_3$/Spiro-OMeTAD/Au | Ammonia | Voids | NH$_3$ is selected as a post-healing gas to avoid the degradation of the FA-based perovskite phase during the post treatment | PCE = 23.21%; PCE = 20% (area = 14 cm$^2$) | [89] |
| Surface polishing treatment | 2021 | ITO/PTAA/Cs$_{0.4}$FA$_{0.6}$Pb (I$_{0.64}$Br$_{0.36}$)$_3$/PCBM/ C$_{60}$/Cu | — | Dislocations or twin boundaries; nanostructured layer | Removing the defective surface layer through mechanical polishing | Retain 93% of initial efficiency after continuous illumination for 2180 h at 1 sun intensity and with ultraviolet radiation at 65 °C | [90] |
| | 2022 | ITO/P3CT-N/ CsPbI$_3$/PCBM/ C$_{60}$/BCP/Ag | 1,4-Butanediamine | Cs$_{Pb}$, V$_{Pb}$, and I$_{Pb}$ defects | 1,4-Butanediamine (DAB) surface treatment | PCE = 19.84% | [91] |
| | 2022 | FTO/c-TiO$_2$/m-TiO$_2$/ FA$_{0.90}$MA$_{0.10}$PbI$_3$· (CsPbI$_3$)$_{0.05}$/HTL/Ag | Benzylamine hydroiodide | PbI$_2$ | Adding BHAI to HTL as a chemical polishing agent | PCE = 24.5% | [94] |

usually contain phases with different *n* values, resulting in an inability to control the phase distribution of 2D perovskite, which affects the transport between 3D perovskite and the transport layer [124, 125]. To further increase stability in the PSCs, attention has shifted to 1D perovskite, which has a more flexible structure with small organic conjugated molecules, providing excellent charge transport properties [126, 127]. Due to its near-ideal band gap of 1.47 eV and superior crystallinity, FAPbI$_3$ is frequently employed as an absorber layer for PSCs and recently achieved an efficiency of 26.1%. However, the black phase α-FAPbI$_3$ is unstable at room temperature and easily converts to the fragile and easily degraded yellow phase δ-FAPbI$_3$ [106]. To address this, preventing the production of δ-FAPbI$_3$ is crucial to boost the overall performance and stability of FAPbI$_3$ devices. Li et al. obtained the first novel 1D/3D hybrid dimensional structure with stabled α-FAPbI$_3$ by incorporating hydrazine cations (HA$^+$) into FAPbI$_3$-based perovskite [106]. They made HA$^+$ cations preferentially reacting with [PbI$_6$]$_4^-$ of the 3D perovskite and formed a 1D-HA phase at the grain boundary of the 3D perovskite through a cation exchange mechanism, which inhibited the FA$^+$ reaction to form δ-FAPbI$_3$ and improved the stability of the device (Fig. 10(f)). Besides, the formation of the 3D polycrystalline perovskite films required thermal annealing, resulting in compressive strain in the out-of-plane direction and tensile strain in the in-plane direction due to thermal expansion mismatch. The generation of strain decreases the activation energy of ion migration and accelerates the decomposition of perovskite. In the 3D single-crystal perovskite, electrostriction reactions occur due to their soft lattice properties with low Young's modulus (Ym) [128]. The electrostriction effect can cause lattice distortion and produce more Schottky and Frenkel defects, leading to more

severe ion migration. To address these issues, Li et al. first observed the electrostriction in 3D polycrystalline perovskite, which significantly affected the lattice strain under the electric field. They prepared 1D/3D structures to improve carrier extraction and transport in 3D perovskite by adding organic salt and bulk benzimidazole cations (Bn$^+$) [44]. Bn$^+$ induced 3D perovskite crystal growth and formed spatially distributed 1D BnPbI$_3$ perovskite in 3D perovskite films, compensating for dangling bonds and passivation defects, contributing to equilibrium extraction of carriers (Fig. 10(h)). Furthermore, 1D BnPbI$_3$ perovskite could suppress the electrostriction effect by increasing the Ym of the 3D perovskite, which effectively improved the lattice deformation and led to weakened ion migration. This approach also significantly reduced iodide ion diffusion to Ag electrodes in 3D perovskite devices, preventing corrosion of the electrodes. In 1D-3D perovskite devices, Ag electrode diffusion and iodide ion migration were effectively suppressed (Fig. 10(i)). To improve the stability of inorganic perovskite, Cs$^+$ cations can be used to resolve the volatility of organic cations due to their chemical inertness. Despite the 1D/3D CsPbI$_3$ hybrid dimensional structures increasing the stability of PSCs, the weak chemical inertness and volatility of Cs$^+$ cause inorganic perovskite to exhibit little activity in cation exchange [129]. Therefore, it is necessary to select molecules with high activity to achieve a strong cation exchange with Cs$^+$. To this end, Zhong et al. treated 3D CsPbI$_3$ perovskite films with ChI solution and formed 1D ChPbI$_3$ structures on the 3D CsPbI$_3$ surface (Fig. 10(e)) [130]. They found that 1D ChPbI$_3$ easily and spontaneously formed at room temperature. The formation of 1D ChPbI$_3$ not only exhibited strong passivation of surface defects but also significantly increased the stability of black-phase CsPbI$_3$
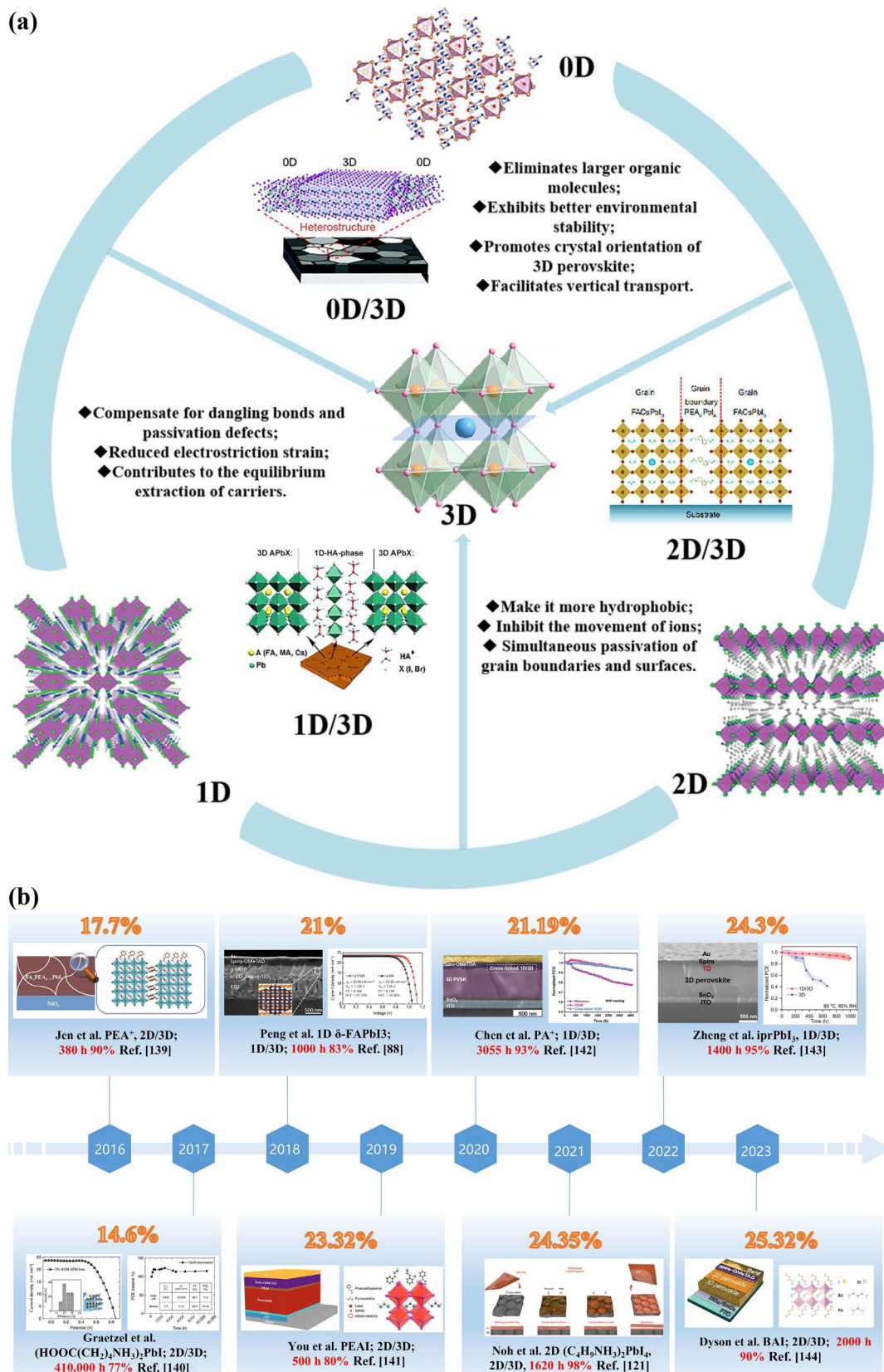
**(a)**



**(b)**



**Figure 8** (a) Summary of measures for the construction of different dimensional structures at the perovskite surface and interface. Construction of 0D and 3D perovskite structures. Reproduced with permission from Ref. [105], © Cui, B. B. et al. 2019. Reproduced with permission from Ref. [108], © The Royal Society of Chemistry 2020. Construction of 1D and 3D perovskite structures. Reproduced with permission from Ref. [106], © Elsevier B.V. 2020. Reproduced with permission from Ref. [107], © American Chemical Society 2018. Construction of 2D and 3D perovskite structures. Reproduced with permission from Ref. [61], © Sun, S. Q. et al. 2021. Reproduced with permission from Ref. [109], © Lee, J. W. et al. 2018. Reproduced with permission from Ref. [110], © American Chemical Society 2022. (b) The graphical abstract of related breakthrough works with reported maximum PCE for each year. Reproduced with permission from Ref. [121], © Jang, Y. W. et al. 2021. Reproduced with permission from Ref. [139], © WILEY-VCH Verlag GmbH & Co. KGaA, Weinheim 2016. Reproduced with permission from Ref. [140], © Grancini, G. et al. 2017. Reproduced with permission from Ref. [88], © WILEY-VCH Verlag GmbH & Co. KGaA, Weinheim 2018. Reproduced with permission from Ref. [141], © Jiang, Q. et al. 2019. Reproduced with permission from Ref. [142], © The Royal Society of Chemistry 2020. Reproduced with permission from Ref. [143], © Chen, R. H. et al. 2022. Reproduced with permission from Ref. [144], © Yang, W. C. et al. 2023.
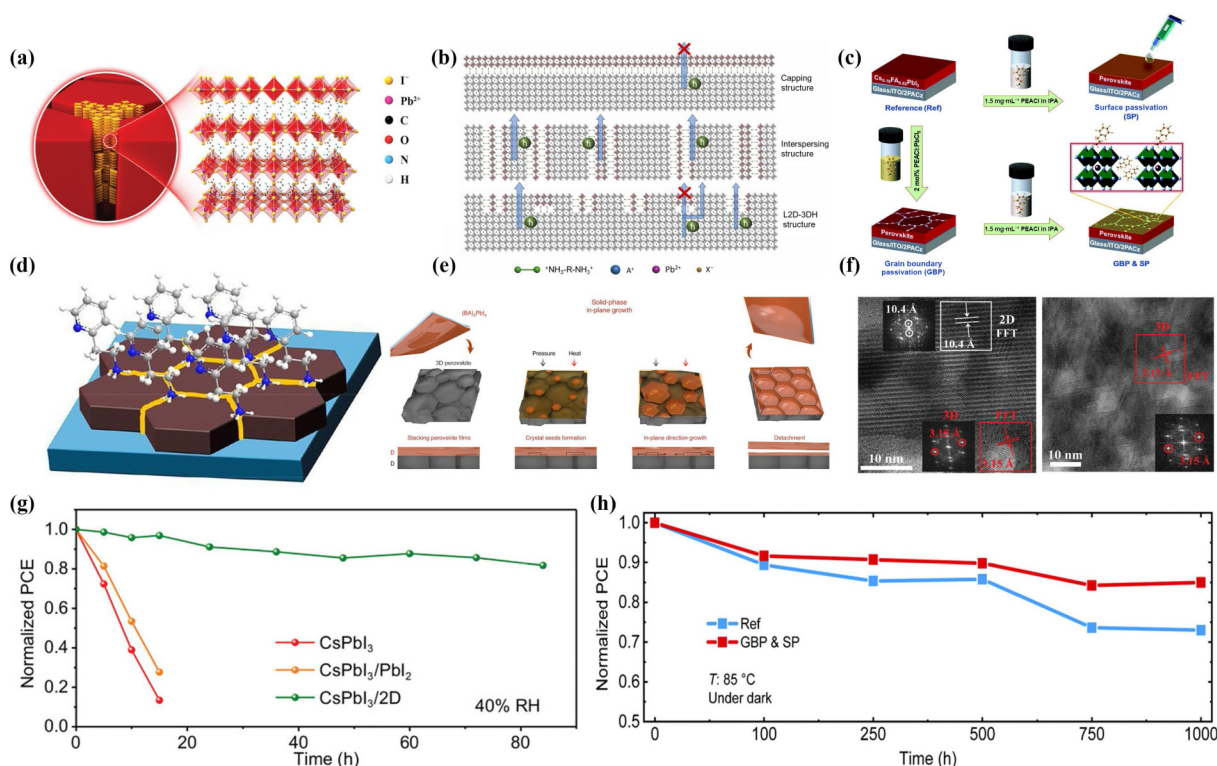
**Figure 9** (a) The diagram illustrates the crystal structure of 2D perovskite with *n* = 1. Reproduced with permission from Ref. [114], © WILEY-VCH Verlag GmbH & Co. KGaA, Weinheim 2020. (b) Illustration of charge transport in various structures of 2D–3D composite: capping structure, interspersing structure, and L2D–3DH structure. Reproduced with permission from Ref. [119], © Elsevier Ltd. 2021. (c) Schematic of the perovskite absorber deposition process employing the dual passivation strategy developed in this work: grain boundary passivation (GBP) by incorporation of PEACl:PbCl₂ into the perovskite precursor solution, SP by treatment of PEACl in IPA on top of the perovskite absorber layer and combination of grain boundary and surface passivation (GBP & SP). Reproduced with permission from Ref. [122], © The Royal Society of Chemistry 2021. (d) Schematic diagram of the 2D@3D/2D perovskite film. Reproduced with permission from Ref. [123], © American Chemical Society 2021. (e) Top-view and cross-sectional sketches of the manufacturing of a $(BA)_2PbI_4$ film on a 3D perovskite substrate via the SIG method. Reproduced with permission from Ref. [121], © Jang, Y. W. et al. 2021. (f) High-resolution cross-sectional transmission electron microscopy (TEM) images of the left and right sides of the β-GUA doped perovskite films, respectively. Reproduced with permission from Ref. [114], © WILEY-VCH Verlag GmbH & Co. KGaA, Weinheim 2020. (g) Long-term stability measurements of unencapsulated devices at 40 ± 5 RH%. Reproduced with permission from Ref. [115], © Wiley-VCH GmbH 2021. (h) Thermal stability of devices heated at temperature of 85 °C in dark condition inside of a glovebox. Data points were extracted from *J–V* curves at various time intervals. Reproduced with permission from Ref. [122], © The Royal Society of Chemistry 2021.

perovskite due to its chemical inertness and strong interaction with 3D perovskite (Fig. 10(g)).

In summary, the 1D/3D hybrid dimensional structure can form a 1D structure at the 3D perovskite surface and interface through a cation exchange mechanism. This structure binds to surface suspension bonds, passivates defects, improves lattice deformation, and inhibits ion migration on the 3D perovskite surface, thereby enhancing the stability of PSCs.

### 3.2.3 0D/3D hybrid dimensional structure

To achieve the highest stability and greater suitability for commercial applications, researchers combined 3D perovskite with 0D perovskite. The 0D perovskite is composed of isolated metal halide octahedral anions or metal halide clusters that are separated from each other by surrounding inorganic or organic cations without forming electronic bands (Fig. 10(a)) [131, 132]. In contrast, the 3D perovskite has large band dispersion and low exciton binding energy, which facilitates the dissociation of excitons. The 0D perovskite, with its strong quantum confinement effects and large exciton binding energy, imposes carrier localization on the structure, leading to the formation of localized Frenkel excitons that can effectively restrain the migration of electrons and holes [61].

$CsPbI_3$ has garnered much attention because of its suitable band gap (≈ 1.73 eV). However, the perovskite phase (α-/γ-$CsPbI_3$) is easily converted to the non-perovskite phase (δ-$CsPbI_3$) by certain spatial unit cell volume changes, thus limiting the

application of $CsPbI_3$ [133, 134]. To this end, Jen et al. used *in situ* dimensional modulation of the $CsPbI_3$ nanocrystals to form a system combining 0D $Cs_4PbI_6$ and 3D γ-$CsPbI_3$ perovskite, which improved the phase stability of $CsPbI_3$ (Fig. 10(b)) [135]. The 0D $Cs_4PbI_6$ coexisted with γ-$CsPbI_3$ in the prepared films and formed *in situ* around the 3D $CsPbI_3$ perovskite lattice as the wrapping layer, effectively solving the problem of phase instability. Lau et al. prepared 0D/3D $Cs_{4-x}K_xPbBr_6$/$CsPbBr_3$ heterostructured perovskite films by introducing KBr [136]. With this method, a type I heterostructure formed at the $Cs_{4-x}K_xPbBr_6$/$CsPbBr_3$ interface, promoting radiative recombination on the perovskite surface and interface. The excitons of the 0D perovskite were transported to the 3D phase in the 0D/3D heterostructured perovskite, but due to the inherent characteristics of the 0D perovskite, free excitation charge in the 3D perovskite was prevented from diffusing into the 0D phase (Fig. 10(c)). The formation of 0D/3D perovskite increased the carrier density within the perovskite grains and prevented free charge diffusion from being trapped and recombined at grain boundaries. Wang et al. recently introduced a lateral (0D/3D) $Cs_4PbI_6$/$FA_xCs_{1-x}PbI_3$ structure [137]. They discovered that $Cs^+$ from $Cs_4PbI_6$ might migrate to replace $FA^+$ in 3D perovskite grains through ion-exchanged with FA-rich $FA_xCs_{1-x}PbI_3$ perovskite in the 0D/3D structure, enhancing the stability of 3D perovskite (Fig. 10(d)). Additionally, the creation of 0D perovskite at 3D perovskite grains promoted the growth of low-defect $FA_xCs_{1-x}PbI_3$, leading to decreased non-radiative recombination and improved light
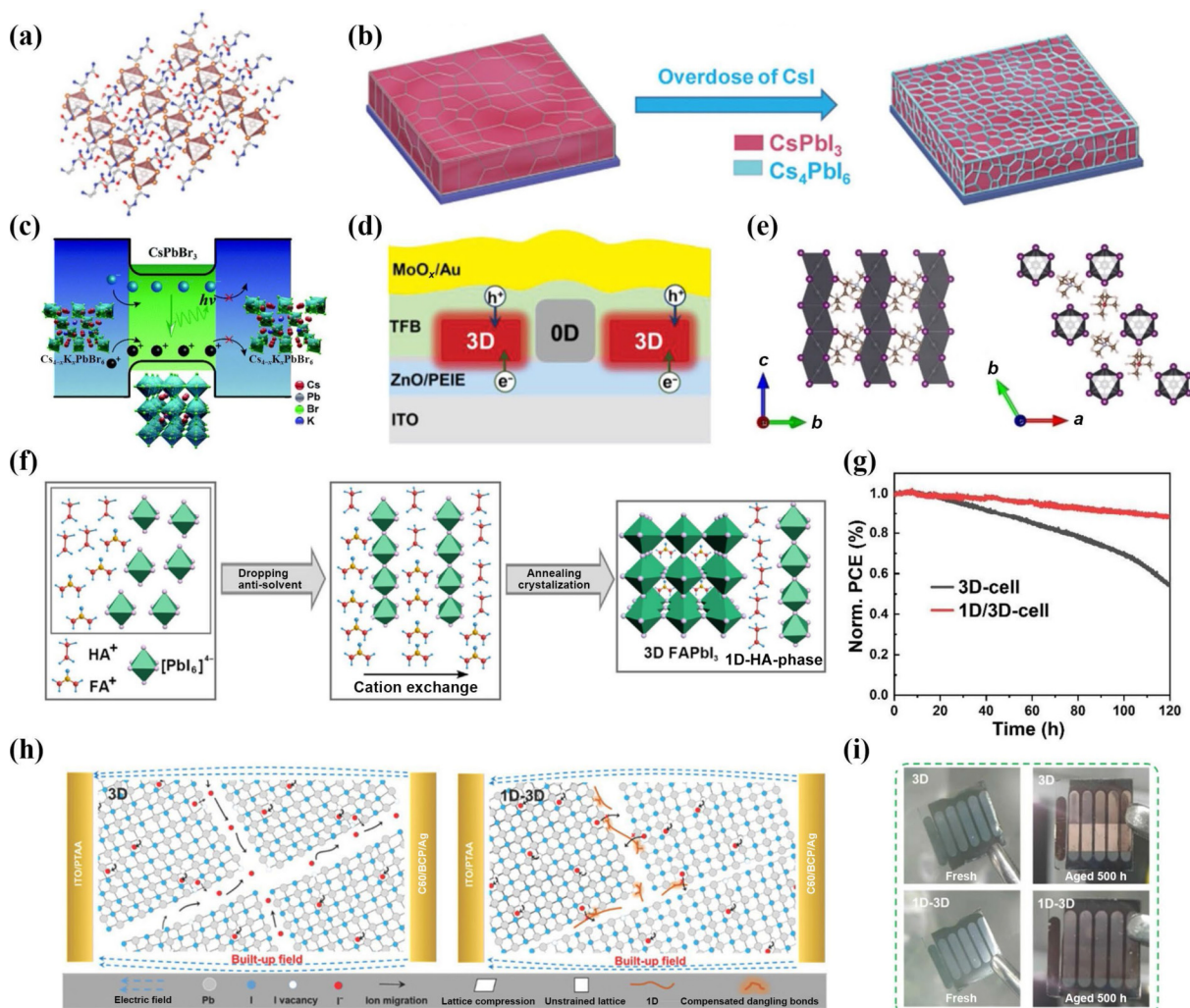
**Figure 10** (a) Typical single crystal structures of 0D organic–inorganic hybrid perovskite. Reproduced with permission from Ref. [131], © Han, Y. et al. 2021. (b) The structure schematic of $Cs_{1+x}PbI_{3+x}$ films. Reproduced with permission from Ref. [135], © WILEY-VCH Verlag GmbH & Co. KGaA, Weinheim 2019. (c) Carrier recombination diagram of 0D/3D perovskite heterostructure. Reproduced with permission from Ref. [136], © The Royal Society of Chemistry 2021. (d) Schematic diagram of the device structure. Holes and electrons injected into the phase-separated emitting layer are mainly transported via the $FA_xCs_{1-x}PbI_3$ crystallites. Reproduced with permission from Ref. [137], © Wiley-VCH GmbH 2023. (e) Schematic crystal structure of hexagonal $ChPbI_3$. Reproduced with permission from Ref. [130], © Wiley-VCH GmbH 2023. (f) Schematic of cation exchange process between $HA^+$ and $FA^+$. Reproduced with permission from Ref. [106], © Elsevier B.V. 2020. (g) Continuous MPP tracking for the 3D- and 1D/3D-cells with a continuous 1 sun irradiation (100 mW·cm$^{-2}$) with LED lamp in a $N_2$ environment. Reproduced with permission from Ref. [130], © Wiley-VCH GmbH 2023. (h) The schematic diagram of ion migration and lattice distortion deformation induced by the electro-strictive strain for the polycrystalline 3D and 1D–3D perovskite films. Reproduced with permission from Ref. [44], © Wiley-VCH GmbH 2021. (i) Photographs of the fresh and 500 h-aged 3D and 1D–3D devices. R Reproduced with permission from Ref. [44], © Wiley-VCH GmbH 2021.

extraction. Although the addition of 0D perovskite efficiently inhibited carrier migration at the 3D perovskite grain boundaries, addressing the challenges on the 3D perovskite surface remains an ongoing effort.

Excellent results can be achieved by combining various LD perovskite with 3D perovskite, utilizing the unique features of the LD perovskite to promote the extraction of carriers between the interfaces. Liu et al. developed a 3D-2D-0D hybrid dimensional interface to introduce an electric field on the back side of PSCs, leading to high-efficiency all-inorganic $CsPbBrI_2$ PSCs with improved stability [138]. The main innovative advances in moderating the dimensional structure of the perovskite surface and interface are summarized in Table 2 and a graphical summary of PCE breakthroughs each year is shown in Fig. 8(b) [88, 121, 139–144].

### 3.3 Energy regulation of the surface

The performance of charge transport is primarily influenced by the electric-field distribution under typical operating conditions of the PSCs, which are designed with a p-i-n or n-i-p heterojunction

structure. In these structures, the perovskite absorber layer is sandwiched between electron- and hole-selective contacts, and photogenerated free carriers generated in perovskite are driven by a built-in field and move toward the CTL. However, the inability to control the distribution of the electric field is caused by contact surfaces that behave as energy-dissipating channels due to misaligned energy band alignment or localized exponential-tail states of band edges. In this section, regulatory strategies related to Urbach band tails, homogeneous junctions, and heterogeneous junctions are discussed from the perspective of energy regulation (Fig. 11(a)) [145–147].

#### 3.3.1 Urbach tail caused by energy disorder

Urbach energy disorder results in photon emission due to energy disorder, which reduces the $V_{oc}$ and induces energy loss. To illustrate its influence on device performance, Jakapan et al. evaluated the $E_U$ for various types of solar cell films [51]. The relationship between the $E_U$ and device performance was also investigated. When $E_U$ increases, $V_{oc}$-deficit ($V_{oc, def}$) increases, thus $V_{oc}$ decreases, indicating an improvement in the quality of the film

**Table 2** Summary of innovative developments in dimensional regulation in PSCs

| | Year | Device structure | Materials | Strategic and approach | Results | References |
|---|---|---|---|---|---|---|
| 0D/3D hybrid dimensional structure | 2019 | ITO/SnO$_2$/nano-ZnO/Cs$_4$PbI$_6$/CsPbI$_3$/Spiro-OMeTAD/MoO$_3$/Ag | Cs$_4$PbI$_6$ | The formation of a heterostructure consisting of 0D Cs$_4$PbI$_6$ and 3D CsPbI$_3$ | PCE = 16.39% | [135] |
| | 2022 | ITO/PEDOT:PSS/Cs$_4$PbBr$_6$/CsPbBr$_3$:PEO:LiPF6/LiF/Al | Cs$_4$PbBr$_6$ | Highly luminescent 0D Cs$_4$PbBr$_6$ nanocrystals into a 3D CsPbBr$_3$ film | EQE = 8.3%; luminance = 11,200 cd·m$^{-2}$ | [202] |
| | 2023 | ITO/ZnO-PEIE/Cs$_4$PbI$_6$/FA$_x$Cs$_{1-x}$PbI$_3$/TFB/MoO$_x$/Au | Cs$_4$PbI$_6$ | The formation of a heterostructure consisting of 0D Cs$_4$PbI$_6$ and 3D FA$_x$Cs$_{1-x}$PbI$_3$ | Photon flux = 1.75 × 10$^{21}$ m$^{-2}$·s$^{-1}$; EQE = 21.0% | [137] |
| | 2021 | ITO/PEDOT:PSS/Cs$_{4-x}$K$_x$PbBr$_6$/CsPbBr$_3$/MoO$_3$/Ag | KBr | Introducing potassium bromide (KBr), prepare 0D/3D Cs$_{4-x}$K$_x$PbBr$_6$/CsPbBr$_3$ heterostructure perovskite films | EQE = 12.8%; luminance = 39,400 cd·m$^{-2}$ | [136] |
| | 2018 | — | — | Prepared Cs$_{4-x}$A$_x$Sn(Br$_{1-y}$I$_y$)$_6$ (A = Rb, K) materials using a simple solid-state heat-and-beat approach | EL = 540 nm; QY = 15% | [203] |
| 1D/3D hybrid dimensional structure | 2021 | ITO/SnO$_2$/DEAECPbI$_3$/(Cs$_{0.04}$FA$_{0.86}$MA$_{0.1}$)Pb(I$_{0.9}$Br$_{0.1}$)$_3$/PCBM/Ag | 2-Diethylaminoethy-lchloride hydrochloride (DEAECCl) | Employed DEAECCl to produce a new 1D perovskitoid, induce the formation of 1D@3D perovskite structure | PCE = 22.9% | [204] |
| | 2023 | FTO/c-TiO$_2$/ChPbI$_3$/CsPbI$_3$/PCBM/carbon | Choline halide (ChX) | ChI react with CsPbI$_3$ to form 1D ChPbI$_3$ and constructs 1D/3D heterostructure with 3D CsPbI$_3$ | PCE = 18.05% | [130] |
| | 2022 | ITO/SnO$_2$/FA$_{0.9}$Cs$_{0.1}$PbI$_3$/Spiro-OMeTAD/Au | N,N′-Dialkylbenzimidazolium iodide | N,N′-Dialkylbenzimidazolium iodide functionalized to convert the 3D FACs-perovskite films into 1D capping layer topped 1D/3D structure | PCE = 24.30% | [205] |
| | 2021 | ITO/PTAA/Cs$_{0.05}$FA$_{0.81}$MA$_{0.14}$PbI$_{2.55}$Br$_{0.45}$/C$_{60}$/BCP/Ag | Benzimidazole cation (Bn$^+$) | Bn$^+$ form a 1D BnPbI$_3$ perovskite spatially distributed in the 3D perovskite film | PCE = 21.17% | [44] |
| | 2020 | FTO/TiO$_2$/(FAMACs)$_{1-x}$HA$_x$/Spiro-OMeTAD/Au | Hydrazinium cation (HA$^+$: NH$_2$NH$_3$$^+$) | Hydrazinium cation is incorporated into FAPbI$_3$-based perovskite to obtain novel 1D/3D hybrid dimension structur | PCE = 21.20% | [106] |
| | 2022 | ITO/SnO$_2$/CsFAMAPbI$_3$/PbI$_2$(Phen)/Spiro-OMeTAD/Ag | 1,10-Phenanthroline (Phen) | Introduce 1,10-phenanthroline (Phen) to form a 1D PbI$_2$(Phen) adduct phase on the surface of a 3D perovskite film | PCE = 23.3% | [206] |
| | 2020 | FTO/TiO$_2$/PbI$_2$-BPy/Cs$_{0.09}$FA$_{0.58}$MA$_{0.33}$PbI$_{2.35}$Br$_{0.65}$/Spiro-OMeTAD/Au | PbI$_2$-bipyridine (BPy)(II) perovskite | *In situ* assembly of a 1D@3D perovskite promoted by a PbI$_2$-dimethyl sulfoxide complex | PCE = 21.18% | [126] |
| | 2022 | ITO/SnO$_2$/Me$_3$SPbI$_3$/3D perovskite/Spiro-OMeTAD/Au | Me$_3$SPbI$_3$ | Incorporating 1D Me$_3$SPbI$_3$ into lead halide 3D perovskite, lead to heterostructural 1D/3D perovskite | PCE = 22.06% | [207] |
| | 2021 | ITO/SnO$_2$/(TMIMPbI$_3$)$_x$:[(FAPbI$_3$)$_{0.85}$(MAPbBr$_3$)$_{0.15}$]$_{1-x}$/Spiro-OMeTAD/Au | 1D ferroelectric perovskite | Incorporation of 1D ferroelectric perovskite with 3D organic–inorganic hybrid perovskite (OIHP) | PCE = 22.7% | [208] |
| | 2020 | ITO/SnO$_2$/perovskite layer/Spiro-OMeTAD/Au | *In situ* cross-linking polymerizable propargylammonium (PA$^+$) | Introduce an *in situ* cross-linking polymerizable propargylammonium (PA$^+$) to the 3D perovskite film at surfaces and grain boundaries to form a 1D/3D perovskite heterostructure | PCE = 21.19% | [142] |
| 2D/3D hybrid dimensional structure | 2017 | FTO/c-TiO$_2$/Cs$_{0.05}$(FA$_{0.83}$MA$_{0.17}$)$_{0.95}$Pb(I$_{0.83}$Br$_{0.17}$)$_3$/PEA$_2$PbI$_4$/Spiro-OMeTAD/Au | 2D PEA$_2$PbI$_4$ capping layers | 2D-3D perovskite stacking-layered architecture by *in situ* growing 2D PEA$_2$PbI$_4$ capping layers on top of 3D perovskite film | PCE = 18.51% | [209] |
| | 2021 | FTO/c-TiO$_2$/m-TiO$_2$/(Cs$_{0.05}$FA$_{0.855}$MA$_{0.095}$PbI$_{2.7}$Br$_{0.3}$/BDAI$_2$/Spiro-OMeTAD/Au | 1,4-Butanediamine iodide (BDAI$_2$) | Constructed DJ phase 2D plates, which are selectively grown on 3D film without completely covering the underlying 3D film | PCE = 20.1% | [119] |
| | 2021 | FTO/SnO$_2$/(FAPbI$_3$)$_{0.95}$(MAPbBr$_3$)$_{0.05}$/(C$_4$H$_9$NH$_3$)$_2$PbI$_4$/Spiro-OMeTAD/Au | 2D (C$_4$H$_9$NH$_3$)$_2$PbI$_4$ | Grow a stable and highly crystalline 2D (C$_4$H$_9$NH$_3$)$_2$PbI$_4$ film on top of a 3D film using a solvent-free solid-phase in-plane growth | PCE = 24.35% | [121] |
| | 2018 | ITO/SnO$_2$/c-SnO$_2$/FAPbI$_3$/PEA$_2$PbI$_4$/Spiro-MeOTAD/Ag | 2D PEA$_2$PbI$_4$ | 2D perovskite spontaneously forms at grain boundaries to protect the FA perovskite | PCE = 20.64% | [109] |
| | 2020 | ITO/SnO$_2$/ZnO/FA$_{0.95}$Cs$_{0.05}$PbI$_3$/Spiro-OMeTAD/Ag | β-guanidinopropionic acid (β-GUA) molecules | Incorporation of β-GUA into perovskite, facilitates the formation of quasi-2D structure with face-on orientation | PCE = 22.2% | [114] |
| | 2020 | FTO/TiO$_2$/CsPbI$_3$/PEA$_2$PbI$_4$/Spiro-OMeTAD/MoO$_3$/Ag | 2D PEA$_2$PbI$_4$ | Using an ultra-thin 2D perovskite to terminate CsPbI$_3$ GBs without damaging the original 3D perovskite | PCE = 18.82% | [115] |
| | 2021 | ITO/PEDOT:PSS/FASnI$_3$/ICBA/BCP/Al | FPEABr | Modulate the microstructure of 2D/3D heterogeneous tin-perovskite absorber films by substituting FAI with FPEABr in FASnI$_3$ | PCE = 14.03% | [116] |

(Continued)

| | Year | Device structure | Materials | Strategic and approach | Results | References |
|---|---|---|---|---|---|---|
| 2D/3D hybrid dimensional structure | 2019 | FTO/c-TiO$_2$/m-TiO$_2$/MAPbI$_3$/(Eu-pyP)$_{0.5}$MA$_{n-1}$Pb$_n$I$_{3n+1}$/Spiro-OMeTAD/Au | Eu-porphyrin complex (Eu-pyP) | Eu-porphyrin complex (Eu-pyP) is directly doped into methylammonium lead triiodide (MAPbI$_3$) precursor | PCE = 18.2% | [117] |
| | 2018 | FTO/c-TiO$_2$/m-TiO$_2$/MAPbI$_3$/Co porphyrins/Au | Tetra-ammonium zinc phthalocyanine (ZnPc) | Tetra-ammonium zinc phthalocyanine (ZnPc) was used to post-treat the MAPbI$_3$ film | PCE = 20.3% | [210] |
| | 2021 | ITO/2PACz/(PEA)$_2$(Cs$_{1-x}$FA$_x$)$_{n-1}$Pb$_n$(I$_{1-y}$Cl$_y$)$_{3n+1}$/C$_{60}$/BCP/Ag | Long chain alkylammonium salt phenethylammonium chloride (PEACl) | Using PEACl both as an additive and for surface treatment to simultaneously passivate the grain boundaries and the perovskite/C$_{60}$ interface | PCE = 22.7% | [122] |
| | 2021 | ITO/SnO$_2$/2-PyEAI@FAPbI$_3$/Spiro-OMeTAD/Au | 2-PyEA | Introducing 2-PyEA molecules with 2D structure and N atoms with a lone electron pair into perovskite | PCE = 23.2% | [123] |

(Fig. 12(a)). The generation of perovskite surface states causes surface lattice distortions, resulting in partial energy disorder of the surface layer. The width of the Urbach tail, related to the nature of the perovskite surface, reveals the level of disorder in the material. Energy disorder may be caused by factors such as the precursor solution stoichiometric ratio, surface defects, and the addition of LD perovskite [148]. Peng et al. combined 1-bromo-4-(methylsulfinyl)benzene (BBMS) with SnF$_2$, which reduced the Urbach energy of the perovskite films and inhibited the oxidation of Sn$^{2+}$ [149]. PDS measurements of the $E_U$ on the perovskite films revealed that the addition of BBMS decreased the $E_U$ from 28 to 19 meV (Figs. 12(b) and 12(c)). This implied that the Urbach energy of the perovskite films can be controlled through the formulation of the perovskite precursor solution. A larger energy disorder at the interface between the perovskite and the transport layer hinders charge carrier diffusion and intensifies non-radiative recombination. Hooman et al. showed an integrated relationship between Urbach energy and the charge carrier diffusion length (Fig. 12(d)) [150]. An increase in non-radiative recombination on the perovskite surface due to an increase in Urbach energy resulted in a shortened diffusion length of the charged carriers. PCBM has been widely investigated as a standard ETL for PSCs. According to the PDS, under identical circumstances, the Urbach tail connected to perovskite trap states at the PCBM/perovskite interface had a steeper slope and less Urbach energy than TiO$_2$ (Fig. 12(e)) [151]. However, the limited solubility of PCBM in the appropriate solvent results in the formation of energetically disorganized and inadequately covered layers on the perovskite surface, leading to energy loss [152]. The Urbach tail of the PCBM layer stretched into the forbidding band as a result of energy disorder, creating additional transition sites (Fig. 12(f)) [152]. The migration of non-equilibrium photogenerated carriers due to the additional transition site generation reduced the quasi-Fermi energy level of the electron. Compared with the control, the improved PCBM had a smaller energy disorder and a higher quasi-Fermi energy level. Although the energy disorder of the PCBM had improved, the Urbach tail was still substantial and continued to interfere with the functionality of the PSCs. Careful selection of the ETL is crucial to reduce the energy disorder at the interface between the ETL and the perovskite layer in order to achieve a higher $V_{oc}$. Jiang et al. employed the fullerene dimer (FP-C8) as an ETL instead of the PCBM because it showed molecular ordering and more extensive covering with the perovskite surface, resulting in less energy disorder and more stable films than PCBM [145]. On the perovskite surface, FP-C8 was visible clinging to the ions (Fig. 12(g)). The dense cover layer and more uniform surface distribution were made possible by this interfacial fixing effect. A more ordered energy was displayed by FP-C8 in comparison to

PCBM, which reduced the production of superfluous transition sites and reduced $V_{oc}$ loss (Fig. 12(h)). As a result, the design of the transport layer in PSCs can reduce energy disorder and improve the quality of the interface between the perovskite and transport layer, thereby minimizing the Urbach energy caused by changes in perovskite surface state. In addition to ETL, the interaction between HTL and perovskite is also important but has received little attention. Therefore, more accurate methods for detecting the Urbach tail and a deeper theoretical understanding of Urbach energy are urgently needed to effectively address the problem of energy disorder in perovskite layers.

### 3.3.2 Heterojunction construction based on energy level matching

To achieve high performance and stability in PSCs, proper alignment between the perovskite and transport layers is crucial. However, the splitting of the Fermi level in the perovskite layer has a significant impact on the $V_{oc}$ of PSCs [153]. Defects on the surface of perovskite and the misaligned energy levels can affect this splitting, leading to lower $V_{oc}$ and efficiency. The architecture of the heterojunction facilitates the alignment of energy levels and the movement of carriers between the transport and perovskite layers. Therefore, optimizing the contact between heterojunction interfaces can improve the transport layer for better results.

The quality of the perovskite film, as well as electron extraction and transport in formal devices, are significantly influenced by the ETL at the bottom of the perovskite film. In most PSCs, oxides are used as the ETL, carrying electrons and blocking holes [154]. TiO$_2$ is a preferred ETL material in PSCs due to its strong optoelectronic characteristics [155]. However, TiO$_2$ suffers from poor efficiency, surface imperfections, and low electron mobility, resulting in substantial current density–voltage (*J–V*) hysteresis [156, 157]. To address this, Liu et al. created a unique low-defect-density ETL by surface-modifying TiO$_2$ films with small-molecule ITIC [146]. This modification improved the energy level alignment by lowering the work function from −4.01 to −3.83 eV. The improved energy level alignment not only encouraged more efficient electron collection and transport, but also effectively hindered electron migration from the ETL to the perovskite absorber. Besides, SnO$_2$ is an ideal ETL candidate to replace TiO$_2$ due to its higher chemical stability, increased electron mobility, and suitable energy band structure [158]. Liu et al. used SnO$_2$ instead of TiO$_2$ as ETL, leading to improved electron mobility and a high $V_{oc}$ by employing EDTA to create a compound with SnO$_2$ that had an improved Fermi level aligned with the conduction band of the perovskite (Fig. 13(c)) [159]. Li et al. introduced ammonium chloride (NH$_4$Cl) into SnO$_2$ aqueous colloidal dispersions, which increased electron mobility and energy band alignment, and dramatically decreased *J–V* hysteresis [160]. ZnO is another excellent ETL option for PSCs due to its outstanding
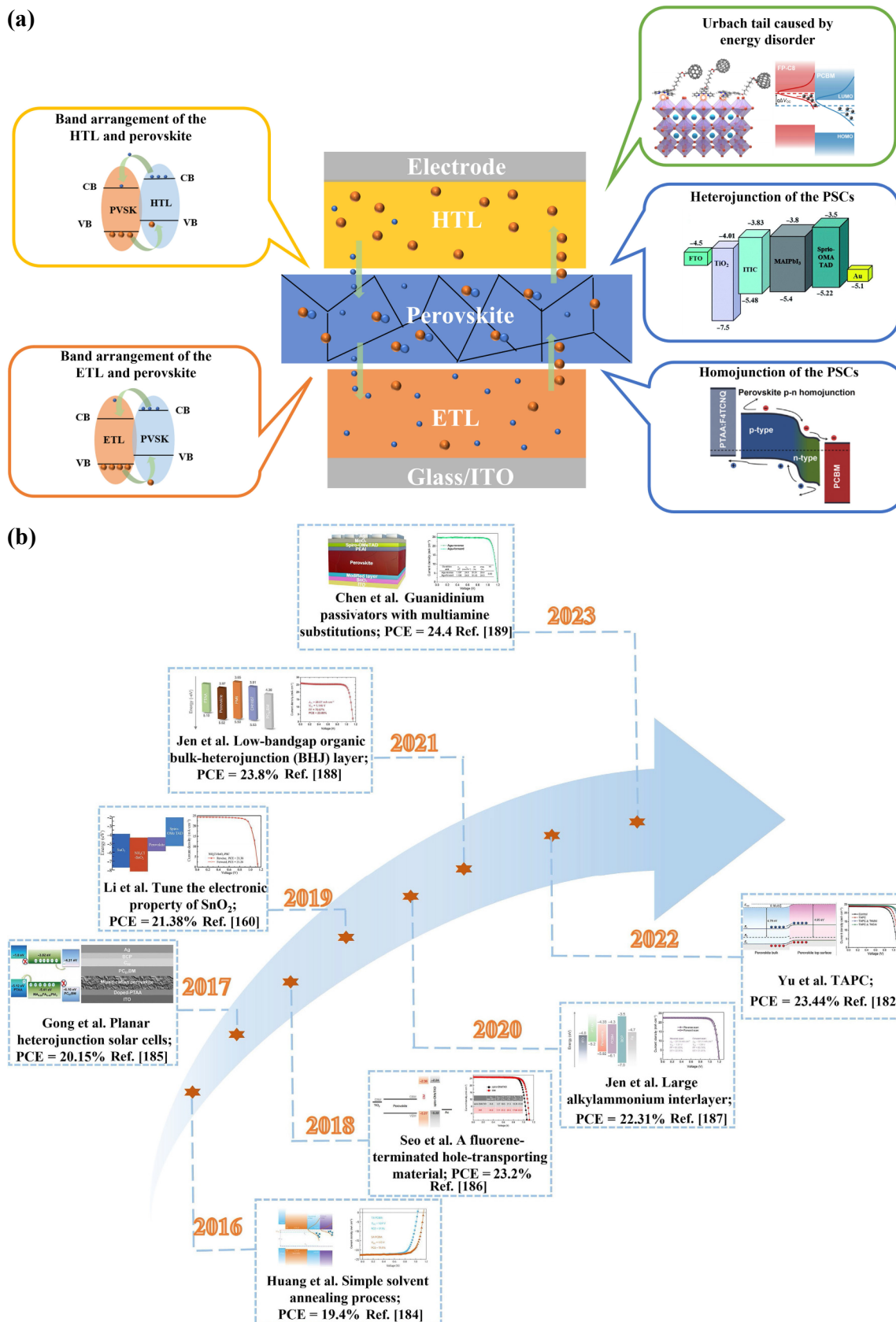
**(a)**



**(b)**



**Figure 11** (a) Modulation of the energy of the perovskite surface and interface. Energy band structure distribution of perovskite and HTL. Energy band structure distribution of perovskite and ETL. Loss of band-tailed states due to energy disorder. Heterojunction based on energy level matching of PSCs. Homojunction based on internal field modulation of PSCs. Reproduced with permission from Ref. [145], © American Chemical Society 2022. Reproduced with permission from Ref. [146], © The Royal Society of Chemistry 2017. Reproduced with permission from Ref. [147], © Elsevier Inc. 2020. (b) The graphical abstract of related breakthrough works with reported maximum PCE for each year. Reproduced with permission from Ref. [160], © Wiley-VCH Verlag GmbH & Co. KGaA, Weinheim 2019. Reproduced with permission from Ref. [182], © Wiley-VCH GmbH 2022. Reproduced with permission from Ref. [184], © Macmillan Publishers Limited 2016. Reproduced with permission from Ref. [184], © WILEY-VCH Verlag GmbH & Co. KGaA, Weinheim 2017. Reproduced with permission from Ref. [185], © Jeon, N. J. et al. 2018. Reproduced with permission from Ref. [186], © Elsevier Inc. 2020. Reproduced with permission from Ref. [187], © Wiley-VCH GmbH 2021. Reproduced with permission from Ref. [188], © American Chemical Society 2023.
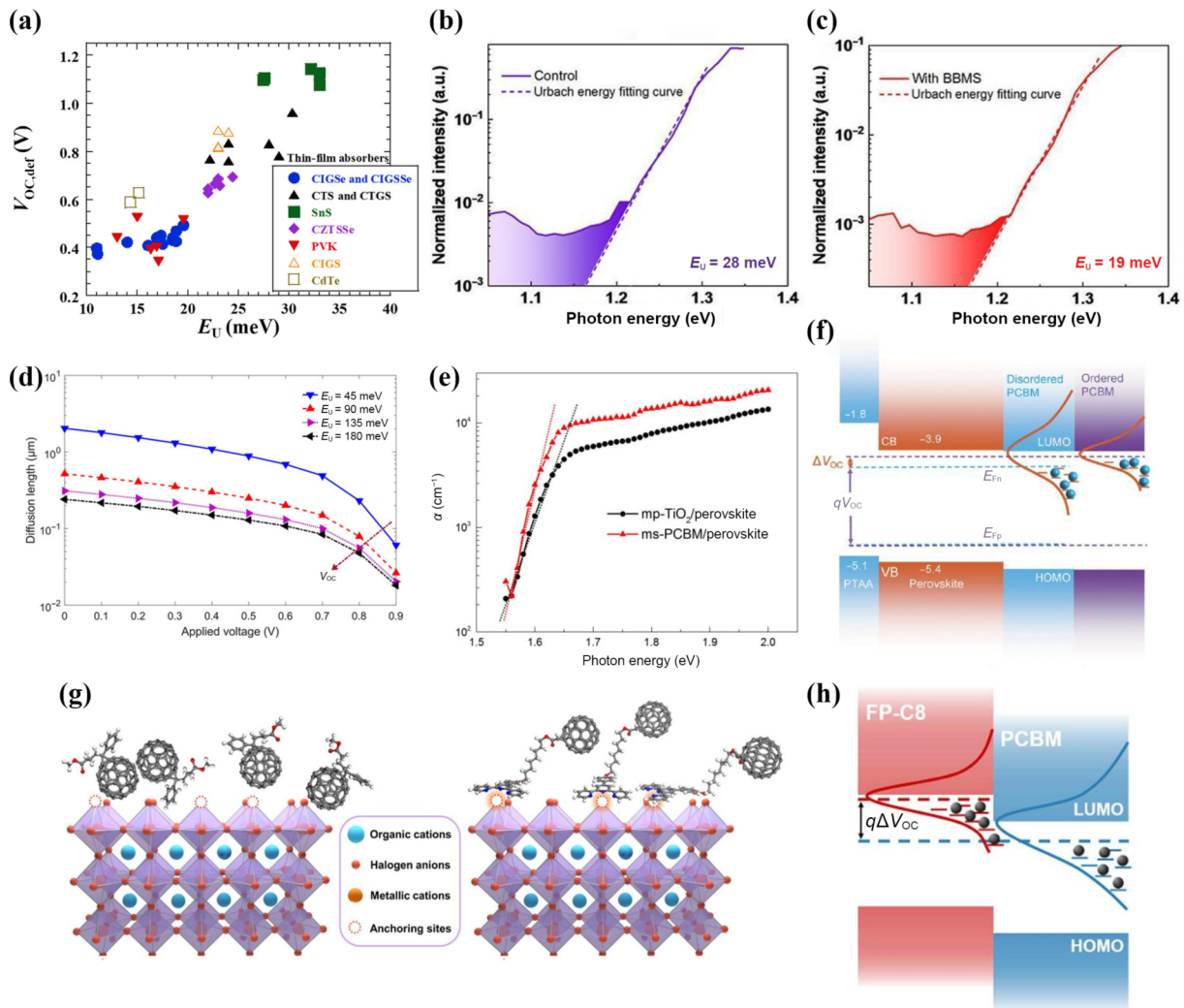
**Figure 12** (a) $V_{oc,def}$ as a function of the $E_U$ values of the thin-film absorbers of different-type thin-film solar cells, which are CIGSe, CIGSSe, CTS, CTGS, SnS, CZTSSe, PVK, CIGS, and CdTe thin-film solar cells. Reproduced with permission from Ref. [51], © Elsevier B.V. 2020. PDS spectra of perovskite films (b) without and (c) with BBMS prepared on quartz substrates. Reproduced with permission from Ref. [149], © Wiley-VCH GmbH 2022. (d) Diffusion length plotted as a function of the applied voltage in the active layer of a PSC of the structure Glass/PEDOT: PSS/CH$_3$NH$_3$PbI$_3$ (200 nm)/PC60BM/Al for four different Urbach energies. Reproduced with permission from Ref. [150], © Wiley-VCH Verlag GmbH & Co. KGaA, Weinheim 2019. (e) PDS measurements of perovskite films grown on mp-TiO$_2$ and ms-PCBM. Lines are linear fits to ln$\alpha$ according to the Urbach equation in sub-band gap region of absorption. Reproduced with permission from Ref. [151], © American Chemical Society 2016. (f) Schematic illustration of how energy disorder of the PCBM layer influences the device $V_{oc}$. Reproduced with permission from Ref. [152], © WILEY-VCH Verlag GmbH & Co. KGaA, Weinheim 2018. (g) Schematic illustration of the interfacial interactions between the perovskite and PCBM (left) or FP-C8 (right). Reproduced with permission from Ref. [145], © American Chemical Society 2022. (h) Schematic illustration of the relationship between energy level, energy disorder, and $\Delta V_{oc}$. (blue and red dashed lines represent the quasi-Fermi level of PCBM and FPC8, respectively). Reproduced with permission from Ref. [145], © American Chemical Society 2022.

optoelectronic characteristics and optimal energy level arrangement [161]. Hao et al. demonstrated that a ZnO/CsPbI$_2$Br heterojunction was successfully manufactured under a low-temperature technique below 150 °C [162]. Compared to SnO$_2$-based PSCs, the ZnO/perovskite expressed better energy level alignment, thus leading to higher electron extraction capability and excellent interfacial recombination suppression (Fig. 13(d)). In addition to oxides, PCBM is commonly used in inverted devices to passivate and smooth the surface defects of the perovskite, enhancing the separation of electrons and holes [163]. However, PCBM performs much worse than other ETLs due to poor film formation and low electron mobility. To optimize the PCBM, researchers have added dopants with excellent film formation and conductivity for regulation. Previously, some teams used polymers such as polystyrene (PS), polymethyl methacrylate (PMMA), and Triton X-100 as the PCBM additives to modify the surface of the PCBM layer [164–166]. Xia et al. added semiconducting poly(9,9-dioctylfluorene) (PFO) and poly(9,9-dioctylfluorene-cobalt benzothiazole) (F8BT) with excellent film-

forming properties to PCBM [167]. The results showed that the addition of 5% and 10% F8BT improved the homogeneity of pure PCBM, promoted the energy level matching between perovskite and PCBM, and facilitated the separation of electron–hole pairs.

The HTL is an essential part of PSCs because it dramatically reduces interfacial recombination and promotes charge extraction. Nickel oxide (NiO$_x$) is a commonly used HTL in PSCs. The traditional low-temperature solution procedure to create NiO$_x$ films results in a redox reaction with the perovskite film, and NiO$_x$ has a low electrical conductivity, resulting in poor contact between perovskite [168–171]. To address this, Hao et al. improved the HTL and perovskite heterojunction contact (NiO$_x$/perovskite) in the p-i-n structure device by including a CsBr buffer layer (Fig. 13(a)) [172]. The addition of a CsBr buffer layer to the NiO$_x$/MAPbI$_3$ interface increased the transfer of electrons to the surface of the perovskite from 0.66e to 0.89e, enhancing the short-circuit current density ($J_{sc}$) of the PSCs. Liu et al. created a bilayer and graded band-aligned inorganic HTM by introducing an ultrathin NiO$_x$ layer between FTO and perovskite and depositing
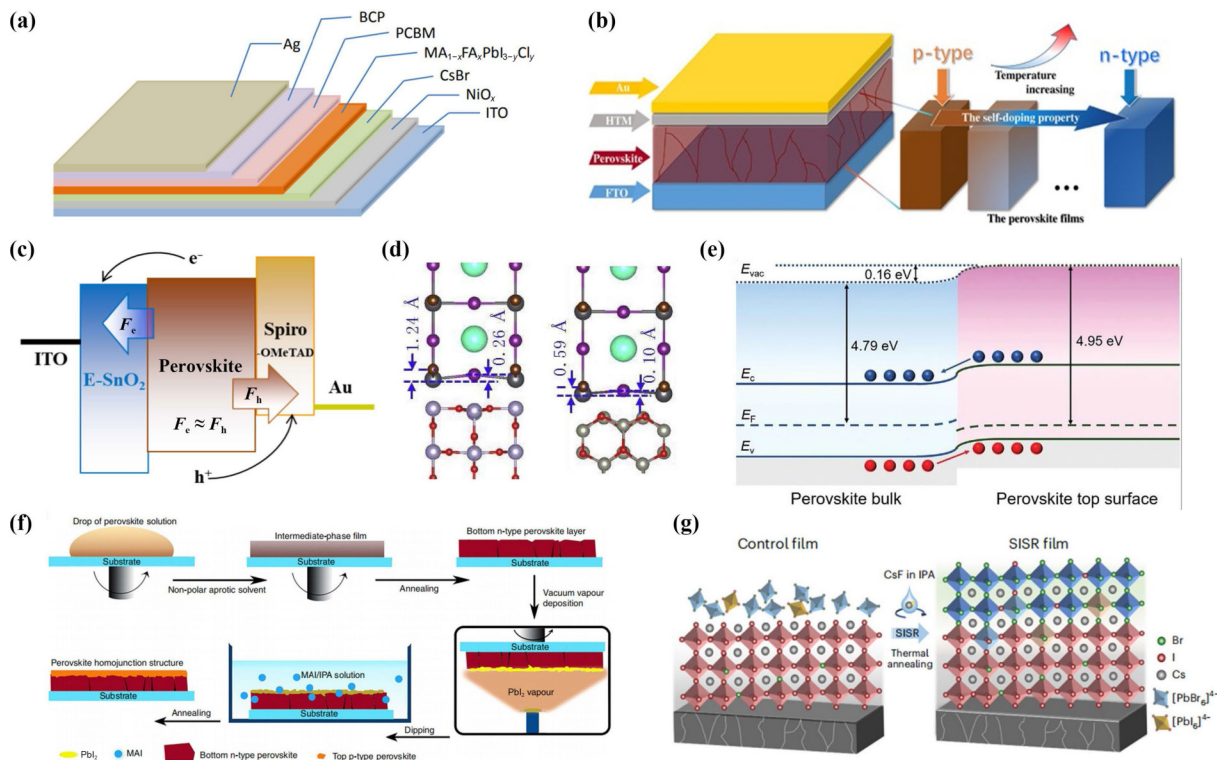
**Figure 13** (a) The device architecture of the inverted planar PSCs. Reproduced with permission from Ref. [172], © Zhang, B. J. et al. 2020. (b) Device architecture of the perovskite solar cells without electron-selective layer and schematic illustration of the change in self-doping property of the perovskite film. Reproduced with permission from Ref. [180], © WILEY-VCH Verlag GmbH & Co. KGaA, Weinheim 2017. (c) Charge transport mechanism of E-SnO₂ ETLs. Reproduced with permission from Ref. [159], © Yang, D. et al. 2018. (d) Optimized structures of CsPbI₂Br on the ZnO and SnO₂ surfaces, the marked arrows reflected the degree of octahedral distortion. Reproduced with permission from Ref. [162], © Elsevier Ltd. 2019. (e) The schematic illustration of the carriers' transportation on the top surface of FAPbI₃-TAPC film. Reproduced with permission from Ref. [182], © Wiley-VCH GmbH 2022. (f) The bottom n-type perovskite layer is deposited by a one-step spin-coating method. The top p-type perovskite layer is deposited by vacuum vapour deposition followed by a dipping process. Reproduced with permission from Ref. [181], © Cui, P. et al. 2019. (g) Schematic illustration of the graded heterojunctions via SISR, where CsF in IPA represent that CsF is dissolved in isopropanol. Reproduced with permission from Ref. [183], © Chu, X. B. et al. 2023.

mesoporous CuGaO₂ on this layer [173]. The addition of CuGaO₂ aligned the HTL and the VBM configuration of the perovskite, and the gradient energy configuration of the VBM between NiOₓ, CuGaO₂, and perovskite was beneficial for the transfer and collecting of charge carriers. In addition to using NiOₓ as HTL and optimizing it, PEDOT:PSS, PTAA, and P3CT are surface treatments for HTL that would encourage the interface contact between HTL and perovskite and enhance the interfacial alignment between energy levels [174–177].

Overall, the careful selection of the appropriate transport layer and the optimization of the interface can have a profound impact on the heterostructure with perovskite, resulting in improved contact between the perovskite layer and the transport layer. This, in turn, enhances the extraction and transfer of charges, ultimately leading to a more stable and efficient performance of the device. By fine-tuning the energy level alignment and addressing surface defects, PSCs can achieve enhanced stability and better overall performance, making them more suitable for practical applications.

### 3.3.3 Homojunction design based on built-in electric field modulation

The short diffusion length of carriers in perovskite can lead to weak carrier separation and slow transport, leading to non-radiative recombination at the perovskite surface and interface [178, 179]. To address this, the concept of perovskite homojunction has been introduced, creating an additional built-in electric field to enhance photogenerated electron and hole transport. This will further reduce carrier recombination in PSCs. Li et al. proposed a method to eliminate the ETL structure in PSCs

by gradually transforming the perovskite layer to n-type perovskite by changing the annealing temperature (Fig. 13(b)) [180]. The manipulation resulted in a self-doping of perovskite films, creating p-n homojunction and providing built-in electric fields. This design significantly improved carrier selection and transport in the perovskite layer, leading to a PCE of 15.69% in ETL-free devices. In planar p-i-n junction PSCs, photogenerated carriers lack a preferred orientation, allowing non-radiative recombination at the perovskite/transport layer interface. Li et al. manufactured the first planar p-n homojunction PSCs, where a built-in electric field was created in a p-type perovskite/n-type perovskite homojunction fabricated by a combined deposition method (Fig. 13(f)) [181]. The generation of the homojunction reduced the nonradiative recombination losses, with a final efficiency of up to 21.38%. Bao et al. achieved the transition from p-type to n-type perovskite by passivating charged defects of the perovskite surface by adding the natural additive capsaicin [147]. The formation of homojunction facilitates charge dissociation/transport as the n-type section of the perovskite combines with the p-type region, which is closely aligned with the ETL. The built-in electric field in the perovskite film enables the separation of photogenerated carriers before they reach the perovskite/transport layer interface, leading to an efficiency of 21.88% and an FF of 83.81%. In addition to the p-n homojunction, Yu et al. treated the surface of the perovskite films by dissolving 4,4′-cyclohexylidenebis [N,N-bis(4-methylphenyl) benzene amine] (TAPC) in an antisolvent to develop a p/p homojunction [182]. The induction of p-type doping by TAPC resulted in a bending of the energy band on the perovskite film surface, facilitating the movement of electrons from the surface to the interior while holes moved oppositely. This created an internal

electric field extending from the interior of the perovskite film toward the surface (Fig. 13(e)). The PCE of the $FAPbI_3$ perovskite was increased to 23.44% due to the p/p homojunction, effectively reducing non-radiative recombination loss and $V_{oc}$ loss at the perovskite/HTL interface. The interface between the inorganic perovskite with a wide band gap and CTL experiences a significant energy shift, resulting in harmful interfacial charge recombination detrimental to the accumulation of photogenerated carriers. To address this, You et al. developed a strategy for *in situ* reconstruction (SISR) of inorganic perovskite surfaces using CsF on perovskite surfaces (Fig. 13(g)) [183]. They confirmed that the excess $PbX_2$ on the perovskite surface interacted with CsF through solid-state reactions to form a wider bandgap inorganic perovskite layer as a graded homogeneous junction. The graded homojunction generates a built-in electric field that promotes holes and blocks electrons from transporting to the HTL, resulting in all-inorganic PSCs with an efficiency of 21.02%.

The concept of homojunction has become a hot research topic in recent years, as it promises to prepare more efficient and stable perovskite devices, laying the foundation for the preparation of large-area PSCs and flexible devices. The main innovative advances in energy modulation at the perovskite surface and interface are summarized in Table 3 and complemented with a graphical summary of PCE breakthroughs each year (Fig. 11(b)) [47, 160, 182, 184–188].

# 4   Conclusions and outlook

In conclusion, our comprehensive review provides conceptual insights into understanding the fundamental physical and chemical properties of perovskite surface-interface. We have critically examined the current scientific and technological efforts aimed at optimizing optoelectronic performance and structural stability, with a particular focus on defects, dimensions, and energies. Despite significant progress in addressing challenges related to energy deficit and intrinsic structural decomposition on the exposed surface, we acknowledge that we are still in the early stages of understanding and overcoming these issues. Moving forward, we propose key considerations for the commercial application of PCSs (Fig. 14).

Firstly, there is a pressing demand for reliable and high-sensitivity probing techniques to unravel carrier dynamics at the surface-interface. Quantifying carrier transfer or defect-assisted recombination kinetics is essential for understanding the predominant sources of energy-loss theoretical mechanism and assessing the accuracy of surface reconstruction engineering. High time resolution and high spatial screening characterizations, such as transient absorption spectroscopy and scanning probe microscopy, should be further developed. For instance, Jin et al. recently reported *in situ* measurements of carrier transport in $CH_3NH_3PbI_3$ perovskite microcrystals (MCs) at high pressure using space-time resolved fluorescence scanning imaging [189]. This technique allowed the observation of different phase transition phenomena at different pressures, demonstrating that perovskite could maintain good carrier transport properties under high pressures. Although not extensively applied to the perovskite system, such methods hold promise for understanding additional characteristics at the perovskite surface and interface. Additionally, theoretical simulations of carrier transport at the interface can further complement our understanding. In addition, *in situ* characterization techniques have become indispensable in the film-forming stage of the perovskite, among which *in situ* infrared, *in situ* Raman, *in situ* X-ray photoelectron spectroscopy (XPS), and *in situ* synchrotron radiation have been widely employed for perovskite film testing. For example, Gong et al. probed the evolution of electronic structures of perovskite surfaces by *in situ* XPS [190]. The *in situ* XPS analysis observed the evolution of N 1s XPS spectra of halogenated PEA organics as they were annealed at temperatures ranging from 30 to 100 °C. The results indicated that, following annealing at 100 °C, only ultrathin PEA organic ligands remained on the perovskite surface. Furthermore, the energy level alignment of the perovskite heterojunction interface was assessed through *in situ* ultraviolet photoelectron spectroscopy (UPS) analysis during the deposition of $PEA^+$ and $C_{60}$ onto perovskite films. The analysis served to illustrate the exceptional electron transport capabilities exhibited by the perovskite/PEA/$C_{60}$ system. These approaches greatly facilitate the understanding of carrier dynamics within perovskite materials as well as the intricate electronic and energy band structures at their interfaces. In addition, spectroscopic techniques such as *in situ* absorption and *in situ* fluorescence spectroscopy make it possible to probe the dynamic differences in surface energy, solvent concentration, and interfaces at different sites of film materials during solvent volatilization. *In situ* characterization tests not only enable a deeper exploration into the nucleation and crystallization mechanisms of perovskites but also make significant contribution to further advancement in designing various film deposition methodologies.

Secondly, considering the soft ionic nature of perovskite materials, rational material design engineering offers an avenue to eliminate chemical impurities and reinforce the stability of crystal texture. Low-dimensional perovskite, such as 1D and 2D structures, exhibit strikingly different physical and chemical properties compared to conventional 3D perovskite crystal structures. However, challenges arise due to spatial site resistance caused by large organic cations in 1D perovskite, leading to conductivity differences between devices and showing anisotropy. Similarly, wide bandgap 2D perovskite with long-chain organic cations may hinder charge extraction from 3D perovskite to neighboring charge transport layers, leading to lower PCE. The 2D perovskite exhibits excellent luminescence properties due to the higher exciton binding energies as a result of quantum confinement and dielectric-limited domain effects. Phenylammonium ($PEA^+$) and butylammonium ($BA^+$) are widely used in 3D perovskite to form 2D perovskite on the perovskite surfaces and at grain boundaries for solving the transport property of the 3D perovskite [141, 191]. However, these cations are unstable in FA-based perovskite at high temperatures as well as under light. Huang et al. addressed the deprotonation scenario by substituting $PEA^+$ and $BA^+$ with ammonium ions with high acid dissociation constants, thus further improving the stability of the perovskites [192]. Hence, it becomes crucial to consider the dielectric and deprotonated properties of the ligands to improve the stability of PSCs while enhancing PCE. Furthermore, 0D perovskite, with its strong quantum confinement effects, offers a potential solution to minimize defects in solid perovskite films through ligand engineering. However, careful control of the electronic coupling between the surface and the ligand is imperative. Besides, the development of single-crystal materials holds great promise, given their excellent carrier lifetime, light absorption area, and carrier diffusion length, making them highly advantageous for solar cells and photodetectors, etc. [193]. Additionally, the observations of the high electronic quality of macroscopic single crystals grown in solution demonstrate that further improvements to material quality are not constrained by the thermodynamics of defect formation in perovskite halides. Nevertheless, it is important to acknowledge that generally prepared single crystal perovskite films have high thicknesses exceeding the diffusion length of the carriers, resulting in low transmittance and causing ohmic loss, which ultimately affects the

**Table 3** Summary of innovative developments in homojunction and heterojunction construction in PSCs

| | Year | Device structure | Strategic and approach | Type | Results | References |
|---|---|---|---|---|---|---|
| Homojunction-based internal field modulation | 2021 | ETL/FAPbI$_3$:0.38MDACl$_2$/Spiro-OMeTAD/Au | The formation of a coherent interlayer between a perovskite thin film and a Cl-bonded SnO$_2$ electrode coated with a Cl-containing FAPbI$_3$ perovskite precursor solution | — | PCE = 25.8% | [211] |
| | 2019 | FTO/c-TiO$_2$/MAPbI$_3$/Spiro-OMeTAD/Au | Integrate the homojunction structure in a planar PSCs combining a thermally evaporated p-type perovskite layer on a solution-processed n-type perovskite layer | n/p | PCE = 20.8% | [181] |
| | 2021 | FTO/TiO$_2$/n-MAPbI$_3$/p-MAPbI$_3$/carbon | New design of n-CH$_3$NH$_3$PbI$_3$/p-CH$_3$NH$_3$PbI$_3$ homojunction is presented to attempt high effiffifficiency HTL-free C-PSCs | n/p | PCE = 25.07% | [212] |
| | 2017 | FTO/MAPbI$_3$/Spiro-MeOTAD/Au | Self-doping property of the perovskite is controlled by defects engineering; introducing mixed nonpolar aprotic solvents to obtain optimal balancing between densification and grain size | p/n | PCE = 15.69% | [180] |
| | 2015 | FTO/c-TiO$_2$/MAPbI$_3$/HTM/Au | Doping property of the perovskite varies from p-type, intrinsic to n-type with increasing annealing temperature | p/n | PCE = 17.5% | [213] |
| | 2021 | ITO/PTAA:F4TCNQ/MAPbI$_3$/PCBM/BCP/Ag | A complete transformation of perovskite MAPbI$_3$ surface region energetics from p- to n-type during defect passivation caused by natural additive capsaicin | p/n | PCE = 21.88% | [147] |
| | 2022 | ITO/SnO$_2$/ThMAI or ThEAI/FAPbI$_3$/TAPC/Spiro-MeOTAD/Ag | The 4,4′-cyclohexylidenebis [N,N-bis(4-methylphenyl) benzene amine] is dissolved into the antisolvent to prepare perovskite films | p/p+ | PCE = 23.44% | [182] |
| | 2022 | FTO/c-TiO$_2$/MAPbI$_3$/Spiro-MeOTAD/Ag | Improved electric fifield at the homojunction, have optimized the thickness range for n-type perovskite (700–800 nm) and p-type perovskite (300–400 nm) | n/p | PCE = 23.52% | [214] |
| Heterojunction-based energy level matching | 2017 | FTO/TiO$_2$/ITIC/MAPbI$_3$/Spiro-MeOTAD/Au | A novel low-trap-density ETL is developed by surface modifification of the an-TiO$_2$ fifilm using small-molecular ITIC | TiO$_2$/ITIC/MAPbI$_3$ | PCE = 20.08% | [146] |
| | 2018 | ITO/EATA/SnO$_2$/FA$_{0.95}$Cs$_{0.05}$PbI$_3$/Spiro-MeOTAD/Au | An EDTA-complexed SnO$_2$ ETL by complexing EDTA with SnO$_2$ | EDTA/SnO$_2$/FA$_{0.95}$Cs$_{0.05}$PbI$_3$ | PCE = 21.60% | [159] |
| | 2019 | ITO/NH$_4$Cl/SnO$_2$/MAPbI$_3$/Spiro-MeOTAD/Au | PSCs with ammonium chloride induced coagulated SnO$_2$ colloids | NH$_4$Cl/SnO$_2$/MAPbI$_3$ | PCE = 21.38% | [160] |
| | 2019 | ITO/ZnO-TiO$_x$/PCBM/MA$_{1-y}$FA$_y$PbI$_{3-x}$Cl$_x$/Spiro-OMeTAD/Ag | A low temperature TiO$_x$ treatment to passivate the ZnO surface | TiO$_x$/ZnO/PCBM/MA$_{1-y}$FA$_y$PbI$_{3-x}$Cl$_x$ | PCE = 20.7% | [161] |
| | 2020 | ITO/ZnO/CsPbI$_2$Br/Spiro-OMeTAD/Ag | The low temperature solution processed ZnO was successfully introduced into the all-inorganic PSCs to replace SnO$_2$ | ZnO/CsPbI$_2$Br | PCE = 14.78 | [162] |
| | 2019 | ITO/NiO$_x$/MAPbI$_3$/F8BT/PCBM/PFO/BCP/Ag | Improve the fifilm-forming properties of PCBM by doping PCBM with F8BT as the ETL | MAPbI$_3$/F8BT/PCBM/PFO | PCE = 15.26% | [167] |
| | 2016 | ITO/PEDOT:PSS/MAPbI$_3$/PCBM/PEI/Al | Doping a 3 wt.% of polyethylenimine (PEI) as additive into the PCBM electron transport layer of an inverted perovskite solar cell | MAPbI$_3$/PCBM/PEI | PCE = 10.7% | [165] |
| | 2017 | FTO/NiO$_x$/FA$_{0.83}$MA$_{0.17}$Pb(I$_{0.83}$Br$_{0.17}$)$_3$/Triton X-100/PCBM/Au | PCBM containing a surfactant Triton X-100 acts as the ETL and NiO$_x$ nanocrystals act as a HTL | FA$_{0.83}$MA$_{0.17}$Pb(I$_{0.83}$Br$_{0.17}$)$_3$/TritonX-100/PCBM | PCE = 15.68% | [166] |
| | 2018 | ITO/NiO$_x$/F6TCNNQ/MAPbI$_3$/PCBM/ZrAcac/Ag | A novel molecular doping of NiO$_x$ is realized successfully by 2,2′-(perfluoronaphthalene-2,6-diylidene)dimalononitrile (F6TCNNQ) | NiO$_x$/F6TCNNQ/MAPbI$_3$ | PCE = 19.75% | [170] |
| | 2022 | ITO/NiO$_x$-IL/Cs$_{0.05}$(MA$_{0.15}$FA$_{0.85}$)$_{0.95}$Pb(I$_{0.85}$Br$_{0.15}$)$_3$/PCBM + C$_{60}$/BCP/Cr/Au | Obtain high-quality NiO$_x$ nanoparticles via an ionic liquid-assisted synthesis method (NiO$_x$-IL) | NiO$_x$/[BMIm]BF$_4$/Cs$_{0.05}$(MA$_{0.15}$FA$_{0.85}$)$_{0.95}$Pb(I$_{0.85}$Br$_{0.15}$)$_3$ | PCE = 22.62% | [171] |
| | 2020 | ITO/NiO$_x$/CsBr/MA$_{1-x}$FA$_x$PbI$_{3-y}$Cl$_y$/PCBM/BCP/Ag | A CsBr buffer layer is inserted between NiO$_x$ hole transport layer and perovskite layer | NiO$_x$/CsBr/MA$_{1-x}$FA$_x$PbI$_{3-y}$Cl$_y$ | PCE = 19.7% | [172] |
| | 2020 | ITO/NiO$_x$/PTAA/(MAPbI$_3$)$_{0.95}$(MAPbBr$_2$Cl)$_{0.05}$/PCBMBCP/Ag | Interface engineering was carried out by modifying the NiO$_x$ layer with PTAA to improve the surface contact between NiO$_x$ and the perovskite | NiO$_x$/PTAA/(MAPbI$_3$)$_{0.95}$(MAPbBr$_2$Cl)$_{0.05}$ | PCE = 21.56% | [215] |
| | 2018 | FTO/c-NiO$_x$/mp-CuGaO$_2$/perovskite/PCBM/BCP/Ag | The new PSC has a graded band alignment and bilayered inorganic HTMs (i.e., compact NiO$_x$ and mesoporous CuGaO$_2$) | c-NiO$_x$/mp-CuGaO$_2$/perovskite | PCE = 20.13% | [173] |
| | 2022 | ITO/PMMA-PTAA/MAPbI$_3$/PCBM/BCP/Ag | Using a poly(methyl methacrylate) (PMMA):2,3,5,6-tetrafluoro-7,7,8,8-tetracyanoquinodimethane (F4-TCNQ)-modified poly(bis(4-phenyl)(2,4,6-trimethylphenyl)amine) (PTAA) | PMMA-PTAA/MAPbI$_3$ | PCE = 20.08% | [176] |
| | 2022 | ITO/P3CT-K(GDYO)/MAPbI$_3$/PCBM/ZnO/Al | Graphdiyne oxide (GDYO) doped P3CT-K nanocomposites are applied as the hole transport nanolayer | P3CT-K(GDYO)/MAPbI$_3$ | PCE = 19.06% | [177] |
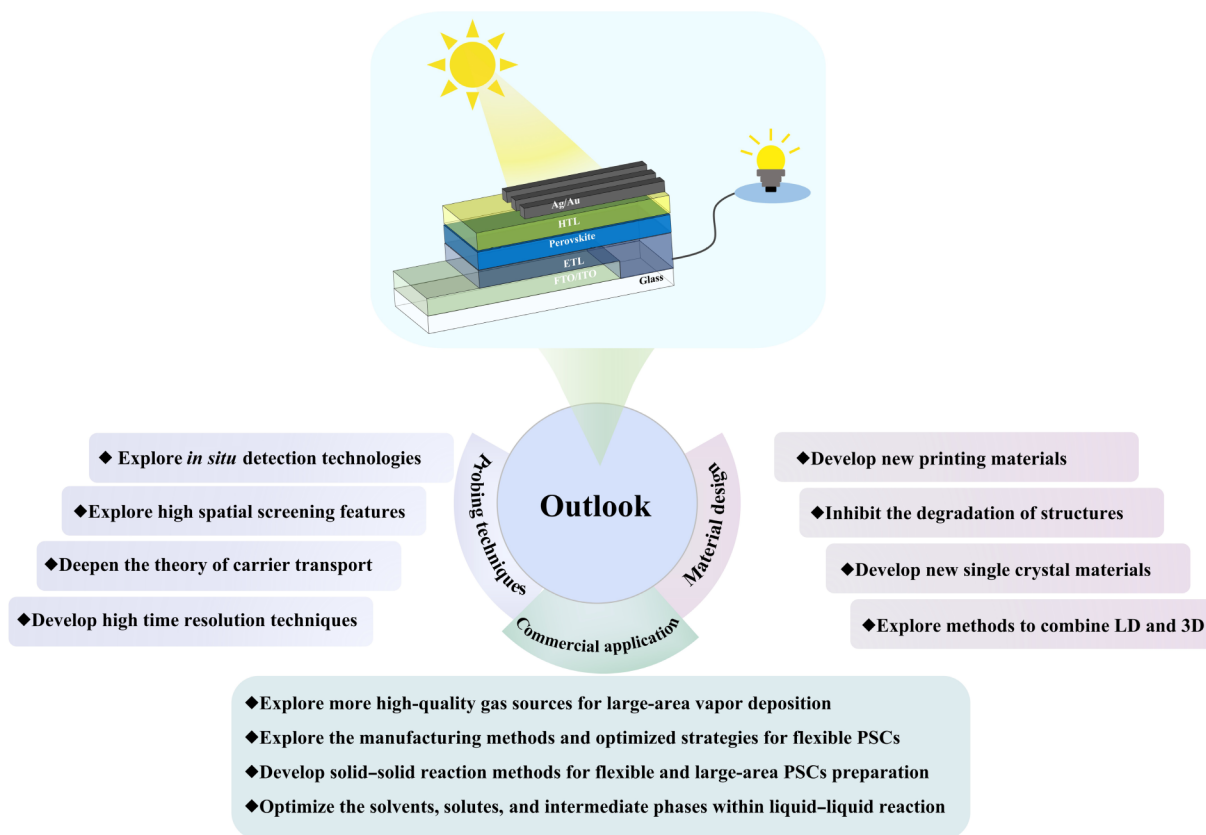
**Figure 14** A brief summary of the perspectives: probing technologies, material design, and commercial applications.

final efficiency of PSCs. As a result, the modulation of crystallinity or orientation of single crystals becomes necessary to prepare high-quality single crystal-like perovskite films [193].

Thirdly, the perovskite films are formed using a liquid–liquid reaction, which contains solvents, solutes, and intermediate phases in the formation of the film that affect the crystallization properties of the perovskite. Therefore, it is imperative to focus on exploring chemical process induced by solutes and solvents. Varying solvent compositions or precursor reaction rates can influence nucleation/growth rates, thereby impacting the microscopic morphology of perovskite crystals. Song et al. successfully impeded rapid ion reactions in the precursor by substituting $PbX_2$ with a $PbX_2$-DMSO complex and prolonged the retention time of the liquid film by introducing n-methyl pyrrolidone (NMP), effectively modulating solvent viscosity and surface energy [194]. This approach slowed down the nucleation/growth rate of the perovskite films, resulting in the formation of well-formed perovskite surfaces. This approach also effectively decelerated the nucleation/growth rate of the perovskite films, leading to the formation of well-defined perovskite surfaces. Moreover, during the preparation of perovskite films using the two-step method, intermediate phases inevitably emerge, which potentially exert a detrimental influence on both nucleation and crystallization processes. Hence, a more profound comprehension and modification of the conventional liquid–liquid reaction are imperative. The spin-coating method utilizes centrifugal force to create perovskite films, employing high-boiling-point polar aprotic solvents in the coating solution. However, the use of polar aprotic solvents in spin-coating is beneficial for the formation of large area film exceeding $10 \times 10$ cm$^2$ [195]. Therefore, there is a pressing need to develop alternative methods that can be applied to high throughput or large area aspects, such as vapor deposition methods. Song et al. used $CS_2$ vapor to treat perovskite surface defects, a method that circumvents the disadvantages of film inhomogeneity caused by spin-coating-assisted passivation and

reconstruction of perovskite surface using solvents [196]. Furthermore, Zhao et al. proposed a solvent-free solid-phase passivation (SPP) technique, where they pre-prepared a passivator film and vertically covered the upper surface of the prepared perovskite film under hot pressing conditions [197]. This solid–solid reaction forms a chemical bond between the passivated molecule and the incompatible $Pb^{2+}$ ions through ligand bonding. Additionally, it enables the use of a passivation device to remove surface residues after the solid–solid reaction. These techniques hold promise for commercial application since they not only enhance efficiency, but can also be employed across various fields involving PSCs. In addition, the flexible PSCs for portable and wearable electronic devices are important for the commercialization of the perovskites. However, the surface-interface properties of the perovskite are a fundamental cause of device degradation during bendable usage. The perovskite is susceptible to fracturing since its grain boundaries are readily broken after numerous bending cycles [198]. Therefore, Ge et al. synthesized –CN additives with different molecular dipoles, where F$^-$ formed hydrogen bound with charged FA$^+$ groups and modulated the dipole moments of the additives, therefore ameliorating defects on the perovskite grain boundaries and releasing tensile stresses at the grain boundaries [199]. In addition, they found that by modifying the additives, the Ym of the perovskite films was significantly reduced and the mechanical flexibility was improved. This additive-modified unpacked f-PSCs showed favorable light, heat, and air stability. Furthermore, laser polishing can be applied to the preparation of flexible PSCs to prevent structural damage caused by bending of flexible PSCs during usage, which helps to promote the commercialization of PSCs [200]. Therefore, rather than solely focusing on conventional body mass doping and surface treatment, it is imperative to actively explore novel approaches for the fabrication of mechanically robust and flexible devices with exceptional durability.

Overall, it is a systematic and meaningful endeavor to comprehend the various pathways of energy loss and the degradation mechanisms at the surface-interface, while simultaneously optimizing the regulation strategies and device characteristics for surface and interface engineering. Through strategies such as surface state reconstruction and energy level alignment optimization between transport and perovskite layers, it is expected that the experimental data for single-junction PSCs will surpass 30%, propelling perovskite solar cells closer to commercial viability.

## Acknowledgements

## References

[1] Zuo, C. T.; Bolink, H. J.; Han, H. W.; Huang, J. S.; Cahen, D.; Ding, L. M. Advances in perovskite solar cells. *Adv. Sci.* **2016**, *3*, 1500324.

[2] Dong, Q. F.; Fang, Y. J.; Shao, Y. C.; Mulligan, P.; Qiu, J.; Cao, L.; Huang, J. S. Electron–hole diffusion lengths > 175 μm in solution-grown CH$_3$NH$_3$PbI$_3$ single crystals. *Science* **2015**, *347*, 967–970.

[3] Xing, G. C.; Mathews, N.; Sun, S. Y.; Lim, S. S.; Lam, Y. M.; Gräetzel, M.; Mhaisalkar, S.; Sum, T. C. Long-range balanced electron- and hole-transport lengths in organic-inorganic CH$_3$NH$_3$PbI$_3$. *Science* **2013**, *342*, 344–347.

[4] Stranks, S. D.; Eperon, G. E.; Grancini, G.; Menelaou, C.; Alcocer, M. J. P.; Leijtens, T.; Herz, L. M.; Petrozza, A.; Snaith, H. J. Electron–hole diffusion lengths exceeding 1 micrometer in an organometal trihalide perovskite absorber. *Science* **2013**, *342*, 341–344.

[5] Zhong, Y.; Liu, G. L.; Su, Y.; Sheng, W. P.; Gong, L. Y.; Zhang, J. Q.; Tan, L. C.; Chen, Y. W. Diammonium molecular configuration-induced regulation of crystal orientation and carrier dynamics for highly efficient and stable 2D/3D perovskite solar cells. *Angew. Chem., Int. Ed.* **2022**, *61*, e202114588.

[6] Kojima, A.; Teshima, K.; Shirai, Y.; Miyasaka, T. Organometal halide perovskites as visible-light sensitizers for photovoltaic cells. *J. Am. Chem. Soc.* **2009**, *131*, 6050–6051.

[7] Bai, S.; Da, P. M.; Li, C.; Wang, Z. P.; Yuan, Z. C.; Fu, F.; Kawecki, M.; Liu, X. J.; Sakai, N.; Wang, J. T. W. et al. Planar perovskite solar cells with long-term stability using ionic liquid additives. *Nature* **2019**, *571*, 245–250.

[8] Prasanna, J. L.; Goel, E.; Kumar, A.; Kumar, A. Computational study of perovskite/perovskite lead-free tandem solar cell devices. In *Proceedings of 2022 IEEE International Symposium on Smart Electronic Systems*, Warangal, India, 2022, pp 257–262.

[9] chart., N. e. [Online]. https://www.nrel.gov/pv/assets/pdfs/best-research-cell-efficiencies.pdf, (accessed Jun 2023).

[10] Xie, H. B.; Lira-Cantu, M. Multi-component engineering to enable long-term operational stability of perovskite solar cells. *J. Phys. Energy* **2020**, *2*, 024008.

[11] Long, C. Y.; Huang, K. Q.; Chang, J. H.; Zuo, C. T.; Gao, Y. J.; Luo, X.; Liu, B.; Xie, H. P.; Chen, Z. H.; He, J. et al. Creating a dual-functional 2D perovskite layer at the interface to enhance the performance of flexible perovskite solar cells. *Small* **2021**, *17*, 2102368.

[12] Yao, K.; Wang, X. F.; Li, F.; Zhou, L. Mixed perovskite based on methyl-ammonium and polymeric-ammonium for stable and reproducible solar cells. *Chem. Commun.* **2015**, *51*, 15430–15433.

[13] Abdelmageed, G.; Jewell, L.; Hellier, K.; Seymour, L.; Luo, B. B.; Bridges, F.; Zhang, J. Z.; Carter, S. Mechanisms for light induced degradation in MAPbI$_3$ perovskite thin films and solar cells. *Appl. Phys. Lett.* **2016**, *109*, 233905.

[14] Shi, D.; Adinolfi, V.; Comin, R.; Yuan, M. J.; Alarousu, E.; Buin, A.; Chen, Y.; Hoogland, S.; Rothenberger, A.; Katsiev, K. et al. Low trap-state density and long carrier diffusion in organolead trihalide perovskite single crystals. *Science* **2015**, *347*, 519–522.

[15] Shao, Y. C.; Fang, Y. J.; Li, T.; Wang, Q.; Dong, Q. F.; Deng, Y. H.; Yuan, Y. B.; Wei, H. T.; Wang, M. Y.; Gruverman, A. et al. Grain boundary dominated ion migration in polycrystalline organic-inorganic halide perovskite films. *Energy Environ. Sci.* **2016**, *9*, 1752–1759.

[16] Tan, S.; Yavuz, I.; Weber, M. H.; Huang, T. Y.; Chen, C. H.; Wang, R.; Wang, H. C.; Ko, J. H.; Nuryyeva, S.; Xue, J. J. et al. Shallow iodine defects accelerate the degradation of α-phase formamidinium perovskite. *Joule* **2020**, *4*, 2426–2442.

[17] Rui, Y. C.; Jin, Z. M.; Fan, X. Y.; Li, W. T.; Li, B.; Li, T. P.; Wang, Y. Q.; Wang, L.; Liang, J. Defect passivation and electrical conductivity enhancement in perovskite solar cells using functionalized graphene quantum dots. *Mater. Futures* **2022**, *1*, 045101.

[18] Roghabadi, F. A.; Alidaei, M.; Mousavi, S. M.; Ashjari, T.; Tehrani, A. S.; Ahmadi, V.; Sadrameli, S. M. Stability progress of perovskite solar cells dependent on the crystalline structure: From 3D ABX$_3$ to 2D Ruddlesden–Popper perovskite absorbers. *J. Mater. Chem. A* **2019**, *7*, 5898–5933.

[19] Zhou, Y. Y.; Zhao, Y. X. Chemical stability and instability of inorganic halide perovskites. *Energy Environ. Sci.* **2019**, *12*, 1495–1511.

[20] Lin, Y.; Bai, Y.; Fang, Y. J.; Chen, Z. L.; Yang, S.; Zheng, X. P.; Tang, S.; Liu, Y.; Zhao, J. J.; Huang, J. S. Enhanced thermal stability in perovskite solar cells by assembling 2D/3D stacking structures. *J. Phys. Chem. Lett.* **2018**, *9*, 654–658.

[21] Tao, L.; Qiu, J.; Sun, B.; Wang, X. J.; Ran, X. Q.; Song, L.; Shi, W.; Zhong, Q.; Li, P.; Zhang, H. et al. Stability of mixed-halide wide bandgap perovskite solar cells: Strategies and progress. *J. Energy Chem.* **2021**, *61*, 395–415.

[22] Chen, F.; Shi, Z. L.; Chen, J. P.; Cui, Q. N.; Jian, A. Q.; Zhu, Y. Z.; Xu, Q. Y.; Lou, Z. D.; Xu, C. X. Dynamics of interfacial carriers and negative photoconductance in CH$_3$NH$_3$PbBr$_3$-ZnO heterostructure. *Appl. Phys. Lett.* **2021**, *118*, 171901.

[23] Ou, Q. D.; Zhang, Y. P.; Wang, Z. Y.; Yuwono, J. A.; Wang, R. B.; Dai, Z. G.; Li, W.; Zheng, C. X.; Xu, Z. Q.; Qi, X. et al. Strong depletion in hybrid perovskite p-n junctions induced by local electronic doping. *Adv. Mater.* **2018**, *30*, 1705792.

[24] Jena, A. K.; Ikegami, M.; Miyasaka, T. Severe morphological deformation of spiro-OMeTAD in (CH$_3$NH$_3$) PbI$_3$ solar cells at high temperature. *ACS Energy Lett.* **2017**, *2*, 1760–1761.

[25] Zhao, Y. C.; Zhou, W. K.; Zhou, X.; Liu, K. H.; Yu, D. P.; Zhao, Q. Quantification of light-enhanced ionic transport in lead iodide perovskite thin films and its solar cell applications. *Light: Sci. Appl.* **2017**, *6*, e16243.

[26] Wang, Q.; Chen, B.; Liu, Y.; Deng, Y. H.; Bai, Y.; Dong, Q. F.; Huang, J. S. Scaling behavior of moisture-induced grain degradation in polycrystalline hybrid perovskite thin films. *Energy Environ. Sci.* **2017**, *10*, 516–522.

[27] Yang, F. J.; MacQueen, R. W.; Menzel, D.; Musiienko, A.; Al-Ashouri, A.; Thiesbrummel, J.; Shah, S.; Prashanthan, K.; Abou-Ras, D.; Korte, L. et al. Rubidium iodide reduces recombination losses in methylammonium-free tin-lead perovskite solar cells. *Adv. Energy Mater.* **2023**, *13*, 2204339.

[28] Stolterfoht, M.; Wolff, C. M.; Márquez, J. A.; Zhang, S. S.; Hages, C. J.; Rothhardt, D.; Albrecht, S.; Burn, P. L.; Meredith, P.; Unold, T. et al. Visualization and suppression of interfacial recombination for high-efficiency large-area pin perovskite solar cells. *Nat. Energy* **2018**, *3*, 847–854.

[29] Wu, H. J.; Cheng, Y. J.; Ma, J. J.; Zhang, J. H.; Zhang, Y. Q.; Song,

Y. L.; Peng, S. Pivotal routes for maximizing semitransparent perovskite solar cell performance: Photon propagation management and carrier kinetics regulation. *Adv. Mater.* **2023**, *35*, 2206574.

[30] Chen, Z.; Chen, X.; Jia, Z. Y.; Zhou, G. Q.; Xu, J. Q.; Wu, Y. X.; Xia, X. X.; Li, X. F.; Zhang, X. N.; Deng, C. et al. Triplet exciton formation for non-radiative voltage loss in high-efficiency nonfullerene organic solar cells. *Joule* **2021**, *5*, 1832–1844.

[31] Luo, D. Y.; Su, R.; Zhang, W.; Gong, Q. H.; Zhu, R. Minimizing non-radiative recombination losses in perovskite solar cells. *Nat. Rev. Mater.* **2020**, *5*, 44–60.

[32] Huang, J. S.; Yuan, Y. B.; Shao, Y. C.; Yan, Y. F. Understanding the physical properties of hybrid perovskites for photovoltaic applications. *Nat. Rev. Mater.* **2017**, *2*, 17042.

[33] An, Y. D.; Wang, C. L.; Cao, G. Y.; Li, X. F. Heterojunction perovskite solar cells: Opto- electro-thermal physics, modeling, and experiment. *ACS Nano* **2020**, *14*, 5017–5026.

[34] Grimme, S.; Antony, J.; Ehrlich, S.; Krieg, H. A consistent and accurate *ab initio* parametrization of density functional dispersion correction (DFT-D) for the 94 elements H-Pu. *J. Chem. Phys.* **2010**, *132*, 154104.

[35] Ran, C. X.; Xu, J. T.; Gao, W. Y.; Huang, C. M.; Dou, S. X. Defects in metal triiodide perovskite materials towards high-performance solar cells: Origin, impact, characterization, and engineering. *Chem. Soc. Rev.* **2018**, *47*, 4581–4610.

[36] Ball, J. M.; Petrozza, A. Defects in perovskite-halides and their effects in solar cells. *Nat. Energy* **2016**, *1*, 16149.

[37] Ono, L. K.; Liu, S. Z.; Qi, Y. B. Reducing detrimental defects for high-performance metal halide perovskite solar cells. *Angew. Chem., Int. Ed.* **2020**, *59*, 6676–6698.

[38] Xie, H. B.; Wang, Z. W.; Chen, Z. H.; Pereyra, C.; Pols, M.; Galkowski, K.; Anaya, M.; Fu, S.; Jia, X. Y.; Tang, P. Y. et al. Decoupling the effects of defects on efficiency and stability through phosphonates in stable halide perovskite solar cells. *Joule* **2021**, *5*, 1246–1266.

[39] Yang, L. K.; Xiong, Q.; Li, Y. B.; Gao, P.; Xu, B.; Lin, H.; Li, X.; Miyasaka, T. Artemisinin-passivated mixed-cation perovskite films for durable flexible perovskite solar cells with over 21% efficiency. *J. Mater. Chem. A* **2021**, *9*, 1574–1582.

[40] Xu, X.; Wu, Z. Y.; Zhao, Z. B.; Lu, Z. L.; Gao, Y. J.; Huang, X.; Huang, J. W.; Zhang, Z. Y.; Cai, Y. T.; Qu, Y. T. et al. First-principles study of detrimental iodine vacancy in lead halide perovskite under strain and electron injection. *Appl. Phys. Lett.* **2022**, *121*, 092106.

[41] Tong, C. J.; Li, L. Q.; Liu, L. M.; Prezhdo, O. V. Synergy between ion migration and charge carrier recombination in metal-halide perovskites. *J. Am. Chem. Soc.* **2020**, *142*, 3060–3068.

[42] Fu, L.; Li, H.; Wang, L.; Yin, R. Y.; Li, B.; Yin, L. W. Defect passivation strategies in perovskites for an enhanced photovoltaic performance. *Energy Environ. Sci.* **2020**, *13*, 4017–4056.

[43] Aydin, E.; De Bastiani, M.; De Wolf, S. Defect and contact passivation for perovskite solar cells. *Adv. Mater.* **2019**, *31*, 1900428.

[44] Zhan, Y.; Yang, F.; Chen, W. J.; Chen, H. Y.; Shen, Y. X.; Li, Y. W.; Li, Y. F. Elastic lattice and excess charge carrier manipulation in 1D-3D perovskite solar cells for exceptionally long-term operational stability. *Adv. Mater.* **2021**, *33*, 2105170.

[45] Yang, D. W.; Ming, W. M.; Shi, H. L.; Zhang, L. J.; Du, M. H. Fast diffusion of native defects and impurities in perovskite solar cell material $CH_3NH_3PbI_3$. *Chem. Mater.* **2016**, *28*, 4349–4357.

[46] Li, W. W.; Zhao, K. Y.; Zhou, H.; Yu, W. L.; Zhu, J. J.; Hu, Z. G.; Chu, J. H. Precursor solution temperature dependence of the optical constants, band gap and Urbach tail in organic-inorganic hybrid halide perovskite films. *J. Phys. D: Appl. Phys.* **2019**, *52*, 045103.

[47] Shao, Y. C.; Yuan, Y. B.; Huang, J. S. Correlation of energy disorder and open-circuit voltage in hybrid perovskite solar cells. *Nat. Energy* **2016**, *1*, 15001.

[48] Urbach, F. The long-wavelength edge of photographic sensitivity and of the electronic absorption of solids. *Phys. Rev.* **1953**, *92*, 1324–1326.

[49] Troviano, M.; Taretto, K. Urbach energy in CIGS extracted from quantum efficiency analysis of high performance CIGS solar cells. In *Proceedings of the 24th European Photovoltaic Solar Energy Conference*, Hamburg, Germany, 2009, pp 2933–2937.

[50] Subedi, B.; Li, C. W.; Chen, C.; Liu, D. C.; Junda, M. M.; Song, Z. N.; Yan, Y. F.; Podraza, N. J. Urbach energy and open-circuit voltage deficit for mixed anion-cation perovskite solar cells. *ACS Appl. Mater. Interfaces* **2022**, *14*, 7796–7804.

[51] Chantana, J.; Kawano, Y.; Nishimura, T.; Mavlonov, A.; Minemoto, T. Impact of Urbach energy on open-circuit voltage deficit of thin-film solar cells. *Sol. Energy Mater. Sol. Cells* **2020**, *210*, 110502.

[52] Subedi, B.; Li, C. W.; Junda, M. M.; Song, Z. N.; Yan, Y. F.; Podraza, N. J. Effects of intrinsic and atmospherically induced defects in narrow bandgap $(FASnI_3)_x$ $(MAPbI_3)_{1-x}$ perovskite films and solar cells. *J. Chem. Phys.* **2020**, *152*, 064705.

[53] Purohit, S.; Yadav, K. L.; Satapathi, S. Metal halide perovskite heterojunction for photocatalytic hydrogen generation: Progress and future opportunities. *Adv. Mater. Interfaces.* **2022**, *9*, 2200058.

[54] Wang, T. Y.; Deng, W. Q.; Cao, J. P.; Yan, F. Recent progress on heterojunction engineering in perovskite solar cells. *Adv. Energy Mater.* **2023**, *13*, 2201436.

[55] Yuan, Y. B.; Huang, J. S. Ion migration in organometal trihalide perovskite and its impact on photovoltaic efficiency and stability. *Acc. Chem. Res.* **2016**, *49*, 286–293.

[56] Choi, J. I. J.; Khan, M. E.; Hawash, Z.; Kim, K. J.; Lee, H.; Ono, L. K.; Qi, Y. B.; Kim, Y. H.; Park, J. Y. Atomic-scale view of stability and degradation of single-crystal $MAPbBr_3$ surfaces. *J. Mater. Chem. A* **2019**, *7*, 20760–20766.

[57] Shi, Z. M.; Cao, Z.; Sun, X. J.; Jia, Y. P.; Li, D. B.; Cavallo, L.; Schwingenschlögl, U. Uncovering the mechanism behind the improved stability of 2D organic–inorganic hybrid perovskites. *Small* **2019**, *15*, 1900462.

[58] Niu, G. D.; Guo, X. D.; Wang, L. D. Review of recent progress in chemical stability of perovskite solar cells. *J. Mater. Chem. A* **2015**, *3*, 8970–8980.

[59] Zhu, H.; Ma, J. J.; Li, P. W.; Zang, S. Q.; Zhang, Y. Q.; Song, Y. L. Low-dimensional Sn-based perovskites: Evolution and future prospects of solar cells. *Chem* **2022**, *8*, 2939–2960.

[60] Li, X. T.; Hoffman, J. M.; Kanatzidis, M. G. The 2D halide perovskite rulebook: How the spacer influences everything from the structure to optoelectronic device efficiency. *Chem. Rev.* **2021**, *121*, 2230–2291.

[61] Sun, S. Q.; Lu, M.; Gao, X. P.; Shi, Z. F.; Bai, X.; Yu, W. W.; Zhang, Y. 0D perovskites: Unique properties, synthesis, and their applications. *Adv. Sci.* **2021**, *8*, 2102689

[62] Qin, C. J.; Matsushima, T.; Potscavage, W. J. Jr.; Sandanayaka, A. S. D.; Leyden, M. R.; Bencheikh, F.; Goushi, K.; Mathevet, F.; Heinrich, B.; Yumoto, G. et al. Triplet management for efficient perovskite light-emitting diodes. *Nat. Photonics* **2020**, *14*, 70–75.

[63] Zheng, H. Y.; Liu, G. Z.; Zhu, L. Z.; Ye, J. J.; Zhang, X. H.; Alsaedi, A.; Hayat, T.; Pan, X.; Dai, S. Y. The effect of hydrophobicity of ammonium salts on stability of quasi-2D perovskite materials in moist condition. *Adv. Energy Mater.* **2018**, *8*, 1800051.

[64] Xiao, X.; Dai, J.; Fang, Y. J.; Zhao, J. J.; Zheng, X. P.; Tang, S.; Rudd, P. N.; Zeng, X. C.; Huang, J. S. Suppressed ion migration along the in-plane direction in layered perovskites. *ACS Energy Lett.* **2018**, *3*, 684–688.

[65] Jeong, J.; Kim, M.; Seo, J.; Lu, H. Z.; Ahlawat, P.; Mishra, A.; Yang, Y. G.; Hope, M. A.; Eickemeyer, F. T.; Kim, M. et al. Pseudo-halide anion engineering for α-$FAPbI_3$ perovskite solar cells. *Nature* **2021**, *592*, 381–385.

[66] Wang, X. T.; Wang, Y.; Chen, Y. T.; Liu, X. M.; Zhao, Y. X. Efficient and stable $CsPbI_3$ inorganic perovskite photovoltaics enabled by crystal secondary growth. *Adv. Mater.* **2021**, *33*, 2103688.

[67] Du, Y. C.; Tian, Q. W.; Chang, X. M.; Fang, J. J.; Gu, X. J.; He, X. L.; Ren, X. D.; Zhao, K.; Liu, S. Z. Ionic liquid treatment for highest-efficiency ambient printed stable all-inorganic $CsPbI_3$ perovskite solar cells. *Adv. Mater.* **2022**, *34*, 2106750.

[68] Li, H.; Chang, B. H.; Wang, L.; Wang, Z. X.; Pan, L.; Wu, Y. T.;

Liu, Z.; Yin, L. W. Surface reconstruction for tin-based perovskite solar cells. *ACS Energy Lett.* **2022**, *7*, 3889–3899.

[69] Yin, W. J.; Shi, T. T.; Yan, Y. F. Unusual defect physics in CH₃NH₃PbI₃ perovskite solar cell absorber. *Appl. Phys. Lett.* **2014**, *104*, 063903.

[70] Whalley, L. D.; van Gerwen, P.; Frost, J. M.; Kim, S.; Hood, S. N.; Walsh, A. Giant Huang–Rhys factor for electron capture by the iodine intersitial in perovskite solar cells. *J. Am. Chem. Soc.* **2021**, *143*, 9123–9128.

[71] Oner, S. M.; Sezen, E.; Yordanli, M. S.; Karakoc, E.; Deger, C.; Yavuz, I. Surface defect formation and passivation in formamidinium lead triiodide (FAPbI₃) perovskite solar cell absorbers. *J. Phys. Chem. Lett.* **2022**, *13*, 324–330.

[72] Kim, H.; Lee, J. W.; Han, G. R.; Kim, Y. J.; Kim, S. H.; Kim, S. K.; Kwak, S. K.; Oh, J. H. Highly efficient hole transport layer-free low bandgap mixed Pb-Sn perovskite solar cells enabled by a binary additive system. *Adv. Funct. Mater.* **2022**, *32*, 2110069.

[73] Zhang, F.; Sun, X. R.; Xie, H. N.; Cai, X. D.; Zheng, B. L.; Yu, H.; Liu, E. Z.; Hao, X. J.; Zhang, M. Unraveling the mechanism of ion-migration suppression by interstitial doping for operationally stable CsPbI₂Br perovskite solar cells. *Chem. Mater.* **2022**, *34*, 1010–1019.

[74] Liu, Z. D.; Duan, C. H.; Liu, F.; Chan, C. C. S.; Zhu, H. P.; Yuan, L. G.; Li, J.; Li, M. J.; Zhou, B.; Wong, K. S. et al. Perovskite bifunctional diode with high photovoltaic and electroluminescent performance by holistic defect passivation. *Small* **2022**, *18*, 2105196.

[75] Yang, X. Y.; Ni, Y.; Zhang, Y. Z.; Wang, Y. J.; Yang, W. Q.; Luo, D. Y.; Tu, Y. G.; Gong, Q. H.; Yu, H. F.; Zhu, R. Multiple-defect management for efficient perovskite photovoltaics. *ACS Energy Lett.* **2021**, *6*, 2404–2412.

[76] Cho, S. H.; Byeon, J.; Jeong, K.; Hwang, J.; Lee, H.; Jang, J. H.; Lee, J.; Kim, T.; Kim, K.; Choi, M. et al. Investigation of defect-tolerant perovskite solar cells with long-term stability via controlling the self-doping effect. *Adv. Energy Mater.* **2021**, *11*, 2100555.

[77] Liu, G. Z.; Zheng, H. Y.; Ye, J. J.; Xu, S. D.; Zhang, L. Y.; Xu, H. F.; Liang, Z.; Chen, X. J.; Pan, X. Mixed-phase low-dimensional perovskite-assisted interfacial lead directional management for stable perovskite solar cells with efficiency over 24%. *ACS Energy Lett.* **2021**, *6*, 4395–4404.

[78] Zhu, X. J.; Du, M. Y.; Feng, J. S.; Wang, H.; Xu, Z.; Wang, L. K.; Zuo, S. N.; Wang, C. Y.; Wang, Z. Y.; Zhang, C. et al. High-efficiency perovskite solar cells with imidazolium-based ionic liquid for surface passivation and charge transport. *Angew. Chem., Int. Ed.* **2021**, *60*, 4238–4244.

[79] Yao, Z.; Xu, Z.; Zhao, W. G.; Zhang, J. R.; Bian, H.; Fang, Y. K.; Yang, Y.; Liu, S. Z. Enhanced efficiency of inorganic CsPbI₃₋ₓBrₓ perovskite solar cell via self-regulation of antisite defects. *Adv. Energy Mater.* **2021**, *11*, 2100403.

[80] Zhou, Z. M.; Wang, Z. W.; Zhou, Y. Y.; Pang, S. P.; Wang, D.; Xu, H. X.; Liu, Z. H.; Padture, N. P.; Cui, G. L. Methylamine-gas-induced defect-healing behavior of CH₃NH₃PbI₃ thin films for perovskite solar cells. *Angew. Chem.* **2015**, *127*, 9841–9845.

[81] Dunlap-Shohl, W. A.; Zhou, Y. Y.; Padture, N. P.; Mitzi, D. B. Synthetic approaches for halide perovskite thin films. *Chem. Rev.* **2019**, *119*, 3193–3295.

[82] Tian, L. W.; Wen, F.; Zhang, W. F.; Zhang, H. C.; Yu, H.; Lin, P.; Liu, X.; Zhou, S. H.; Zhou, X. Q.; Jiang, Y. T. et al. Rising from the ashes: Gaseous therapy for robust and large-area perovskite solar cells. *ACS Appl. Mater. Interfaces* **2020**, *12*, 49648–49658.

[83] Zhou, Y. Y.; Game, O. S.; Pang, S. P.; Padture, N. P. Microstructures of organometal trihalide perovskites for solar cells: Their evolution from solutions and characterization. *J. Phys. Chem. Lett.* **2015**, *6*, 4827–4839.

[84] Pang, S. P.; Zhou, Y. Y.; Wang, Z. W.; Yang, M. J.; Krause, A. R.; Zhou, Z. M.; Zhu, K.; Padture, N. P.; Cui, G. L. Transformative evolution of organolead triiodide perovskite thin films from strong room-temperature solid–gas interaction between HPbI₃-CH₃NH₂ precursor pair. *J. Am. Chem. Soc.* **2016**, *138*, 750–753.

[85] Liu, Z. H.; Qiu, L. B.; Juarez-Perez, E. J.; Hawash, Z.; Kim, T.; Jiang, Y.; Wu, Z. F.; Raga, S. R.; Ono, L. K.; Liu, S. Z. et al. Gas–solid reaction based over one-micrometer thick stable perovskite films for efficient solar cells and modules. *Nat. Commun.* **2018**, *9*, 3880.

[86] Wang, J. F.; Luo, S. Q.; Tang, X. L.; Xiao, S.; Chen, Z. H.; Pang, S. P.; Zhang, L.; Lin, Y.; He, J.; Yuan, Y. B. Healing the buried cavities and defects in quasi-2D perovskite films by self-generated methylamine gas. *ACS Energy. Lett.* **2021**, *6*, 3634–3642.

[87] Zhou, Y. Y.; Yang, M. J.; Pang, S. P.; Zhu, K.; Padture, N. P. Exceptional morphology-preserving evolution of formamidinium lead triiodide perovskite thin films via organic-cation displacement. *J. Am. Chem. Soc.* **2016**, *138*, 5535–5538.

[88] Zhang, Y.; Zhou, Z. M.; Ji, F. X.; Li, Z. P.; Cui, G. L.; Gao, P.; Oveisi, E.; Nazeeruddin, M. K.; Pang, S. P. Trash into treasure: δ-FAPbI₃ polymorph stabilized MAPbI₃ perovskite with power conversion efficiency beyond 21%. *Adv. Mater.* **2018**, *30*, 1707143.

[89] Li, Z. P.; Wang, X.; Wang, Z. W.; Shao, Z. P.; Hao, L. Z.; Rao, Y.; Chen, C.; Liu, D. C.; Zhao, Q. Q.; Sun, X. H. et al. Ammonia for post-healing of formamidinium-based perovskite films. *Nat. Commun.* **2022**, *13*, 4417.

[90] Lin, Y. Z.; Liu, Y.; Chen, S. S.; Wang, S.; Ni, Z. Y.; Van Brackle, C. H.; Yang, S.; Zhao, J. J.; Yu, Z. H.; Dai, X. Z. et al. Revealing defective nanostructured surfaces and their impact on the intrinsic stability of hybrid perovskites. *Energy Environ. Sci.* **2021**, *14*, 1563–1572.

[91] Fu, S.; Le, J. B.; Guo, X. M.; Sun, N. N.; Zhang, W. X.; Song, W. J.; Fang, J. F. Polishing the lead-poor surface for efficient inverted CsPbI₃ perovskite solar cells. *Adv. Mater.* **2022**, *34*, 2205066.

[92] Jiang, Q.; Chu, Z. M.; Wang, P. Y.; Yang, X. L.; Liu, H.; Wang, Y.; Yin, Z. G.; Wu, J. L.; Zhang, X. W.; You, J. B. Planar-structure perovskite solar cells with efficiency beyond 21%. *Adv. Mater.* **2017**, *29*, 1703852.

[93] Park, B. W.; Kedem, N.; Kulbak, M.; Lee, D. Y.; Yang, W. S.; Jeon, N. J.; Seo, J.; Kim, G.; Kim, K. J.; Shin, T. J. et al. Understanding how excess lead iodide precursor improves halide perovskite solar cell performance. *Nat. Commun.* **2018**, *9*, 3301.

[94] Zhao, L. C.; Li, Q. Y.; Hou, C. H.; Li, S. D.; Yang, X. Y.; Wu, J.; Zhang, S. Y.; Hu, Q.; Wang, Y. J.; Zhang, Y. Z. et al. Chemical polishing of perovskite surface enhances photovoltaic performances. *J. Am. Chem. Soc.* **2022**, *144*, 1700–1708.

[95] Li, F. M.; Zhu, W. D.; Bao, C. X.; Yu, T.; Wang, Y. R. Q.; Zhou, X. X.; Zou, Z. G. Laser-assisted crystallization of CH₃NH₃PbI₃ films for efficient perovskite solar cells with a high open-circuit voltage. *Chem. Commun.* **2016**, *52*, 5394–5397.

[96] Park, S. J.; Kim, A. R.; Hong, J. T.; Park, J. Y.; Lee, S.; Ahn, Y. H. Crystallization kinetics of lead halide perovskite film monitored by *in situ* terahertz spectroscopy. *J. Phys. Chem. Lett.* **2017**, *8*, 401–406.

[97] Shan, X. Y.; Wang, S. M.; Dong, W. W.; Pan, N.; Shao, J. Z.; Wang, X. Q.; Tao, R. H.; Deng, Z. H.; Hu, L. H.; Kong, F. T. et al. Flash surface treatment of CH₃NH₃PbI₃ films using 248 nm KrF excimer laser enhances the performance of perovskite solar cells. *Sol. RRL* **2019**, *3*, 1900020.

[98] Kong, W. C.; Zhao, C.; Xing, J.; Zou, Y. T.; Huang, T.; Li, F.; Yang, J. J.; Yu, W. L.; Guo, C. L. Enhancing perovskite solar cell performance through femtosecond laser polishing. *Sol. RRL* **2020**, *4*, 2000189.

[99] Kedia, M.; Rai, M.; Phirke, H.; Aranda, C. A.; Das, C.; Chirvony, V.; Boehringer, S.; Kot, M.; Byranvand, M. M.; Flege, J. I. et al. Light makes right: Laser polishing for surface modification of perovskite solar cells. *ACS Energy Lett.* **2023**, *8*, 2603–2610.

[100] Peng, J.; Wu, Y. L.; Ye, W.; Jacobs, D. A.; Shen, H. P.; Fu, X.; Wan, Y. M.; The Duong; Wu, N. D.; Barugkin, C. et al. Interface passivation using ultrathin polymer-fullerene films for high-efficiency perovskite solar cells with negligible hysteresis. *Energy Environ. Sci.* **2017**, *10*, 1792–1800.

[101] Zhang, F.; Bi, D. Q.; Pellet, N.; Xiao, C. X.; Li, Z.; Berry, J. J.; Zakeeruddin, S. M.; Zhu, K.; Grätzel, M. Suppressing defects through the synergistic effect of a Lewis base and a Lewis acid for highly efficient and stable perovskite solar cells. *Energy Environ. Sci.* **2018**, *11*, 3480–3490.

[102] Yoo, J. J.; Wieghold, S.; Sponseller, M. C.; Chua, M. R.; Bertram, S. N.; Hartono, N. T. P.; Tresback, J. S.; Hansen, E. C.; Correa-Baena, J. P.; Bulović, V. et al. An interface stabilized perovskite solar cell with high stabilized efficiency and low voltage loss. *Energy Environ. Sci.* **2019**, *12*, 2192–2199.

[103] Cao, J.; Jiang, J. K.; Li, N.; Dong, Y. F.; Jia, Y. H.; Tao, S. X.; Zhao, N. Alkali-cation-enhanced benzylammonium passivation for efficient and stable perovskite solar cells fabricated through sequential deposition. *J. Mater. Chem. A* **2020**, *8*, 19357–19366.

[104] Yang, T. H.; Gao, L. L.; Lu, J.; Ma, C.; Du, Y. C.; Wang, P. J.; Ding, Z. C.; Wang, S. Q.; Xu, P.; Liu, D. L. et al. One-stone-for-two-birds strategy to attain beyond 25% perovskite solar cells. *Nat. Commun.* **2023**, *14*, 839.

[105] Cui, B. B.; Han, Y.; Huang, B. L.; Zhao, Y. Z.; Wu, X. X.; Liu, L.; Cao, G. Y.; Du, Q.; Liu, N.; Zou, W. et al. Locally collective hydrogen bonding isolates lead octahedra for white emission improvement. *Nat. Commun.* **2019**, *10*, 5190.

[106] Yu, S. S.; Liu, H. L.; Wang, S. R.; Zhu, H. W.; Dong, X. F.; Li, X. G. Hydrazinium cation mixed FAPbI$_3$-based perovskite with 1D/3D hybrid dimension structure for efficient and stable solar cells. *Chem. Eng. J.* **2021**, *403*, 125724.

[107] Wu, G. H.; Zhou, C. K.; Ming, W. M.; Han, D.; Chen, S. Y.; Yang, D.; Besara, T.; Neu, J.; Siegrist, T.; Du, M. H. et al. A one-dimensional organic lead chloride hybrid with excitation-dependent broadband emissions. *ACS Energy Lett.* **2018**, *3*, 1443–1449.

[108] Li, Z. Z.; Liu, X. L.; Xu, J.; Yang, S. J.; Zhao, H.; Huang, H.; Liu, S. Z.; Yao, J. X. All-inorganic 0D/3D Cs$_4$Pb(IBr)$_6$/CsPbI$_{3-x}$Br$_x$ mixed-dimensional perovskite solar cells with enhanced efficiency and stability. *J. Mater. Chem. C* **2020**, *8*, 6977–6987.

[109] Lee, J. W.; Dai, Z. H.; Han, T. H.; Choi, C.; Chang, S. Y.; Lee, S. J.; De Marco, N.; Zhao, H. X.; Sun, P. Y.; Huang, Y. et al. 2D perovskite stabilized phase-pure formamidinium perovskite solar cells. *Nat. Commun.* **2018**, *9*, 3021

[110] Li, X. T.; Kepenekian, M.; Li, L. D.; Dong, H.; Stoumpos, C. C.; Seshadri, R.; Katan, C.; Guo, P. J.; Even, J.; Kanatzidis, M. G. Tolerance factor for stabilizing 3D hybrid halide perovskitoids using linear diammonium cations. *J. Am. Chem. Soc.* **2022**, *144*, 3902–3912.

[111] Mahmud, A.; Duong, T.; Peng, J.; Wu, Y. L.; Shen, H. P.; Walter, D.; Nguyen, H. T.; Mozaffari, N.; Tabi, G. D.; Catchpole, K. R. et al. Origin of efficiency and stability enhancement in high-performing mixed dimensional 2D-3D perovskite solar cells: A review. *Adv. Funct. Mater.* **2022**, *32*, 2009164.

[112] Wang, Z. P.; Lin, Q. Q.; Chmiel, F. P.; Sakai, N.; Herz, L. M.; Snaith, H. J. Efficient ambient-air-stable solar cells with 2D-3D heterostructured butylammonium-caesium-formamidinium lead halide perovskites. *Nat. Energy* **2017**, *2*, 17135.

[113] Zheng, X. P.; Hou, Y.; Bao, C. X.; Yin, J.; Yuan, F. L.; Huang, Z. R.; Song, K. P.; Liu, J. K.; Troughton, J.; Gasparini, N. et al. Managing grains and interfaces via ligand anchoring enables 22.3%-efficiency inverted perovskite solar cells. *Nat. Energy* **2020**, *5*, 131–140.

[114] Yao, Q.; Xue, Q. F.; Li, Z. C.; Zhang, K. C.; Zhang, T.; Li, N.; Yang, S. H.; Brabec, C. J.; Yip, H. L.; Cao, Y. Graded 2D/3D perovskite heterostructure for efficient and operationally stable MA-free perovskite solar cells. *Adv. Mater.* **2020**, *32*, 2000571.

[115] Liu, T. T.; Zhang, J.; Qin, M. C.; Wu, X.; Li, F. Z.; Lu, X. H.; Zhu, Z. L.; Jen, A. K. Y. Modifying surface termination of CsPbI$_3$ grain boundaries by 2D perovskite layer for efficient and stable photovoltaics. *Adv. Funct. Mater.* **2021**, *31*, 2009515.

[116] Yu, B. B.; Chen, Z. H.; Zhu, Y. D.; Wang, Y. Y.; Han, B.; Chen, G. C.; Zhang, X. S.; Du, Z.; He, Z. B. Heterogeneous 2D/3D tin-halides perovskite solar cells with certified conversion efficiency breaking 14%. *Adv. Mater.* **2021**, *33*, 2102055.

[117] Feng, X. X.; Chen, R. H.; Nan, Z. A.; Lv, X. D.; Meng, R. Q.; Cao, J.; Tang, Y. Perfection of perovskite grain boundary passivation by Eu-porphyrin complex for overall-stable perovskite solar cells. *Adv. Sci.* **2019**, *6*, 1802040.

[118] Tsai, H.; Nie, W. Y.; Blancon, J. C.; Stoumpos, C. C.; Asadpour, R.; Harutyunyan, B.; Neukirch, A. J.; Verduzco, R.; Crochet, J. J.; Tretiak, S. et al. High-efficiency two-dimensional Ruddlesden–Popper perovskite solar cells. *Nature* **2016**, *536*, 312–316.

[119] Li, W. H.; Gu, X. Y.; Shan, C. W.; Lai, X.; Sun, X. W.; Kyaw, A. K. K. Efficient and stable mesoscopic perovskite solar cell in high humidity by localized Dion–Jacobson 2D-3D heterostructures. *Nano Energy* **2022**, *91*, 106666.

[120] Quan, L. N.; Yuan, M. J.; Comin, R.; Voznyy, O.; Beauregard, E. M.; Hoogland, S.; Buin, A.; Kirmani, A. R.; Zhao, K.; Amassian, A. et al. Ligand-stabilized reduced-dimensionality perovskites. *J. Am. Chem. Soc.* **2016**, *138*, 2649–2655.

[121] Jang, Y. W.; Lee, S.; Yeom, K. M.; Jeong, K.; Choi, K.; Choi, M.; Noh, J. H. Intact 2D/3D halide junction perovskite solar cells via solid-phase in-plane growth. *Nat. Energy* **2021**, *6*, 63–71.

[122] Gharibzadeh, S.; Fassl, P.; Hossain, I. M.; Rohrbeck, P.; Frericks, M.; Schmidt, M.; The Duong; Khan, M. R.; Abzieher, T.; Nejand, B. A. et al. Two birds with one stone: Dual grain-boundary and interface passivation enables > 22% efficient inverted methylammonium-free perovskite solar cells. *Energy Environ. Sci.* **2021**, *14*, 5875–5893.

[123] Li, G. D.; Song, J.; Wu, J. H.; Song, Z. Y.; Wang, X. B.; Sun, W. H.; Fan, L. Q.; Lin, J. M.; Huang, M. L.; Lan, Z. et al. Efficient and stable 2D@3D/2D perovskite solar cells based on dual optimization of grain boundary and interface. *ACS. Energy Lett.* **2021**, *6*, 3614–3623.

[124] Li, L.; Zhou, N.; Chen, Q.; Shang, Q. Y.; Zhang, Q.; Wang, X. D.; Zhou, H. P. Unraveling the growth of hierarchical quasi-2D/3D perovskite and carrier dynamics. *J. Phys. Chem. Lett.* **2018**, *9*, 1124–1132.

[125] Liu, Y.; Lu, R. X.; Zhang, J. F.; Guo, X.; Li, C. Construction of a gradient-type 2D/3D perovskite structure for subsurface passivation and energy-level alignment of an MAPbI$_3$ film. *J. Mater. Chem. A* **2021**, *9*, 26086–26094.

[126] Liu, P.; Xian, Y. M.; Yuan, W. N.; Long, Y.; Liu, K.; Rahman, N. U.; Li, W. Z.; Fan, J. D. Lattice-matching structurally-stable 1D@3D perovskites toward highly efficient and stable solar cells. *Adv. Energy Mater.* **2020**, *10*, 1903654.

[127] Liu, X. M.; Wang, X. T.; Zhang, T. Y.; Miao, Y. F.; Qin, Z. X.; Chen, Y. T.; Zhao, Y. X. Organic tetrabutylammonium cation intercalation to heal inorganic CsPbI$_3$ perovskite. *Angew. Chem., Int. Ed.* **2021**, *60*, 12351–12355.

[128] Chen, B.; Li, T.; Dong, Q. F.; Mosconi, E.; Song, J. F.; Chen, Z. L.; Deng, Y. H.; Liu, Y.; Ducharme, S.; Gruverman, A. et al. Large electrostrictive response in lead halide perovskites. *Nat. Mater.* **2018**, *17*, 1020–1026.

[129] Chen, Y. T.; Liu, X. M.; Zhao, Y. X. Organic matrix assisted low-temperature crystallization of black phase inorganic perovskites. *Angew. Chem., Int. Ed.* **2022**, *61*, e202110603.

[130] Zhang, J. X.; Zhang, G. Z.; Su, P. Y.; Huang, R.; Lin, J. G.; Wang, W. R.; Pan, Z. X.; Rao, H. S.; Zhong, X. H. 1D choline-PbI$_3$-based heterostructure boosts efficiency and stability of CsPbI$_3$ perovskite solar cells. *Angew. Chem., Int. Ed.* **2023**, *62*, e202303486.

[131] Han, Y.; Yue, S. J.; Cui, B. B. Low-dimensional metal halide perovskite crystal materials: Structure strategies and luminescence applications. *Adv. Sci.* **2021**, *8*, 2004805.

[132] Chen, Y. T.; Wang, X. T.; Wang, Y.; Liu, X. M.; Miao, Y. F.; Zhao, Y. X. Functional organic cation induced 3D-to-0D phase transformation and surface reconstruction of CsPbI$_3$ inorganic perovskite. *Sci. Bull.* **2023**, *68*, 706–712.

[133] Ho-Baillie, A.; Zhang, M.; Lau, C. F. J.; Ma, F. J.; Huang, S. J. Untapped potentials of inorganic metal halide perovskite solar cells. *Joule* **2019**, *3*, 938–955.

[134] Dastidar, S.; Hawley, C. J.; Dillon, A. D.; Gutierrez-Perez, A. D.; Spanier, J. E.; Fafarman, A. T. Quantitative phase-change thermodynamics and metastability of perovskite-phase cesium lead iodide. *J. Phys. Chem. Lett.* **2017**, *8*, 1278–1282.

[135] Bai, F. J.; Zhang, J.; Yuan, Y. F.; Liu, H. B.; Li, X. S.; Chueh, C. C.; Yan, H.; Zhu, Z. L.; Jen, A. K. Y. A 0D/3D heterostructured all-inorganic halide perovskite solar cell with high performance and enhanced phase stability. *Adv. Mater.* **2019**, *31*, 1904735.

[136] Zhuang, L. C.; Zhai, L. L.; Li, Y. Y.; Ren, H.; Li, M. J.; Lau, S. P. Mixed dimensional 0D/3D perovskite heterostructure for efficient green light-emitting diodes. *J. Mater. Chem. C* **2021**, *9*, 14318–14326.

[137] Ke, Y.; Guo, J. S.; Kong, D. C.; Wang, J. M.; Kusch, G.; Lin, C.; Liu, D. W.; Kuang, Z. Y.; Qian, D. M.; Zhou, F. Y. et al. Efficient and bright deep-red light-emitting diodes based on a lateral 0D/3D perovskite heterostructure. *Adv. Mater.*, in press, DOI: 10.1002/adma.202207301.

[138] Zhang, J. R.; Bai, D. L.; Jin, Z. W.; Bian, H.; Wang, K.; Sun, J.; Wang, Q.; Liu, S. Z. 3D–2D–0D interface profiling for record efficiency all-inorganic CsPbBrI$_2$ perovskite solar cells with superior stability. *Adv. Energy Mater.* **2018**, *8*, 1703246

[139] Li, N.; Zhu, Z. L.; Chueh, C. C.; Liu, H. B.; Peng, B.; Petrone, A.; Li, X. S.; Wang, L. D.; Jen, A. K. Y. Mixed cation FA$_x$PEA$_{1-x}$PbI$_3$ with enhanced phase and ambient stability toward high-performance perovskite solar cells. *Adv. Energy Mater.* **2017**, *7*, 1601307.

[140] Grancini, G.; Roldán-Carmona, C.; Zimmermann, I.; Mosconi, E.; Lee, X.; Martineau, D.; Narbey, S.; Oswald, F.; De Angelis, F.; Graetzel, M. et al. One-year stable perovskite solar cells by 2D/3D interface engineering. *Nat. Commun.* **2017**, *8*, 15684.

[141] Jiang, Q.; Zhao, Y.; Zhang, X. W.; Yang, X. L.; Chen, Y.; Chu, Z. M.; Ye, Q. F.; Li, X. X.; Yin, Z. G.; You, J. B. Surface passivation of perovskite film for efficient solar cells. *Nat. Photonics* **2019**, *13*, 460–466.

[142] Yang, N.; Zhu, C.; Chen, Y. H.; Zai, H. C.; Wang, C. Y.; Wang, X.; Wang, H.; Ma, S.; Gao, Z. Y.; Wang, X. Y. et al. An *in situ* cross-linked 1D/3D perovskite heterostructure improves the stability of hybrid perovskite solar cells for over 3000 h operation. *Energy Environ. Sci.* **2020**, *13*, 4344–4352.

[143] Chen, R. H.; Shen, H.; Chang, Q.; Tang, Z. H.; Nie, S. Q.; Chen, B. L.; Ping, T.; Wu, B. H.; Yin, J.; Li, J. et al. Conformal imidazolium 1D perovskite capping layer stabilized 3D perovskite films for efficient solar modules. *Adv. Sci.* **2022**, *9*, 2204017.

[144] Yang, W. C.; Ding, B.; Lin, Z. D.; Sun, J. S.; Meng, Y. Y.; Ding, Y.; Sheng, J.; Yang, Z. H.; Ye, J. C.; Dyson, P. J. et al. Visualizing interfacial energy offset and defects in efficient 2D/3D heterojunction perovskite solar cells and modules. *Adv. Mater.* **2023**, *35*, 2302071.

[145] Jiang, Y. T.; Wang, J. B.; Zai, H. C.; Ni, D. Y.; Wang, J. Y.; Xue, P. Y.; Li, N. X.; Jia, B. Y.; Lu, H. J.; Zhang, Y. et al. Reducing energy disorder in perovskite solar cells by chelation. *J. Am. Chem. Soc.* **2022**, *144*, 5400–5410.

[146] Jiang, J. X.; Jin, Z. W.; Lei, J.; Wang, Q.; Zhang, X. S.; Zhang, J. R.; Gao, F.; Liu, S. Z. ITIC surface modification to achieve synergistic electron transport layer enhancement for planar-type perovskite solar cells with efficiency exceeding 20%. *J. Mater. Chem. A* **2017**, *5*, 9514–9522.

[147] Xiong, S. B.; Hou, Z. Y.; Zou, S. J.; Lu, X. S.; Yang, J. M.; Hao, T. Y.; Zhou, Z. H.; Xu, J. H.; Zeng, Y. H.; Xiao, W. et al. Direct observation on p-to *n*-type transformation of perovskite surface region during defect passivation driving high photovoltaic efficiency. *Joule* **2021**, *5*, 467–480.

[148] Solomon, M.; Johnson, A. New research in solar cells: Urbach tails and open circuit voltage. *Elements* **2015**, *11*, 45–52.

[149] Peng, C.; Li, C. W.; Zhu, M. Z.; Zhang, C. J.; Jiang, X. F.; Yin, H.; He, B. L.; Li, H. Y.; Li, M.; So, S. K. et al. Reducing energy disorder for efficient and stable Sn-Pb alloyed perovskite solar cells. *Angew. Chem., Int. Ed.* **2022**, *61*, e202201209.

[150] Mehdizadeh-Rad, H.; Singh, J. Influence of Urbach energy, temperature, and longitudinal position in the active layer on carrier diffusion length in perovskite solar cells. *ChemPhysChem* **2019**, *20*, 2712–2717.

[151] Zhong, Y. F.; Munir, R.; Balawi, A. H.; Sheikh, A. D.; Yu, L. Y.; Tang, M. C.; Hu, H. L.; Laquai, F.; Amassian, A. Mesostructured fullerene electrodes for highly efficient n-i-p perovskite solar cells. *ACS Energy Lett.* **2016**, *1*, 1049–1056.

[152] Lian, J. R.; Lu, B.; Niu, F. F.; Zeng, P. J.; Zhan, X. W. Electron-transport materials in perovskite solar cells. *Small Methods* **2018**, *2*, 1800082.

[153] Guo, Z. L.; Jena, A. K.; Kim, G. M.; Miyasaka, T. The high open-circuit voltage of perovskite solar cells: A review. *Energy Environ. Sci.* **2022**, *15*, 3171–3222.

[154] Mahmood, K.; Sarwar, S.; Mehran, M. T. Current status of electron transport layers in perovskite solar cells: Materials and properties. *RSC Adv.* **2017**, *7*, 17044–17062.

[155] Wei, D.; Ji, J.; Song, D. D.; Li, M. C.; Cui, P.; Li, Y. Y.; Mbengue, J. M.; Zhou, W. J.; Ning, Z. J.; Park, N. G. A TiO$_2$ embedded structure for perovskite solar cells with anomalous grain growth and effective electron extraction. *J. Mater. Chem. A* **2017**, *5*, 1406–1414.

[156] Tress, W.; Marinova, N.; Moehl, T.; Zakeeruddin, S. M.; Nazeeruddin, M. K.; Grätzel, M. Understanding the rate-dependent *J–V* hysteresis, slow time component, and aging in CH$_3$NH$_3$PbI$_3$ perovskite solar cells: The role of a compensated electric field. *Energy Environ. Sci.* **2015**, *8*, 995–1004.

[157] Yang, D.; Yang, R. X.; Zhang, J.; Yang, Z.; Liu, S. Z.; Li, C. High efficiency flexible perovskite solar cells using superior low temperature TiO$_2$. *Energy Environ. Sci.* **2015**, *8*, 3208–3214.

[158] Deng, K. M.; Chen, Q. H.; Li, L. Modification engineering in SnO$_2$ electron transport layer toward perovskite solar cells: Efficiency and stability. *Adv. Funct. Mater.* **2020**, *30*, 2004209.

[159] Yang, D.; Yang, R. X.; Wang, K.; Wu, C. C.; Zhu, X. J.; Feng, J. S.; Ren, X. D.; Fang, G. J.; Priya, S.; Liu, S. Z. High efficiency planar-type perovskite solar cells with negligible hysteresis using EDTA-complexed SnO$_2$. *Nat. Commun.* **2018**, *9*, 3239.

[160] Liu, Z. Z.; Deng, K. M.; Hu, J.; Li, L. Coagulated SnO$_2$ colloids for high-performance planar perovskite solar cells with negligible hysteresis and improved stability. *Angew. Chem.* **2019**, *131*, 11621–11628.

[161] Ma, J.; Lin, Z. H.; Guo, X.; Zhou, L.; Su, J.; Zhang, C. F.; Yang, Z.; Chang, J. J.; Liu, S. Z.; Hao, Y. Low-temperature solution-processed ZnO electron transport layer for highly efficient and stable planar perovskite solar cells with efficiency over 20%. *Sol. RRL* **2019**, *3*, 1900096.

[162] Ma, J.; Su, J.; Lin, Z. H.; Zhou, L.; He, J.; Zhang, J. C.; Liu, S. Z.; Chang, J. J.; Hao, Y. Improve the oxide/perovskite heterojunction contact for low temperature high efficiency and stable all-inorganic CsPbI$_2$Br perovskite solar cells. *Nano Energy* **2020**, *67*, 104241.

[163] Xiao, Z. G.; Bi, C.; Shao, Y. C.; Dong, Q. F.; Wang, Q.; Yuan, Y. B.; Wang, C. G.; Gao, Y. L.; Huang, J. S. Efficient, high yield perovskite photovoltaic devices grown by interdiffusion of solution-processed precursor stacking layers. *Energy Environ. Sci.* **2014**, *7*, 2619–2623.

[164] Chen, K.; Hu, Q.; Liu, T. H.; Zhao, L. C.; Luo, D. Y.; Wu, J.; Zhang, Y. F.; Zhang, W.; Liu, F.; Russell, T. P. et al. Charge-carrier balance for highly efficient inverted planar heterojunction perovskite solar cells. *Adv. Mater.* **2016**, *28*, 10718–10724.

[165] Dong, S. J.; Wan, Y. Y.; Wang, Y. L.; Yang, Y.; Wang, Y. H.; Zhang, X. Y.; Cao, H. Q.; Qin, W. J.; Yang, L. Y.; Yao, C. et al. Polyethylenimine as a dual functional additive for electron transporting layer in efficient solution processed planar heterojunction perovskite solar cells. *RSC Adv.* **2016**, *6*, 57793–57798.

[166] Lee, K.; Ryu, J.; Yu, H.; Yun, J.; Lee, J.; Jang, J. Enhanced efficiency and air-stability of NiO$_x$-based perovskite solar cells via PCBM electron transport layer modification with Triton X-100. *Nanoscale* **2017**, *9*, 16249–16255.

[167] Jiang, M.; Niu, Q. L.; Tang, X.; Zhang, H. Y.; Xu, H. W.; Huang, W. T.; Yao, J. Z.; Yan, B. Y.; Xia, R. D. Improving the performances of perovskite solar cells via modification of electron transport layer. *Polymers* **2019**, *11*, 147.

[168] Xu, L.; Chen, X. F.; Jin, J. J.; Liu, W.; Dong, B.; Bai, X.; Song, H. W.; Reiss, P. Inverted perovskite solar cells employing doped NiO hole transport layers: A review. *Nano Energy* **2019**, *63*, 103860.

[169] Yin, X. T.; Guo, Y. X.; Xie, H. X.; Que, W. X.; Kong, L. B. Nickel oxide as efficient hole transport materials for perovskite solar cells. *Sol. RRL* **2019**, *3*, 1900001.

[170] Chen, W.; Zhou, Y. C.; Wang, L. J.; Wu, Y. H.; Tu, B.; Yu, B. B.; Liu, F. Z.; Tam, H. W.; Wang, G.; Djurišić, A. B. et al. Molecule-doped nickel oxide: Verified charge transfer and planar inverted mixed cation perovskite solar cell. *Adv. Mater.* **2018**, *30*, 1800515.

[171] Wang, S. J.; Li, Y. K.; Yang, J. B.; Wang, T.; Yang, B. W.; Cao, Q.; Pu, X. Y.; Etgar, L.; Han, J.; Zhao, J. S. et al. Critical role of removing impurities in nickel oxide on high-efficiency and long-term stability of inverted perovskite solar cells. *Angew. Chem.* **2022**, *134*, e202116534.

[172] Zhang, B. J.; Su, J.; Guo, X.; Zhou, L.; Lin, Z. H.; Feng, L. P.; Zhang, J. C.; Chang, J. J.; Hao, Y. NiO/perovskite heterojunction contact engineering for highly efficient and stable perovskite solar cells. *Adv. Sci.* **2020**, *7*, 1903044.

[173] Chen, Y.; Yang, Z.; Wang, S. B.; Zheng, X. J.; Wu, Y. H.; Yuan, N. Y.; Zhang, W. H.; Liu, S. Z. Design of an inorganic mesoporous hole-transporting layer for highly efficient and stable inverted perovskite solar cells. *Adv. Mater.* **2018**, *30*, 1805660.

[174] Li, Y. Q.; Wang, W.; Dong, J.; Lu, Y.; Huang, X. F.; Niu, Y.; Qiao, B.; Zhao, S. L.; Xu, Z.; Smirnov, A. et al. Modification of PEDOT:PSS to enhance device efficiency and stability of the quasi-2D perovskite light-emitting diodes. *Org. Electron.* **2022**, *108*, 106579.

[175] Chandel, A.; Ke, Q. B.; Thakur, D.; Chiang, S. E.; Wu, J. R.; Cai, K. B.; Yuan, C. T.; Chang, S. H. Regioregularity effects of p-type P3CT-Na polymers on inverted perovskite photovoltaic cells. *Org. Electron.* **2022**, *102*, 106449.

[176] Hu, L. N.; Zhang, L. L.; Ren, W. H.; Zhang, C. X.; Wu, Y. K.; Liu, Y. F.; Sun, Q. J.; Dai, Z.; Cui, Y. X.; Cai, L. F. et al. High efficiency perovskite solar cells with PTAA hole transport layer enabled by PMMA:F4-TCNQ buried interface layer. *J. Mater. Chem. C* **2022**, *10*, 9714–9722.

[177] Cai, X.; Tang, J.; Zhao, M.; Liu, L.; Yu, Z. B.; Du, J. J.; Bai, L.; Lu, F. S.; Jiu, T. G.; Li, Y. L. Graphdiyne oxide doping for aggregation control of hole-transport nanolayer in inverted perovskite solar cells. *Nano Res.* **2022**, *15*, 9734–9740.

[178] Zhao, B. Y.; Gillan, L. V.; Scully, A. D.; Chesman, A. S. R.; Tan, B. E.; Lin, X. F.; Liu, J. Y.; Rietwyk, K. J.; Deng, S. Q.; Bailey, C. et al. Enhanced carrier diffusion enables efficient back-contact perovskite photovoltaics. *Angew. Chem., Int. Ed.* **2023**, *62*, e202218174.

[179] Shi, M.; Li, G. N.; Tian, W. M.; Jin, S. Y.; Tao, X. P.; Jiang, Y. M.; Pidko, E. A.; Li, R. G.; Li, C. Understanding the effect of crystalline structural transformation for lead-free inorganic halide perovskites. *Adv. Mater.* **2020**, *32*, 2002137.

[180] Cui, P.; Wei, D.; Ji, J.; Song, D. D.; Li, Y. Y.; Liu, X.; Huang, J.; Wang, T. Y.; You, J. B.; Li, M. C. Highly efficient electron-selective layer free perovskite solar cells by constructing effective p-n heterojunction. *Sol. RRL* **2017**, *1*, 1600027.

[181] Cui, P.; Wei, D.; Ji, J.; Huang, H.; Jia, E. D.; Dou, S. Y.; Wang, T. Y.; Wang, W. J.; Li, M. C. Planar p-n homojunction perovskite solar cells with efficiency exceeding 21.3%. *Nat. Energy* **2019**, *4*, 150–159.

[182] Zhang, J. K.; Sun, Y. P.; Huang, C. W.; Yu, B.; Yu, H. Z. Reduced open-circuit voltage loss of perovskite solar cells via forming p/p$^+$ homojunction and interface electric field on the surfaces of perovskite film. *Adv. Energy Mater.* **2022**, *12*, 2202542.

[183] Chu, X. B.; Ye, Q. F.; Wang, Z. H.; Zhang, C.; Ma, F.; Qu, Z. H.; Zhao, Y.; Yin, Z. G.; Deng, H. X.; Zhang, X. W. et al. Surface *in situ* reconstruction of inorganic perovskite films enabling long carrier lifetimes and solar cells with 21% efficiency. *Nat. Energy* **2023**, *8*, 372–380.

[184] Luo, D. Y.; Zhao, L. C.; Wu, J.; Hu, Q.; Zhang, Y. F.; Xu, Z. J.; Liu, Y.; Liu, T. H.; Chen, K.; Yang, W. Q. et al. Dual-source precursor approach for highly efficient inverted planar heterojunction perovskite solar cells. *Adv. Mater.* **2017**, *29*, 1604758.

[185] Jeon, N. J.; Na, H.; Jung, E. H.; Yang, T. Y.; Lee, Y. G.; Kim, G.; Shin, H. W.; Il Seok, S.; Lee, J.; Seo, J. A fluorene-terminated hole-transporting material for highly efficient and stable perovskite solar cells. *Nat. Energy* **2018**, *3*, 682–689.

[186] Wu, S. F.; Zhang, J.; Li, Z.; Liu, D. J.; Qin, M. C.; Cheung, S. H.; Lu, X. H.; Lei, D. Y.; So, S. K.; Zhu, Z. L. et al. Modulation of defects and interfaces through alkylammonium interlayer for efficient inverted perovskite solar cells. *Joule* **2020**, *4*, 1248–1262.

[187] Wu, S. F.; Li, Z.; Zhang, J.; Wu, X.; Deng, X.; Liu, Y. M.; Zhou, J. K.; Zhi, C. Y.; Yu, X. G.; Choy, W. C. H. et al. Low-bandgap organic bulk-heterojunction enabled efficient and flexible perovskite solar cells. *Adv. Mater.* **2021**, *33*, 2105539.

[188] Zhang, B.; Oh, J.; Sun, Z.; Cho, Y.; Jeong, S.; Chen, X.; Sun, K.; Li, F.; Yang, C.; Chen, S. S. Buried guanidinium passivator with favorable binding energy for perovskite solar cells. *ACS Energy. Lett.* **2023**, *8*, 1848–1856.

[189] Yin, Y. F.; Tian, W. M.; Luo, H.; Gao, Y. X.; Zhao, T. T.; Zhao, C. Y.; Leng, J.; Sun, Q.; Tang, J. B.; Wang, P. et al. Excellent carrier transport property of hybrid perovskites sustained under high pressures. *ACS Energy Lett.* **2022**, *7*, 154–161.

[190] Hu, J. T.; Chen, P.; Luo, D. Y.; Dai, L. J.; Chen, N.; Li, S. D.; Yang, S. Y.; Fu, Z. W.; Wang, D. K.; Gong, Q. H. et al. Anchoring of halogen-cleaved organic ligands on perovskite surfaces. *Energy Environ. Sci.* **2022**, *15*, 5340–5349.

[191] Yan, J. L.; Croes, G.; Fakharuddin, A.; Song, W. Y.; Heremans, P.; Chen, H. Z.; Qiu, W. M. Exploiting two-step processed mixed 2D/3D perovskites for bright green light emitting diodes. *Adv. Opt. Mater.* **2019**, *7*, 1900465.

[192] Wang, M. R.; Shi, Z. F.; Fei, C. B.; Deng, Z. J. D.; Yang, G.; Dunfield, S. P.; Fenning, D. P.; Huang, J. S. Ammonium cations with high p$K_a$ in perovskite solar cells for improved high-temperature photostability. *Nat. Energy*, in press, DOI: 10.1038/s41560-023-01362-0.

[193] Li, H. Y.; Shen, N.; Chen, S.; Guo, F.; Xu, B. M. Recent progress on synthesis, intrinsic properties and optoelectronic applications of perovskite single crystals. *Adv. Funct. Mater.* **2023**, *33*, 2214339.

[194] Li, Z. H.; Li, P. W.; Chen, G. S.; Cheng, Y. J.; Pi, X. D.; Yu, X. G.; Yang, D. R.; Han, L. Y.; Zhang, Y. Q.; Song, Y. L. Ink engineering of inkjet printing perovskite. *ACS Appl. Mater. Interfaces* **2020**, *12*, 39082–39091.

[195] Park, N. G. Perovskite solar cell: Research direction for next 10 years. *ACS Energy Lett.* **2019**, *4*, 2983–2985.

[196] Zhang, K.; Wang, Y.; Tao, M. Q.; Guo, L. T.; Yang, Y. R.; Shao, J. Y.; Zhang, Y. Y.; Wang, F. Y.; Song, Y. L. Efficient inorganic vapor-assisted defects passivation for perovskite solar module. *Adv. Mater.* **2023**, *35*, 2211593.

[197] Luo, C.; Zheng, G. H. J.; Wang, X. J.; Gao, F.; Zhan, C. L.; Gao, X. Y.; Zhao, Q. Solid–solid chemical bonding featuring targeted defect passivation for efficient perovskite photovoltaics. *Energy Environ. Sci.* **2023**, *16*, 178–189.

[198] Nazir, G.; Lee, S. Y.; Lee, J. H.; Rehman, A.; Lee, J. K.; Seok, S. I.; Park, S. J. Stabilization of perovskite solar cells: Recent developments and future perspectives. *Adv. Mater.* **2022**, *34*, 2204380.

[199] Xie, L. S.; Du, S. Y.; Li, J.; Liu, C.; Pu, Z. W.; Tong, X. Y.; Liu, J.; Wang, Y. H.; Meng, Y. Y.; Yang, M. J. et al. Molecular dipole engineering-assisted strain release for mechanically robust flexible perovskite solar cells. *Energy Environ. Sci.*, in press, DOI: 10.1039/D3EE02569A.

[200] Nie, L.; Wang, T.; Yu, X.; Gao, W.; Peng, Q. P.; Xia, Z. G.; Qiu, J. B.; Yu, S. F.; Xu, X. H. Multicolor display fabricated via stacking CW laser-patterned perovskite films. *ACS Energy. Lett.* **2023**, *8*, 2025–2032.

[201] Wang, R. J.; Wu, J. H.; Wei, S. P.; Zhu, J. W.; Guo, M. H.; Zheng, Q.; Wei, M. D.; Cheng, S. Y. Gadolinium-doped SnO$_2$ electron transfer layer for highly efficient planar perovskite solar cells. *J. Power Sources* **2022**, *544*, 231870.

[202] Mishra, A.; Bose, R.; Zheng, Y. Z.; Xu, W. J.; McMullen, R.; Mehta, A. B.; Kim, M. J.; Hsu, J. W. P.; Malko, A. V.; Slinker, J. D. Stable and bright electroluminescent devices utilizing emissive 0D perovskite nanocrystals incorporated in a 3D CsPbBr$_3$ matrix. *Adv. Mater.* **2022**, *34*, 2203226.

[203] Benin, B. M.; Dirin, D. N.; Morad, V.; Wörle, M.; Yakunin, S.; Rainò, G.; Nazarenko, O.; Fischer, M.; Infante, I.; Kovalenko, M. V. Highly emissive self-trapped excitons in fully inorganic zero-

dimensional tin halides. *Angew. Chem., Int. Ed.* **2018**, *57*, 11329–11333.

[204] Kong, T. F.; Xie, H. B.; Zhang, Y.; Song, J.; Li, Y. H.; Lim, E. L.; Hagfeldt, A.; Bi, D. Q. Perovskitoid-templated formation of a 1D@3D perovskite structure toward highly efficient and stable perovskite solar cells. *Adv. Energy Mater.* **2021**, *11*, 2101018.

[205] Wang, Y.; Ye, J. C.; Song, J. X.; Chu, L.; Zang, Y.; Li, G. D.; Zhou, Q.; Yang, G. Y.; Tu, Y. B.; Jin, Y. Z. et al. Modulation of buried interface by 1-(3-aminopropyl)-imidazole for efficient inverted formamidinium-cesium perovskite solar cells. *Small*, in press, DOI: 10.1002/smll.202304273.

[206] Chen, Q. H.; Deng, K. M.; Shen, Y.; Li, L. Stable one dimensional (1D)/three dimensional (3D) perovskite solar cell with an efficiency exceeding 23%. *InfoMat* **2022**, *4*, e12303.

[207] Ge, C. Y.; Lu, J. F.; Singh, M.; Ng, A.; Yu, W.; Lin, H. R.; Satapathi, S.; Hu, H. L. Mixed dimensional perovskites heterostructure for highly efficient and stable perovskite solar cells. *Sol. RRL* **2022**, *6*, 2100879.

[208] Zhang, H. J.; Shi, Z. J.; Hu, L. G.; Tang, Y. Y.; Qin, Z. Y.; Liao, W. Q.; Wang, Z. S.; Qin, J. J.; Li, X. G.; Wang, H. L. et al. Highly efficient 1D/3D ferroelectric perovskite solar cell. *Adv. Funct. Mater.* **2021**, *31*, 2100205.

[209] Chen, P.; Bai, Y.; Wang, S. C.; Lyu, M. Q.; Yun, J. H.; Wang, L. Z. *In situ* growth of 2D perovskite capping layer for stable and efficient perovskite solar cells. *Adv. Funct. Mater.* **2018**, *28*, 1706923.

[210] Cao, J.; Li, C. P.; Lv, X. D.; Feng, X. X.; Meng, R. Q.; Wu, Y. Y.; Tang, Y. Efficient grain boundary suture by low-cost tetra-ammonium zinc phthalocyanine for stable perovskite solar cells with expanded photoresponse. *J. Am. Chem. Soc.* **2018**, *140*, 11577–11580.

[211] Min, H.; Lee, D. Y.; Kim, J.; Kim, G.; Lee, K. S.; Kim, J.; Paik, M. J.; Kim, Y. K.; Kim, K. S.; Kim, M. G. Perovskite solar cells with atomically coherent interlayers on $SnO_2$ electrodes. *Nature* **2021**, *598*, 444–450.

[212] Lin, L. Y.; Li, P.; Kang, Z. J.; Xiong, H.; Chen, Y. T.; Yan, Q.; Jiang, L. Q.; Qiu, Y. Device design of doping-controlled homojunction perovskite solar cells omitting HTL and exceeding 25% efficiency. *Adv. Theory Simul.* **2021**, *4*, 2000222.

[213] Song, D. D.; Cui, P.; Wang, T. Y.; Wei, D.; Li, M. C.; Cao, F. H.; Yue, X. P.; Fu, P. F.; Li, Y. Y.; He, Y. et al. Managing carrier lifetime and doping property of lead halide perovskite by postannealing processes for highly efficient perovskite solar cells. *J. Phys. Chem. C* **2015**, *119*, 22812–22819.

[214] Sengar, B. S.; Garg, V.; Kumar, A.; Dwivedi, P. Numerical simulation: Design of high-efficiency planar p-n homojunction perovskite solar cells. *IEEE Trans. Electron Devices* **2021**, *68*, 2360–2364.

[215] Lian, X. M.; Chen, J. H.; Shan, S. Q.; Wu, G.; Chen, H. Z. Polymer modification on the $NiO_x$ hole transport layer boosts open-circuit voltage to 1.19 V for perovskite solar cells. *ACS Appl. Mater. Interfaces* **2020**, *12*, 46340–46347.